UNIVERSITAT POLITÈCNICA DE CATALUNYA BARCELONATECH

Spectral response of individual molecules and nanoantennas with two-beam excitation

by
Esther Gellings

Spectral Response of Individual Molecules and Nanoantennas with Two-Beam Excitation

Doctoral Thesis

by

Esther Gellings

Thesis Advisor:
Prof. Dr. Niek F. van Hulst

February 2020

ICFO – The Institute of Photonic Sciences
BIST – Barcelona Institute of Science and Technology
UPC – Universitat Politècnica de Catalunya

Thesis advisor:
Prof. Dr. Niek van Hulst

Thesis committee:
Prof. Dr. Frank Cichos (Universität Leipzig)
PD Dr. Dai Zhang (Eberhard Karls Universität Tübingen)
Prof. Dr. María García-Parajo (ICFO – The Institute of Photonic Sciences)

Abstract

At room temperature, individual molecules can be found in different conformations due to intrinsic and extrinsic factors, which are reflected in spectral variability. When detecting single molecules, the ensemble average is lifted and the spectral variability is no longer obscured by the inhomogeneously broadened ensemble spectrum. Yet, only about one in every 10^7 photons interacts with the molecule, so that detection necessarily relies on background-free fluorescence. Fluorescence emission spectra only contain information about the ground state of molecules. In this thesis, two new detection techniques are introduced to overcome this limitation: fluorescence excitation spectroscopy and stimulated emission detection. Moreover, the latter method is adapted to probe individual plasmonic nanoantennas.

First, Fourier transform excitation spectroscopy is introduced as a sensitive and robust method to probe the excited state manifold of single molecules. Fluorescence excitation and emission spectra complement each other, the former probing the excited state, and the latter probing the ground state manifold. Both spectra are routinely measured at cryogenic temperatures, though excitation spectroscopy has only recently reached single molecule sensitivity at room temperature. Here, Fourier transform spectroscopy is adapted to measure excitation spectra of single molecules. The working of the technique is demonstrated on synthetic dye molecules, where a spectral variability of more than 100 nm has been uncovered. It is then applied to photosynthetic light-harvesting complexes LH2 that exhibit near-unity energy transfer efficiencies despite large environmental differences. Excitation spectra were routinely measured alongside emission spectra and it was found that variations in the two absorption bands B800 and B850 are uncorrelated, while the Stokes shift between the B850 and emission band becomes larger for more red-shifted complexes. The single complex Stokes shift was found to be about 20 % larger than the ensemble result.

Second, a stimulated emission pump-probe setup with single molecule sensitivity is developed, which does not rely on fluorescence detection and can directly probe excited state dynamics. The necessary steps to achieve shot noise limited sensitivity will be explained. Stimulated emission depletion measurements are performed to verify the alignment of the setup and to find the best experimental parameters. The stimulated emission measurements achieved sensitivities of up to 10^{-8}, which in principle is sufficient for single molecule detection.

Finally, the stimulated emission setup has been applied to study the scattering and absorption of single plasmonic nanoantennas in focused Gaussian beams. In photothermal microscopy, the contribution of the scattering component and focal position to the signal has been largely ignored. Here, a comprehensive model

including all relevant parameters is developed and systematically probed on nano-antennas of various lengths, positions in the focus, and surrounding media. It will be shown that the interaction of an antenna with a single probe beam results in a dispersive interference signal that mainly depends on the antenna dimensions, and that flips sign when passing through the antenna resonance. Adding a modulated pump beam that heats the antenna's environment leads to a combination of the probe beam scattering off the refractive index gradient around the nanoantenna, and the antenna resonance shifting, which affects the interference between the incident and scattered light. It will be demonstrated that both effects are relevant for antennas with a significant scattering cross-section and that photothermal measurements strongly depend on the photothermal properties of the surrounding medium and the antenna dimensions, which lead to strong signal variations around antenna resonance.

Resumen

A temperatura ambiente, las moléculas individuales se pueden encontrar en distintas conformaciones debido a factores intrínsecos y extrínsecos que se reflejan en la variabilidad espectral. Cuando se detectan moléculas aisladas, la variabilidad espectral ya no se ve oculta debido al espectro ensanchado del conjunto molecular. Sin embargo, solo aproximadamente uno de cada 10^7 fotones interactúa con la molécula, por lo cual la detección necesariamente se basa en la fluorescencia libre del ruido de fondo. Los espectros de emisión de fluorescencia solo contienen información sobre el estado fundamental de las moléculas. En esta tesis se introducen dos nuevas técnicas de detección para superar esta limitación: espectroscopía de excitación de fluorescencia y detección de emisión estimulada. Además, el segundo método está adaptado para investigar nanoantenas plasmónicas individuales.

En primer lugar, se introduce la espectroscopía de excitación por transformada de Fourier como un método sensible y robusto para investigar el estado excitado de moléculas individuales. Los espectros de excitación y emisión de fluorescencia se complementan entre sí, el primero prueba el estado excitado y el segundo el estado fundamental. Ambos espectros se miden por lo general a temperaturas criogénicas, aunque la espectroscopía de excitación solo recientemente ha alcanzado la sensibilidad para medir moléculas individuales a temperatura ambiente. En este trabajo, la espectroscopía de transformada de Fourier está adaptada para medir los espectros de excitación de moléculas individuales. El funcionamiento de esta técnica se demuestra en moléculas de colorante sintéticas, donde se ha descubierto una variabilidad espectral de más de 100 nm. Luego se aplica a los complejos fotosintéticos de captación de luz LH2 que exhiben eficiencias de transferencia de energía cercanas a la unidad a pesar de grandes diferencias en su entorno. Los espectros de excitación se midieron conjuntamente con los espectros de emisión y se descubrió que las variaciones en las dos bandas de absorción B800 y B850 no están correlacionadas, mientras que el desplazamiento de Stokes entre el B850 y la banda de emisión se hace más grande para más complejos desplazados al rojo. Se constantó que el desplazamiento de Stokes en complejos individuales era aproximadamente 20 % más grande que el resultado del conjunto.

En segundo lugar, se desarrolla una configuración de bombeo-prueba para medir con mayor sensibilidad la emisión estimulada de moléculas individualesla cual no se basa en la detección de fluorescencia y puede probar directamente la dinámica del estado excitado. Se explicarán los pasos necesarios para lograr una sensibilidad que solo es limitada por el de disparo. Se realizan mediciones de del decaimiento de la emisión estimulada para verificar la alineación del dispositivo experimental y para encontrar los mejores parámetros experimentales. Las mediciones de emisiones

estimuladas lograron sensibilidades de hasta 10^{-8}, que en principio es suficiente para la detección de una sola molécula.

Finalmente, el experimento para medir emisión estimulada está adaptado para estudiar la dispersión y absorción de nanoantenas plasmónicas individuales en haces gaussianos enfocados. En la microscopía fototérmica se ha ignorado, en gran medida, la contribución de la componente de dispersión y de la posición focal a la señal. En este trabajo, se desarrolla un modelo integral que incluye todos los parámetros relevantes y se prueba sistemáticamente en nanoantenas con diferentes longitudes, posiciones en el foco y medios circundantes. Se demostrará que la interacción de una antena con un solo haz de prueba da como resultado una señal de interferencia dispersiva que depende principalmente de las dimensiones de la antena y, que cambia de signo cuando pasa a través de la resonancia de la antena. Agregar un haz de bombeo modulado que calienta el entorno de la antena provoca una combinación de dispersión del haz de prueba con el gradiente del índice de refracción alrededor de la nanoantena, y el desplazamiento de resonancia de la antena, que afecta la interferencia entre la luz incidente y la dispersa. Se demostrará que ambos efectos son relevantes para antenas con una sección eficaz de dispersión significativa y que las mediciones fototérmicas dependen en gran medida de las propiedades fototérmicas del medio circundante y las dimensiones de la antena, lo que resulta en fuertes variaciones de la señal alrededor de la resonancia de la antena.

Contents

Introduction

It took a little more than 300 years from the discovery of the light spectrum to the first recording of the excitation and emission spectrum of a single molecule. In the 17th century, Sir Isaac Newton discovered that white light is actually a mixture of colors, and he called the dispersed rainbow pattern that he observed with prisms a spectrum[1]. By 1802, William Wollaston observed that there were some dark lines in the spectrum of sunlight[2]. This prompted Joseph von Fraunhofer to systematically study these lines, which are called Fraunhofer lines until today, and to introduce a quantified wavelength scale to be able to compare his results between labs[3]. Around the same time, John Herschel and William Talbot discovered that different salts produce distinct line patterns when added to flames[4, 5], which Gustav Kirchhoff and Robert Bunsen interpreted as the absorption and emission lines of specific elements in the 1860s[6]. The realization that atoms are made up of electrons[7], and a nucleus[8] at the turn of the 20th century allowed Niels Bohr to propose his quantum mechanical hydrogen model, where electrons could only move around the nucleus on orbits of a discrete set of energy levels corresponding to the spectral lines[9]. From this moment onward, quantum mechanics developed in parallel with spectroscopy continued, and the ability to measure the composition and structure of matter over the entire electromagnetic spectrum, and from the atomic scale to astronomical distances made spectroscopy a standard technique in many scientific sub-disciplines[10–14].

One of the central topics of this thesis is single molecule spectroscopy. The energy levels, and thus the spectra characteristic for a specific molecule do vary due to both intrinsic and extrinsic factors[15]. Averaging over the heterogeneous distribution of these variable spectra of a specific molecule thus leads to inhomogeneously broadened ensemble spectra. Consequently, many spectral subtleties of the individual molecules are hidden, especially in the case of more complex molecules. This motivated a push to lift the ensemble average via single molecule measurements. The first methods that allowed to selectively study molecular sub-ensembles emerged in the 1970s[15, 16]. Fluorescence line narrowing records the fluorescence spectra of molecular subsets that are excited by a narrowband tunable laser[17]. Spectral hole burning "burns" all molecules resonant at a certain wavelength, which results in a persistent dip in the absorption spectrum at that specific wavelength[18, 19]. These methods became quite sensitive over time[15], but they ultimately still probed a subset of molecules, though with a much narrower distribution.

By the late 1980s, the first successful measurement of a single molecule in a condensed medium was achieved by Moerner and Kador through absorption[20], and by Orrit and Bernard through fluorescence detection[21]. Due to the spectral separation between the excitation wavelength and the Stokes-shifted fluorescence,

fluorescence detection provides superior signal-to-noise and signal-to-background ratios than absorption, and became the norm for most subsequent experiments[22, 23]. At cryogenic temperatures, excitation spectra are typically measured by scanning a tunable narrowband laser across the absorption band of a diluted ensemble sample. The narrow zero-phonon-lines of individual molecules appear as spectrally separated spikes at different wavelengths in the excitation spectrum. At ambient temperatures, single molecules could be studied in a more natural state, but significantly broadened absorption bands, reduced photostability, and a six orders of magnitude lower absorption cross-section need to be overcome. This required faster, and more sensitive detection techniques that spatially select individual molecules by only having one of them in the focus at a time[24, 25]. Room temperature spectroscopic experiments were exclusively based on the detection of fluorescence emission spectra, facilitated by the development of charge-coupled device (CCD) cameras[26–28].

The ability to remove the ensemble average unraveled many effects related to the single quantum emitter nature of individual molecules. They include spectral diffusion, fluorescence intermittency, and the ability to optically control the fluorescence emission of molecules through photoswitching[16]. Single molecule methods quickly became an important part of modern science, penetrating especially physics, chemistry, and biology. Spectral measurements that probe the statistical distribution of spectra offer information about the conformation and nanoenvironment of the individual molecules[29–32]. Temporal measurements unravel molecular kinetics like the interplay between different intramolecular energy pathways[33–35]. Super-resolution fluorescence microscopic techniques including near-field scanning optical microscopy (NSOM) were pioneered by Eric Betzig[24], and stimulated emission depletion (STED) developed by Stefan Hell [36]. They beat the diffraction limit, enabling the localization of molecules with a precision of few tens of nanometer[37, 38] which has already unraveled the working mechanisms of many important cellular processes[39, 40].

Without a doubt, the field of single molecule spectroscopy and detection has matured significantly over the past 30 years. Still, not all ensemble techniques at room temperature have reached single molecule sensitivity, and information about certain molecular properties is lacking. In this thesis, two new detection techniques are introduced and one of them is adapted to probe individual plasmonic nanoantennas. This thesis is divided into three topics:

1. Fourier transform excitation spectroscopy is adapted to single molecule requirements and introduced as a robust technique to probe the excited state manifold.

2. Stimulated emission measurements which can directly probe excited state dynamics and which are not limited by fluorescence detection, are pushed to reach single molecule sensitivity.

3. A comprehensive model for the scattering and absorption of single particles in a focused Gaussian beam is developed and systematically tested on plasmonic nanoantennas.

The first part of the thesis focuses on developing a robust technique based on Fourier transform spectroscopy with which the excited state manifold of single molecules can be probed routinely at room temperature. Fluorescence excitation and emission spectra complement each other, the former probing the excited state, and the latter the ground state manifold. While both excitation and emission spectra are measured at cryogenic temperatures[21, 26, 41], excitation spectra only became available very recently at room temperature in proof-of-principle studies on bright, photostable synthetic dye molecules[32, 42, 43]. The availability of the variability of the excited state manifold will help improve data interpretation and models. Here, Fourier transform spectroscopy is adapted to the requirements of single molecule detection. The sensitivity and robustness of the technique is such that the fluorescence excitation spectra of weakly fluorescing biologically relevant systems can be routinely measured at room temperature.

For the second topic of the thesis, a stimulated emission setup with single molecule sensitivity is developed. Single molecules have an absorption cross-section of $\sim 10^{-16}$ cm^2 at room temperature, while the excitation focus has a diffraction limited spot size of $\sim 10^{-9}$ cm^2[44]. This mismatch in sizes signifies that only one in every 10^7 photons interacts with the molecule, and signal-to-background ratios of 10^{-7} need to be overcome. Yet, stimulated emission can be applied to non-fluorescent molecules and enable the direct detection of ultrafast molecular process ($\sim$ fs), which are currently limited to the indirect detection of the spectrally separated fluorescence ($\sim$ ns)[45–47]. Some pioneering pump-probe techniques that do not rely on fluorescence detection have reached single molecule sensitivity a decade ago, including transmission microscopy[48], ground state depletion[44] and photothermal contrast[49]. Stimulated emission would add the first non-fluorescence based optical technique to the single molecule toolbox that can directly probe the excited state dynamics.

For the third thesis topic, the stimulated emission setup is adapted to probe plasmonic nanoparticles with it. Due to its spectral sensitivity as well as its spatial and temporal resolution, single molecule techniques have always been applied to other systems including individual quantum dots[50, 51], colored centers in diamonds[52], and plasmonic nanoparticles[53]. In the latter case, the detection limit for the scattering spectra was reached for a particle diameter of $\sim$40 nm[54]. More advanced scattering techniques like interferometric scattering microscopy (iSCAT)

beat this limit to ∼5 nm[55], while photothermal microscopy instead exploited the dominance of the absorption over the scattering contribution for small particles, and has even reached single molecule sensitivity[49, 56]. In models that describe photothermal microscopy, the scattering contribution or focal dependence of the measured signal are often neglected. While the former may be valid for the small particles used in the initial studies, it is no longer valid for larger plasmonic particles studied in subsequent experiments[57–60]. Here, a comprehensive model to explain the interaction between tightly focused Gaussian beams and plasmonic nanoparticles is developed, that includes the role of scattering, and whose validity will be systematically probed for plasmonic gold nanorods of various lengths, positions in the focus, and surrounding media.

Thesis outline

This thesis is organized into five chapters as follows:

- Chapter 1 describes the main concepts and experimental methods that are necessary to understand and interpret the experiments presented in this thesis, including molecular spectroscopy, single molecule detection, confocal microscopy, and Fourier transform spectroscopy.

- In chapter 2, Fourier transform excitation spectroscopy is performed on photostable synthetic dye molecules alongside emission spectroscopy. The sensitivity and robustness of the technique is demonstrated and the importance of choosing the correct excitation wavelength and detection window to observe the complete spectral range is discussed.

- Chapter 3 investigates emission and excitation spectra of weakly fluorescing light harvesting complexes, demonstrating the maturity of the Fourier transform spectroscopic method for single molecule detection. The newly available variability of the excited state manifold will be explored in detail.

- In chapter 4, a cw pump-probe setup is built to enable the shot-noise limited detection of stimulated emission. Stimulated emission depletion measurements demonstrate the excellent alignment of the setup, while stimulated emission measurements had sufficient sensitivity to detect single molecules.

- Chapter 5 ventures into nanoplasmonics. The extremely sensitive setup developed in chapter 4 is exploited to study how a single gold nanorod interacts with a focused Gaussian beam for different antenna dimensions, positions, and surrounding media. Both the interaction with a single beam, and the change of interaction when heating the surrounding medium with a modulated pump beam are considered, and the interpretation complemented by comprehensive models.

1 | Experimental methods for single molecule spectroscopy

One of the central topics of this thesis is single molecule spectroscopy at room temperature. Besides using already established techniques such as fluorescence emission spectroscopy, others like Fourier transform excitation spectroscopy and stimulated emission detection will be brought to the single molecule sensitivity level to access new spectral regimes. This first chapter introduces the main concepts and experimental techniques that will be used throughout the thesis. After a general introduction into molecular spectroscopy, the requirements for detecting the spectral response at the single molecule level. Finally, the theoretical foundation of Fourier transform spectroscopy will be explained, on which the excitation spectrum measurements are based.

Molecules and their detection are at the heart of this thesis. That is why this chapter starts with a general description of molecules and various processes that take place when they are photoexcited. With this foundation, the specifics of single molecule detection such as weak signal strength, limited photostability and spectral variability are discussed together with detection techniques developed to reach single molecule sensitivity. While the field of single molecule detection has matured over the past thirty years, some spectral regimes have remained inaccessible, especially at room temperature. This thesis introduces Fourier transform spectroscopy to single molecule spectroscopy, as one of the first studies to make excitation spectra available. Its working principles will be introduced in the last part of this chapter.

1.1 Molecular spectroscopy

Spectroscopy is one of the dominant tools to characterize, understand and eventually control the properties of optically active molecules. According to quantum mechanics, a molecule can only be found in a discrete set of energy levels. Each molecule has its own unique set of energy levels, which is their footprint. This section introduces some of the underlying concepts of what molecular energy levels are and how they can be measured. If not stated otherwise, the explanations follow the conventions of the book of Valeur and Berberan-Santos[61]. They will form the basis for the interpretation of the experimental results presented in the following chapters. The energy levels of a molecule are often visualized in a Jablonski diagram like the one in figure 1.1a. They are grouped into the electronic ground state S_0, the first excited electronic singlet states S_1 and the first excited electronic triplet state T_1. Each electronic state contains multiple vibrational energy levels, which originate from periodic vibrations of the atoms within the molecule. They are drawn as horizontal black lines, where the bold lines represent the lowest vibrational level for each electronic state.

A molecule can move from one to another energy level through the absorption and emission of photons, or through non-radiative energy exchanges with their environment. The colored arrows in the Jablonski diagram depict various radiative (solid lines) and non-radiative (dashed lines) transitions that can take place.

At room temperature, a molecule is typically found in the lowest vibrational level of the ground state initially. When it absorbs a photon, the molecule is promoted into the excited state manifold (red). This vibronic transition occurs practically instantaneously ($\sim 10^{-15}$ s). From S_1, the molecule dissipates energy into its nano-environment through vibrational relaxation to reach the lowest excited state energy level ($\sim 10^{-12} - 10^{-10}$ s).

There are several possibilities for what can happen from here for the molecule to eventually reach the ground state again. On the one hand, the molecule can
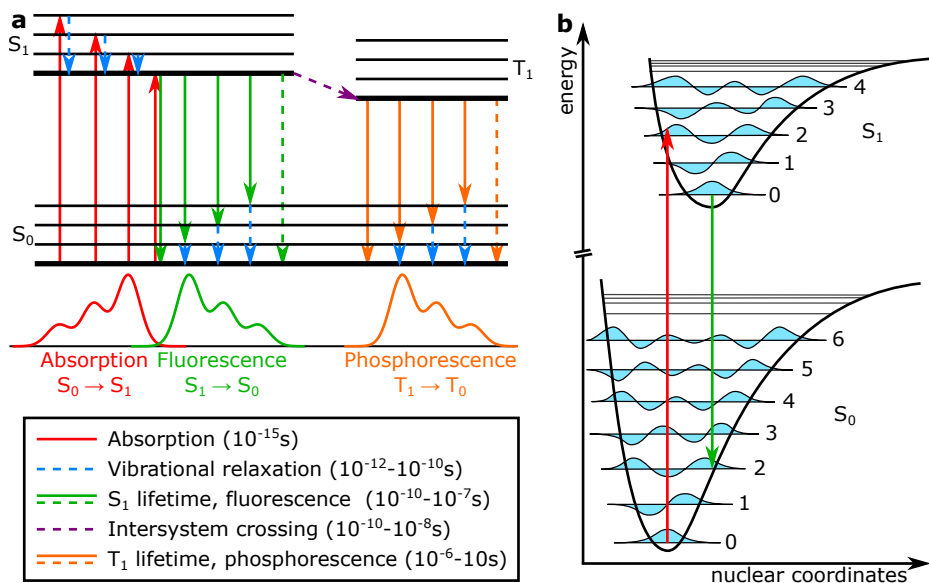
Figure 1.1: *Molecular energy diagrams.* **(a)** Jablonski diagram. Radiative (solid lines) and non-radiative (dashed lines) transitions that take place in a molecule with ground state S_0, first excited state S_1 and first triplet state T_1. The different pathways and time scales are listed at the bottom. The corresponding spectra sketched, the broadened shape accounting for the energy uncertainty. **(b)** Franck-Condon principle energy diagram. The ground and first excited singlet states S_0 and S_1 together with their vibrational levels (light blue) and an absorption (red) and emission (green) transition. (Adapted from [62]).

relax to the ground state manifold through the spontaneous emission of a photon (i.e. fluorescence), or via a non-radiative decay ($\sim 10^{-10} - 10^{-7}$ s). On the other hand, it may transition into T_1 via intersystem crossing ($\sim 10^{-10} - 10^{-8}$ s). From the lowest T_1 state, it will eventually relax back to the ground state via the spontaneous emission of a photon (i.e. phosphorescence), or via a non-radiative decay ($\sim 10^{-6} - 10$ s). While the molecule is trapped in the triplet state, it cannot emit any photons, which is why it is also known as the "dark state" of the molecule. Regardless of how the system arrived to the ground state manifold, vibrational relaxation will bring the molecule back to the lowest vibrational state of S_0.

A molecule only absorbs or emits light at wavelengths that correspond to the energy difference of molecular transitions. They are probed by molecular spectroscopy. Not all of the transitions between energy levels are equally probable. The stronger the transition probability for a certain energy difference is, the stronger the recorded signal will be. An illustrative absorption, fluorescence, and phosphorescence spectra at room temperature are sketched below the Jablonski diagram. It shows how the vibronic transitions lead to the different signal intensities. It is sketched as a continuous spectrum instead of discrete lines due to the uncertainty principle linking excited state lifetime with transition energy.

The Franck-Condon principle helps to understand and quantify the transition probabilities. The probability for a vibronic transition between two quantum mechanical states Ψ_i and Ψ_f to happen is given by $P_{i \to f} = \left| \left\langle \Psi_f \middle| \mu \middle| \Psi_i \right\rangle \right|^2$. The molecular dipole operator $\mu = \mu_e(r) + \mu_N(R)$ depends on the position of the electrons (r) and of the nuclei (R). The wave functions of the initial and final states depend on both coordinates. The Born-Oppenheimer approximation allows to rewrite Ψ as the product of the electronic ψ and vibrational φ wave function where the vibrational one only depends on the nuclear coordinates $\Psi(r, R) \approx \psi(r, R)\varphi(R)$. Additionally, the electronic transition occurs on a time scale that is short compared to nuclear motion so that the transition probability can be approximated by a constant R. In other words,

$$P_{i \to f} = \left| \left\langle \Psi_f \middle| \mu \middle| \Psi_i \right\rangle \right|^2 \tag{1.1a}$$

$$\approx \left| \left\langle \psi_f \varphi_f \middle| \mu_e \middle| \psi_i \varphi_i \right\rangle \right|^2 \tag{1.1b}$$

$$\approx \underbrace{\left| \left\langle \psi_f \middle| \mu_e \middle| \psi_i \right\rangle \right|^2}_{\substack{\text{transition} \\ \text{dipole moment}}} \quad \underbrace{\left| \left\langle \varphi_f \middle| \varphi_i \right\rangle \right|^2}_{\substack{\text{Franck-Condon} \\ \text{factor}}} \tag{1.1c}$$

The transition dipole moment $\mu_{if} = \left\langle \psi_f \middle| \mu_e \middle| \psi_i \right\rangle$ expresses the transition strength of the electronic transition. The absorption cross-section σ_{abs} of the molecule is proportional to $\left| \mu_{if} \right|^2$. Due to its vectorial nature, the value depends on the alignment of the polarization of the light with the transition dipole moment of the molecule. The Franck-Condon factor calculates the overlap between the initial and final vibrational wave function φ. The larger the overlap, the more likely the transition.

Figure 1.1b depicts an alternative way to draw energy diagrams based on the Franck-Condon principle. The electronic ground and excited state S_0 and S_1 are drawn as potential wells alongside the wave functions of their lowest lying vibrational levels. Due to the assumption that the nuclear coordinate R does not change during the transition, both absorption (red) and fluorescence (green) can be drawn as vertical arrows. For both the absorption and fluorescence transitions, the vibrational wave functions overlap well, leading to large Franck-Condon factors and thus peaks in the absorption and fluorescence spectrum. The arrow for the fluorescence transition is shorter than that for the absorption spectrum, which is why fluorescence spectra have a lower energy than absorption spectra. The molecular structural conformation of S_0 and S_1 are often very similar, resulting in absorption and emission spectra that are almost mirror images of one another. The distance between the maxima of the first absorption and emission band is known as the Stokes shift.

After photoexcitation, the different relaxation pathways all compete with one another. Their interplay is expressed by rate constants k. For the processes that were drawn in the Jablonski diagram they are the fluorescence (k_f), non-radiative decay (k_{nr}), and intersystem crossing (k_{ic}) rate constants. The efficiency of the pathways

can then be calculated as a ratio between them. For example, even though the intersystem crossing and the fluorescence relaxation pathway happen at roughly the same time scale, the probability of a transition to the triplet state typically only happens in $\sim 10^6$ of the cases due to the spin mismatch between the two states involved. Although $k_{ic} \ll (k_f + k_{nr})$, the efficiency of fluorescence is still competing with non-radiative decay channels. Thus, the fluorescence quantum yield Φ_{fl} can be expressed by the ratio between the different decay rates as

$$\Phi_{fl} = \frac{k_f}{k_f + k_{nr} + k_{ic}}. \tag{1.2}$$

Both absorption and emission spectra can be probed experimentally. They are fundamentally different. As is already apparent from figure 1.1a, the absorption spectrum maps the excited state manifold S_1, while the fluorescence spectrum probes the ground state manifold S_0. An absorption spectrum measures the decrease in light intensity at the wavelengths at which the molecule absorbs more light, making it a differential measurement where the excitation wavelength equals the detected wavelength. In contrast, fluorescence can be measured directly due to the spectral separation between the excitation wavelength and the fluorescence spectrum. The shape of the fluorescence emission spectrum is independent of the excitation wavelength λ_{ex} since it always takes place from the lowest excited state. However, its strength depends on it through the absorption cross-section $\sigma_{abs}(\lambda_{ex})$. The more light gets absorbed at a certain λ_{ex}, the larger the fluorescence spectrum. In excitation spectroscopy, this relationship is utilized to indirectly measure the absorption spectrum through fluorescence detection. It is exploited in Chapters 2 and 3 to map the excited state manifold of different molecules at room temperature along with fluorescence spectra that probe the ground state manifold.

1.1.1 Pump-probe microscopy

Fluorescence excitation and emission spectroscopy both rely on the detection of spontaneous fluorescence emission. Still, not all molecules fluoresce efficiently. That is why Chapter 4 explores stimulated emission, a pump-probe technique that does not depend on fluorescence detection. In pump-probe microscopy, the molecule is brought into the excited state by an excitation (pump) beam. A second (probe) beam then probes the effect of this pump beam on the molecule. The transmitted probe light in absence of the pump beam, T_{off}, differs from that when the pump beam is on, T_{on}. This change in transmitted power can be expressed as:

$$\Delta T = T_{on} - T_{off}. \tag{1.3}$$

The probe beam instantaneously brings the molecule into a different state, so that the $\sim$ ns lifetime of fluorescence detection is overcome. ΔT can take either positive
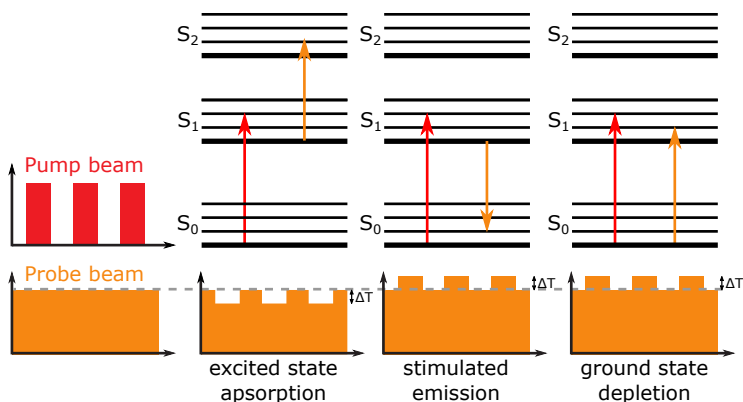
Figure 1.2: *Pump-probe microscopy.* The intensity of the unmodulated probe beam (orange) changes due to the modulated pump beam (red). Excited state absorption (left) reduces the probe beam intensity, while stimulated emission (center) and ground state depletion (right) increase it.

or negative values depending on the process that is tested. The different processes that can be observed are called excited state absorption, stimulated emission, and ground state depletion. They are sketched in figure 1.2 where the modulated pump beam is drawn as red and the probe beam as orange arrow.

In excited state absorption (left), the pump beam excites the molecule into S_1. The probe beam then excites the system even further into a higher excited electronic state S_2. Without the pump beam present, the probe beam would not have reacted with the molecule. Therefore, more probe light is absorbed when the pump beam is on, and $\Delta T < 0$.

A molecule in an excited state can be stimulated down to the ground state by a photon at a wavelength corresponding to a transition to the ground state in a process called stimulated emission (center). The emitted photon has the same phase, wavelength, polarization, and travel direction as the incoming photon. The additional photon created by stimulated emission increases the probe beam intensity when the system has been brought into the excited state by the pump beam first, so that $\Delta T > 0$. Stimulated emission will be explained in more detail in chapter 4, where it is tested on single molecules.

Ground state depletion (right) can be observed when both pump and probe beam are resonant with the absorption band of the molecule. Whenever the pump beam excites the molecule into the excited state, the transition becomes unavailable for the probe beam. Therefore, more probe beam is transmitted in the presence of the pump beam and $\Delta T > 0$.

All these three processes bring the system into a different state instantaneously. When measured with pulsed laser beams with a sufficient temporal resolution, they can beat the $\sim$ ns temporal response governed by fluorescence emission.
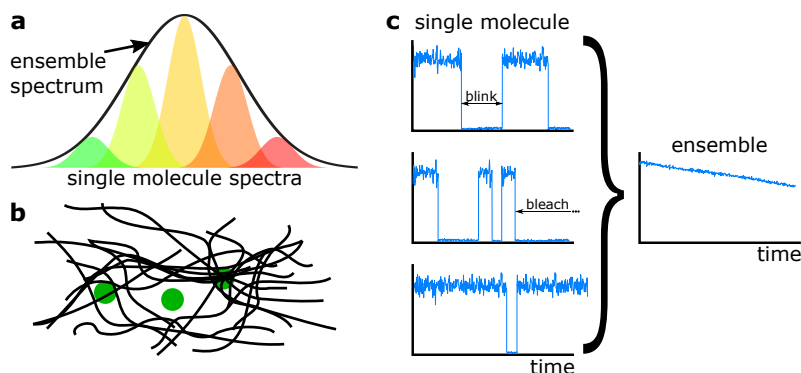
Figure 1.3: *Single molecule motivation.* Going to the single molecule level **(a)** lifts the ensemble average, **(b)** probes the nanoenvironment, and **(c)** unveils dynamic processes.

Photothermal microscopy can be considered as a special form of pump-probe microscopy. After excitation by a pump beam, a molecule transmits heat into its nanoenvironment whenever it relaxes through a non-radiative process. This creates a temperature gradient around the molecule, which alters the local refractive index of the surrounding medium. The probe beam scatters on the refractive index gradient. The scattering can both increase and decrease the amount of transmitted light that is detected depending on various experimental parameters. That is why ΔT can take positive or negative values in photothermal microscopy. A more in-depth explanation of this effect and the parameters which influence it will be covered in chapter 5, where it is studied on gold nanoantennas.

1.2 Single molecules

Single molecule studies come with certain peculiarities that are hidden in ensemble measurements, and which have been addressed in many reviews and books[16, 23, 49, 63–65]. In this section, a motivation for single molecule measurements and an overview over the main spectral features that emerge at the single molecule level are presented.

Single molecules are single quantum emitters, which implies the absorption and emission of only one photon at a time. This leads to weak signals that require very sensitive detection techniques. These are typically based on fluorescence detection, since it is background free due to the spectral separation from the excitation wavelength. Only at the single molecule level, the variability and dynamics of individual molecules emerges from the ensemble average. The main features will be discussed in the following.

Spectra are typically not narrow lines at the exact transition energy, but are broadened significantly. The uncertainty principle links the excited state lifetime to the

transition energy. Therefore, the shorter the lifetime, the larger energy uncertainty. This leads to homogeneous broadening of the spectra and is intrinsic to the molecule. In addition, inhomogeneous broadening also occurs. No two molecules have exactly the same spectral shape and position. Differences are either extrinsic, like changes in the molecule's surrounding medium and temperature[66, 67], or intrinsic, like conformational changes[31, 33, 68]. They can occur spontaneously or be photoinduced. In an ensemble measurement, this variability is reflected by an inhomogeneously broadened spectrum. This is sketched in figure 1.3a, where a distribution of homogeneously broadened single molecule spectra (colored) lead to a significantly broader ensemble spectrum (black contour).

Experiments have already shown that the spectral position can shift by more than 100 nm from molecule to molecule, often accompanied by significant changes in the spectral shape[30, 31, 69, 70]. Especially molecular conformations with a weaker spectrum or that occur less frequently will be lost in the ensemble. That is why it is necessary to go to the single molecule level to unravel the full spectral distribution of a molecule population.

One of the consequences of the spectral spread due to external factors is that single molecule spectra are an excellent readout to probe their nanoenvironment. In a typical experiment, single molecules are embedded in a rigid polymer matrix as sketched in figure 1.3b[71, 72]. They might be slightly trapped, not trapped at all or completely restricted by this polymer (left to right in sketch). This may lead to drastic differences in their energy level distribution, which translates into spectral differences.

Moreover, certain molecular aspects only become visible at the single molecule level. For instance, while trapped in a long-lived dark state, a molecule cannot emit light. This phenomenon is known as blinking (or fluorescence intermittency) and it is one of the most studied single molecule phenomena[33, 73–79]. Eventually, the continuous photo-excitation of the molecule will lead to its irreversible destruction, called photobleaching. From this moment onward, no more photons are emitted. Figure 1.3c exemplifies both blinking and photobleaching events. On the left hand side, the fluorescence count rate is recorded in a timetrace for three different molecules. All three traces show a constant number of fluorescent counts intermitted by periods of no counts when the molecules are temporarily trapped in a dark state. From top to bottom, the first and second molecule stop emitting entirely at some point, which means that they got photobleached. Different processes lead to blinking and bleaching. They depend strongly on the molecule under investigation as well as the experimental conditions under which they are measured, including excitation power, wavelength, and the environment[68, 80].

Only single molecules blink and bleach in one discrete step without any intermediate levels. The presence of a second molecule in the focus would already lead to

a two-step blinking or bleaching behavior. In an ensemble measurement, blinking of different molecules at random time intervals leads to an overall lower fluorescence intensity as compared to the case of non-blinking molecules. Moreover, in an ensemble measurement, photobleaching is visible as a gradual decline in emission intensity and any single molecule dynamics is hidden. This is sketched on the right hand side of figure 1.3c.

Although discrete blinking and photobleaching are all signatures of single molecules, antibunching measurements are the more rigorous way to confirm the single quantum emitter nature of a recorded signal[81–83]. It is based on photon counting statistics. It measures the time delay τ between two incident photons in a Hanbury Brown and Twiss setup, in which the emitted light is split onto two single photon sensitive detectors with a 50/50 beamsplitter. Since a single molecule can only emit one photon at a time, it is highly improbable to detect a photon on both detectors at the same time, while there is a finite probability to detect them for any non-zero time delay. This dip in photon coincidences at $\tau = 0$ is known as antibunching and it is expressed by the second-order intensity correlation function

$$g^{(2)}(\tau) = \frac{< I(t) >< I(t + \tau) >}{< I(t) >^2},$$
(1.4)

where the pointy brackets denote the time average. In an ideal scenario of a background-free single molecule measurement, $g^{(2)}(\tau = 0) = 0$, which leads to a dip in the correlation function at zero time delay.

Since antibunching is an intensity measurement, it can be integrated into the recording of the actual data in any intensity based measurement. The full signal is recovered when adding up the intensities of the two photodetectors. However, the dark counts intrinsic to each detector would also be added up, making it noisier. Especially for single molecules with a low fluorescence quantum yield, this may result in the signal disappearing into the noise. Also, antibunching intensity measurements are not compatible with spectrally resolved measurements like fluorescence spectroscopy. Additionally, the use of two detectors makes the setup and its alignment more involved. All of this combined is why the more straightforward observation of single step blinking or photobleaching events was selected as the method of choice for single molecule verification throughout the thesis. Thus, the measurements in this thesis were carried out until the molecule either blinked or photobleached.

Another effect that emerges only at the single molecule level is spectral diffusion[21, 71, 84, 85]. It summarizes the processes that lead to a change in the molecule's spectrum over time. Small variations in the molecule's interaction with its environment, for example due to the heating, leads to gradual conformational changes in time, called spectral wandering. Abrupt spectral jumps affecting the shape, position or intensity of the spectrum can also occur[30, 74, 86]. They either appear randomly or are photoinduced.

1.3 Single molecule detection

Generally speaking, there are only a couple of requirements for the successful detection of single molecules. No more than one molecule should be resonant in the detection volume at once, and the signal-to-noise ratio should be such that the measured signal stands out of the background before photobleaching occurs. For the first requirement, the sample can always be diluted until only one molecule is present in the excitation volume at a time. However, smart detection schemes are necessary to simultaneously satisfy the second requirement. In practice, a combination of a small detection volume and techniques that warrant low noise and background levels are chosen. They will be discussed in this section.

Single molecule measurements have come a long way since the first detection of a single molecule through absorption[20] and fluorescence excitation[21] at cryogenic temperatures some 30 years ago. At cryogenic temperatures, the absorption cross-section of zero-phonon lines of $\sim 10^{-11}$ cm^2 is about two orders of magnitude smaller than the beam waist area of a focused beam $\propto \lambda_{exc}^2 \sim 10^{-9}$ cm^2. This means that under ideal conditions one in every 100 photons is absorbed. In contrast, fluorescence detection is practically background free due to the spectral separation between the excitation wavelength and the Stokes-shifted fluorescence. That is why it was the method of choice for most subsequent single molecule experiments, which routinely measured both excitation and emission spectra at cryogenic temperatures. However, a drawback of fluorescence detection is the limitation to fluorescing molecules.

At room temperatures, single molecules can be studied in a more natural environment than at cryogenic temperatures. However, the broadening of the absorption bands at higher temperatures decreases the absorption cross-section by 5 to 6 orders of magnitude compared to the zero-phonon line at low temperatures to $\sigma_{abs} \sim 10^{-16}$ cm^2[87]. This means that only one in every 10^7 will excite the molecule. Together with a decreased photostability, this drastic reduction in signal strength puts a major constraint onto all room temperature measurements. Only time and detection efficient spectroscopic schemes are feasible at this temperature regime. The development of near-field imaging reduced the detection area to sub diffraction spot sizes[24], though at the cost of the plasmonic near-field tip influencing the photophysical properties of the molecules. The incorporation of a confocal microscope[25, 28] enabled non-invasive detection with diffraction-limited resolution. All of the experiments presented in this thesis make use of a confocal microscope whose working principle is explained in more detail in the next section.

Owing to the low signal levels and photostability, only fluorescence emission spectra were routinely measured at room temperature so far. Excitation spectra have only recently been introduced in proof-of-principle studies by scanning a narrow-

band laser across the absorption band[32, 42, 43]. Remembering that excitation and emission spectra probe different electronic states, excitation spectroscopy is a very valuable addition to the already existing methods. The combination of the two techniques could for example probe if conformational changes affect the ground and excited vibrational manifolds differently. Chapter 2 introduces Fourier transform spectroscopy to the single molecule regime to measure excitation alongside emission spectra. In chapter 3, it is successfully performed on single light harvesting complexes, which are weak fluorescence emitters, demonstrating its maturity beyond proof-of-principle studies.

The fs dynamics of single molecules have already been probed indirectly through fluorescence detection by pump-probe experiments. These experiments include measurements of energy redistributions over different vibrational modes[45, 88], and quantum coherences in the excited state manifold [46, 89, 90]. To measure these effects directly, a 10^7 signal-to-background ratio has to be overcome at room temperature due to the small absorption cross-sections of single molecules. Both ground state depletion[44] and photothermal contrast[49] have already reached single molecule sensitivity, while stimulated emission experiments have been performed on a handful of molecules as well[91]. Despite the challenges of overcoming the large background signal, pump-probe experiments are the gateway to directly probe the fs dynamics of the excited state manifold without being dependent on fluorescence. This will be the focus of chapter 4, where a setup was developed to push the sensitivity of stimulated emission measurements to the single molecule level.

1.3.1 Confocal microscopy

All the experiments presented in this thesis required the same three basic ingredients: a light source, a confocal microscope including the sample, and a detector. These individual ingredients were adapted according to the unique demands of each specific experiment. The confocal microscope was at the heart of all experiments. Laser light gets focused tightly into a diffraction limited spot over which the sample is scanned, instead of illuminating the entire region of interest at the same time as in wide-field microscopy. It relies on the rejection of out-of-focus light, leading to improved signal-to-background ratios due to background reduction.

Figure 1.4a shows the working principle of a confocal microscope. A collimated beam is focused onto the sample through a microscope objective (red beam). The sample typically consists of molecules on top of a glass coverslip. The fluorescence emitted by the molecules is then collected through the same objective and focused onto a small aperture (green beam). An avalanche photodiode (APD) serves as the aperture due to its small active area. This aperture will cut all fluorescence components originating from parts of the sample that are out-of-focus away (dashed
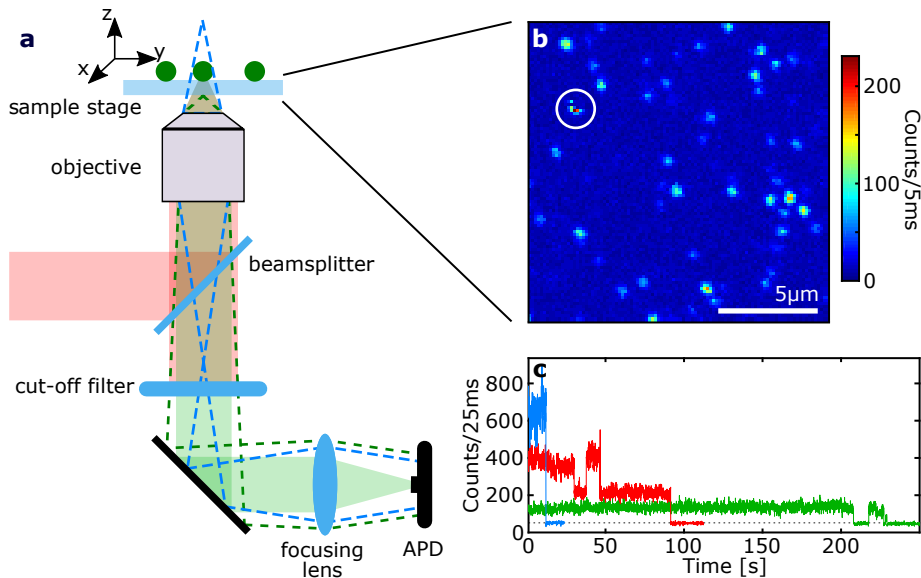
Figure 1.4: *Confocal microscope.* **(a)** The collimated excitation beam (red) is focused onto the sample through the objective. The fluorescence response of the particles (green) is collected through the same objective and focused onto the APD. The cut-off filter blocks any scattered excitation light. Out-of-focus signal (green and blue dashed lines) is not focused onto the APD. **(b)** Confocal image, where each diffraction limited spot corresponds to the fluorescence detection from individual molecules. **(c)** Time trace of 3 different single molecule spots on the confocal image. The dashed line corresponds to the background counts.

lines). A spectral filter is added to detection path to block any scattered excitation light.

The diffraction limit defines the fundamental limit of resolution of the microscope as the minimum distance between two point sources that can still be distinguished. The larger the angle of the focus, the tighter the focus and the better the resolution. The numerical aperture (*NA*) is a quantitative measure for the maximum collection angle of an objective as $NA = n \sin(\theta)$, where n is the refractive index of the medium between the objective and the sample and θ the half angle of the focus.

The diffraction limit d for both the lateral and axial dimensions of the focus can be approximated by the Rayleigh criterion[92]. It states that two sources can be distinguished whenever the position of the maximum signal of one overlaps with the position of the first minimum of the other. Assuming a uniform beam, the distance between the central maximum and the first minimum of the Airy disk is

$$d_{lateral} = \frac{0.61\lambda}{NA}, \tag{1.5a}$$

$$d_{axial} = \frac{2\lambda}{NA^2}. \tag{1.5b}$$

The diffraction limit is closely related to the radius of the spot size. It therefore also serves as a good first approximation for the beam waist radius in the focus. According to equation (1.5), the larger the *NA*, the smaller the focal volume. One way to increase the *NA* is by using a medium with a high refractive index *n* between the objective and the sample. That is why an oil immersion objective was used to focus the beam onto the sample in all experiments. To study larger areas, the sample is placed onto a 3D piezoelectric scanner and raster-scanned through the focus with nanometer resolution.

Confocal microscopy is a very popular technique for single molecule experiments due to its high spatial resolution and good contrast. However, since it is based on point excitation and detection it requires scanning the sample to probe a larger region. In contrast, wide-field microscopy illuminates and probes the entire focal volume at once, though with a lower signal-to-background ratio. Still, it is a more suitable technique for experiments which require a wide field of view such as in single particle tracking[93].

1.3.2 A typical single molecule measurement

Whenever a new sample was placed onto the microscope, an evaluation and, if necessary, adjustments of the alignment of the confocal microscope took place. For this, a small sample area was raster-scanned in the xy-plane, while the fluorescence counts at each pixel were recorded with the APD. Fluorescent molecules stood out as bright spots on the resulting image. By positioning one of these bright spots into focus using the piezoelectric stage, the alignment of the system was optimized iteratively under the assumption that a larger number of fluorescence counts on the APD corresponded to a better alignment. Firstly, the position of the sample was optimized in all three dimensions. Secondly, the position of the APD was moved in all three dimensions to overlap its active area with the focus of the lens in the detection path. These two steps were repeated until the optimum was reached.

When recording a confocal image, the bright spots now have a diffraction limited size. An exemplary optimized image of quatterylene diimide (QDI) molecules is shown in figure 1.4b. These rylene based dye molecules were studied in chapter 2, where more can be learned about them. From the confocal image, it can already be seen that not all spots have the same fluorescence intensity. Due to the use of circularly polarized light, the transition dipole moments of all molecules were excited with the same probability. That is why the intensity differences are most likely due to molecules in different conformations, which leads to changes in their absorption cross section at the excitation wavelength $\sigma_{abs}(\lambda_{exc})$ and a different fraction of fluorescence counts being blocked by the cut-off filter.

The spot that has been circled in figure 1.4b is not circular, but appears to have part of the top half missing. This is due to blinking. It can be better observed when focus-

ing onto a molecule and recording the total fluorescence counts in time. Figure 1.4c shows three representative time traces of QDI molecules where the background level is indicated by the dashed line. The red trace shows a two-step blinking and bleaching process, the signature for two molecules being excited simultaneously. The blue trace emits very efficiently, giving a large number of fluorescence counts, but bleaches very rapidly. The green trace gives fewer counts than the previous one, but fluoresces for a longer time. Towards the end of the trace, it shows one-step blinking and then, discrete bleaching. The one-step blinking and bleaching of the latter two traces are signatures for single molecules.

Up to $600 \, \text{counts}/25\text{ms} = 2.5 \times 10^4$ counts/s were recorded by the APD for the single molecules in the time traces. This value will be compared to the theoretically achievable fluorescence counts. The molecules were excited with a helium-neon laser at 633 nm using an $1.3 \, NA$ objective. According to equation (1.5a), this results in a diffraction limited beam waist radius of 300 nm, which agrees well with the spot sizes seen on the confocal image. From this radius, the beam area in the focus can be calculated as $A = \sim 3 \times 10^{-9} \, \text{cm}^2$. The absorption coefficient of QDI is about $\epsilon = 25\,000 \, \text{M}^{-1} \, \text{cm}^{-1}$ at 633 nm[94]. σ_{abs} can be approximated from it as $\sigma_{abs} \approx \ln(10)\epsilon/\text{N}_\text{A} \approx 1 \times 10^{-16} \, \text{cm}^2$, with N_A Avogadro's number. This means that the molecule only absorbs one in every 3×10^7 photons. For a photon density of 1×10^{22} counts/s/cm^2 of the excitation beam in the focus (corresponding to approximately 10 μW excitation power), and under the assumption that all absorbed light will generate a fluorescence photon ($\Phi_{fl} = 1$), this would lead to 1×10^6 counts/s fluorescence, almost two orders of magnitude larger than the detected counts.

Different factors still need to be taken into account to estimate the emitted fluorescence that reaches the APD. The objective only transmits ~80 % of the light, the 50/50 beamsplitter and the long-pass filters in the detection path both block about half of the fluorescence. Finally, the quantum yield of the APD is ~60 % at 633 nm. Combined, they already account for one order of magnitude reduction in fluorescence counts. The remaining difference is at least partially due to a fluorescence quantum yield of less than unity and the collection angle of the objective. All in all, the fluorescence detection efficiency of the setup is around 5-10 %.

A molecule can only emit a limited amount of photons before it photobleaches. For most molecules, this number lies around 10^6-10^7 photons[95–97]. Assuming an average lifetime of 100 s, this would yield the total amount of 2.5×10^6 photons emitted using the recorded data, or 1×10^9 photons using the calculated value.

This covered all of the concepts of single molecule detection relevant to this thesis. They will come back in the descriptions and interpretations of the experiments in the following chapters.

1.4 Fourier transform spectroscopy

The measurement of excitation spectra in chapters 2 and 3 are based on Fourier transform spectroscopy. Due to the novelty of this method in single molecule research, its theoretical background, as well as some practical considerations, are introduced here.

Scanning two identical beams across one another in time changes the phase difference between them. This results in an interference pattern that oscillates between twice the intensity of the individual beam for constructive interference and zero intensity for destructive interference. The properties of the interference pattern measured in the time domain are directly related to the spectrum of the beams in the frequency domain through a Fourier transformation. This relationship is exploited in Fourier transform spectroscopy, which relies on an interferometric measurement using a broadband light source that covers the entire spectral band at once. This is opposed to measurements in the spectral domain, where a narrowband tunable light source performs a wavelength scan over the absorption band.

1.4.1 The interference of light

The discussion of Fourier transform spectroscopy presented here loosely follows the book of Kauppinen and Partanen on the same topic[98]. The general Fourier-pair relationship between the interference of light and the corresponding spectrum is derived and the results interpreted in terms of excitation spectroscopy.

Monochromatic electromagnetic waves can be described as

$$\mathbf{E}(\mathbf{r}, t) = E_0 e^{i(\mathbf{k}\cdot\mathbf{r} - \omega t)}, \tag{1.6}$$

with E_0 the amplitude, $\mathbf{k}$ the wave vector, and $\mathbf{r}$ the position vector. The angular frequency ω of the wave is typically too high to directly detect it and the intensity of the wave is recorded instead. In case of in-plane waves, it is quadratically proportional to the amplitude of the electromagnetic wave: $I \propto \mathbf{E}^2$.

An interferogram records the intensity of the sum of two electromagnetic waves. If the two waves $\mathbf{E}_1$ and $\mathbf{E}_2$ are identical except for a phase difference δ, then $\mathbf{E}_2 = \mathbf{E}_1 \exp(i\delta)$. Then the intensity becomes $I \propto (\mathbf{E}_1 + \mathbf{E}_2)^2 = 2E_0^2(1 + \cos(\delta))$ and following a sinusoidal pattern as a function of δ. The phase difference δ can be expressed in many different ways. The mathematical description of Fourier transformations often does it in terms of interpulse time delay Δt and angular frequency $\omega = 2\pi/\Delta t$ such that $\delta = \omega\Delta t$. However, in Fourier transform spectroscopy it is more common to talk about optical path length differences $x = c\Delta t$ with c the speed of light and wavenumbers $\tilde{\nu} = 1/\lambda = \omega/2\pi c$ so that $x = 1/\tilde{\nu}$. From this follows that $\delta = 2\pi x \tilde{\nu}$.

With $I_0 = E_0^2$, the intensity can be rewritten as $I(x, \tilde{v}) = 2I_0(\tilde{v})[1 + \cos(2\pi x\tilde{v})]$. This interfering intensity measurement $I(x, \tilde{v})$ is called the interference record. It can be transformed into the interferogram $\mathcal{I}(x, \tilde{v})$ by dropping the constant offset $2I_0(\tilde{v})$ so that the interference oscillates around zero:

$$\mathcal{I}(x, \tilde{v}) = 2I_0(\tilde{v})\cos(2\pi x\tilde{v}). \tag{1.7}$$

For each value of $\tilde{v}$, a sinusoidal wave that oscillates between 0 and $4I_0(\tilde{v})$ is obtained when scanning through x with its own periodicity. In the case of a light source with a continuous spectrum $\mathcal{S}(\tilde{v})$, all colors are in phase only at $x = 0$. That is why it is necessary to integrate over all $\tilde{v}$ in order to obtain the intensity at a specific path length difference x. For an infinitesimally small spectral component $d\tilde{v}$, $I_0(\tilde{v}) = \mathcal{S}(\tilde{v})d\tilde{v}$ such that equation (1.7) becomes

$$\mathcal{I}(x) = 2\int_0^\infty \mathcal{S}(\tilde{v})\cos(2\pi\tilde{v}x)d\tilde{v}. \tag{1.8}$$

A further simplification is to mirror the spectrum for negative wave numbers to create a symmetrical integral with $\mathcal{S}(\tilde{v}) = \mathcal{S}(-\tilde{v})$ as

$$\mathcal{I}(x) = \int_{-\infty}^\infty \mathcal{S}(\tilde{v})\cos(2\pi\tilde{v}x)d\tilde{v} = \int_{-\infty}^\infty \mathcal{S}(\tilde{v})e^{-i2\pi\tilde{v}x}d\tilde{v} = \mathcal{F}\{\mathcal{S}(\tilde{v})\}. \tag{1.9}$$

The second integral already has the shape of a Fourier transform, indicated by the operator $\mathcal{F}$. The Fourier transform pair $\mathcal{I}(x)$ and $\mathcal{S}(\tilde{v})$ consequentially is:

$$\mathcal{I}(x) = \int_{-\infty}^\infty \mathcal{S}(\tilde{v})e^{i2\pi\tilde{v}x}d\tilde{v} = \mathcal{F}\{\mathcal{S}(\tilde{v})\}, \tag{1.10a}$$

$$\mathcal{S}(\tilde{v}) = \int_{-\infty}^\infty \mathcal{I}(x)e^{-i2\pi\tilde{v}x}dx = \mathcal{F}^{-1}\{\mathcal{I}(x)\}. \tag{1.10b}$$

In short, equation (1.10a) expresses the intensity as a function of the difference in path length, i.e. the interferogram whereas equation (1.10b) denotes the variation in intensity as a function of wavenumber, i.e. the spectrum.

1.4.2 Fourier transform spectroscopy

Fourier transform spectroscopy exploits the relationship between the temporal and spectral domain as described by equation (1.10). Depending on how the experiment is set up, different types of spectra can be measured. This will be discussed in the following, with a special emphasis on excitation spectra. The simplest example for an interferometric measurement is the laser autocorrelation. The interferogram $\mathcal{I}_{las}(x)$ represents the interferogram of the laser with itself. Its Fourier transformation immediately yields the laser spectrum.$\mathcal{S}_{las}(\tilde{v})$. Similarly, though not as
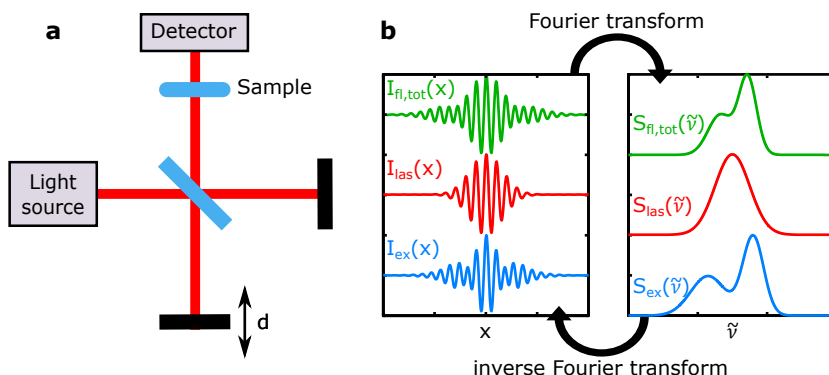
Figure 1.5: *Fourier transform spectroscopy.* **(a)** Sketch of an interferometer, where the two interfering beams pass through the sample before detection. **(b)** The temporal (left) and spectral (right) domain are related through a Fourier transformation. When the laser (red) and total (green) signal are known, the excitation spectrum (blue) can be obtained via deconvolution in the time domain (left) or division in the spectral domain (right) of the total by the laser signal.

common, an emission spectrum can be measured by interfering the fluorescence response of the system with itself[99, 100].

It is also possible to obtain absorption spectra using Fourier transform spectroscopy. For example, Fourier transform infrared spectroscopy (FTIR) is a well-established technique to measure absorption spectra of ensembles in the infrared spectral region[101]. As sketched in figure 1.5a, broadband light source overlapping with the spectral region of interest is propagated through the interferometer. One of the two arms has a movable mirror, whose displacement d corresponds to half the path length difference x. The recombined interfering beam interacts with the sample before being detected. Now, the measured interferogram $\mathcal{I}_{meas}(x)$ depends on both the absorption spectrum of the molecule $\mathcal{S}_{abs}(\tilde{\nu})$ and the spectrum of the excitation beam $\mathcal{S}_{las}(\tilde{\nu})$. In the spectral domain, the measured signal would simply be the product between the two $\mathcal{S}_{meas}(\tilde{\nu}) = \mathcal{S}_{abs}(\tilde{\nu}) \cdot \mathcal{S}_{las}(\tilde{\nu})$. With the convolution theorem $\mathcal{F}\{A \cdot B\} = \mathcal{F}\{A\} * \mathcal{F}\{B\}$, this turns into a convolution for the interferogram: $\mathcal{I}_{meas}(x) = \mathcal{I}_{abs}(x) * \mathcal{I}_{las}(x)$.

The same relationship as for absorption spectra holds for excitation spectroscopy, with the difference that an interferogram of the fluorescence intensity is measured instead of the attenuation of the transmitted beam:

$$\mathcal{I}_{fl,tot}(x) \propto \mathcal{I}_{ex}(x) * \mathcal{I}_{las}(x), \tag{1.11a}$$

$$\mathcal{S}_{fl,tot}(\tilde{\nu}) \propto \mathcal{S}_{ex}(\tilde{\nu}) \cdot \mathcal{S}_{las}(\tilde{\nu}). \tag{1.11b}$$

The different components of equation (1.11) are modeled in figure 1.5b using a Gaussian laser spectrum and a double-Gaussian fluorescence excitation spectrum. On the left hand side, the interferograms are shown. The total fluorescence signal, $\mathcal{I}_{fl,tot}(x)$ (green), and the laser spectrum, $\mathcal{I}_{las}(x)$ (red) would be measured in an

experiment. The excitation spectrum $\mathcal{S}_{ex}(\tilde{\nu})$ can be obtained in two ways from here. First, the excitation spectrum, $\mathcal{I}_{ex}(x)$ (blue) can obtained via a deconvolution and the result Fourier transformed into the spectral domain. Second, $\mathcal{I}_{fl,tot}(x)$ and $\mathcal{I}_{las}(x)$ are Fourier transformed and then the product spectrum $\mathcal{S}_{fl,tot}(\tilde{\nu})$ divided by the laser spectrum $\mathcal{S}_{las}(\tilde{\nu})$.

A division is easier to realize than a deconvolution, so that in the experiments the ratio of the two spectra will be taken to obtain the excitation spectrum. Still, in both cases the spectrum of the laser is the only additional component that is required in order to retrieve $\mathcal{S}_{ex}(\tilde{\nu})$. Though not a common method for excitation spectroscopy, it has already been applied successfully in ensemble measurements[102, 103].

The simultaneous sampling of all wavelengths makes Fourier transform spectroscopy fast compared to spectral measurements with the same resolution, which is the same as to say with a higher signal-to-noise ratio for the same integration time. This is known as the Fellgett's advantage[104] which makes Fourier transform spectroscopy good choice for measurements dealing with low signal levels and a limited time window. Another advantage is that the $\tilde{\nu}$ of different spectra can be known very accurately, making it easy to average them[105]. A drawback is that it is more mathematically involved to obtain spectra through a Fourier transformation. Overall, Fourier transform fluorescence excitation spectroscopy is a very general technique which can in principle be applied to any fluorescing system as long as a measurement can be performed within the time window dictated by photobleaching.

1.4.3 Discretization

It is impossible to record an interferogram with an infinitesimally small step size over infinitely long path length differences as equation (1.10) may suggest. This section considers how the mathematical description for the Fourier pair of equation (1.10) can be adapted to reflect an actual measurement. It discusses the effect of sampling on the recorded data and how signal processing beyond the Fourier transformation can have a positive impact on the spectrum.

Sampling and truncation

To compute the spectrum through equation (1.10b), the integral needs to be rewritten as a sum over a set of discrete path length differences $x_j = j\Delta x$. Here, the sampling interval $\Delta x = x_{j-1} - x_j$ is the equidistant separation between two neighboring data points. The number of data points j depends on the region that is sampled by the interferogram. The index j can take values between $-N$ and $N-1$. The discrete Fourier spectrum can be written as a sum by replacing the infinite

integral by a finite sum: $\int_{-\infty}^{\infty} dx \rightarrow \Delta x \sum_{-N}^{N-1}$. It reads

$$S_L^{\Delta x}(\tilde{\nu}) = \Delta x \sum_{j=-N}^{N-1} \mathcal{I}(x_j) e^{-i2\pi\tilde{\nu}j\Delta x}, \tag{1.12}$$

with $L = N\Delta x$ the range $[-L, L]$ over which the interferogram is measured.

The parameters Δx and L of the interferogram are now compared to the corresponding ones for the spectrum, which are the sampling rate $\tilde{\nu}_s$ and the sampling interval $\Delta\tilde{\nu}$, as follows:

$$\tilde{\nu}_s = \frac{1}{\Delta x} = \frac{N}{L}, \tag{1.13a}$$

$$\Delta\tilde{\nu} = \frac{\tilde{\nu}_s}{2N} = \frac{1}{2L}. \tag{1.13b}$$

Equation (1.13a) shows that the smaller the separation between measurement points Δx in an interferogram, the larger the spectral range after Fourier transformation. Similarly, equation (1.13b) shows how a larger sampling region $[-L, L]$ decreases the sampling interval of the spectrum $\Delta\tilde{\nu}$. The smallest Δx at which the wavenumber $\tilde{\nu}_{max}$ still forms part of the spectral region is called the Nyquist frequency[106]. It is defined as the frequency that is equal to half of the sampling rate

$$\Delta x_{Nyquist} = \frac{1}{2\tilde{\nu}_{max}}. \tag{1.14}$$

In conclusion, it is important to measure an interferogram with a sufficiently large Δx in order to include the spectral region of interest and over a certain range to resolve its features.

Signal processing

In Fourier transform spectroscopy, there are two types of resolutions. The first one is the sampling resolution. The larger the sampling region of the interferogram, the finer the separation between $\tilde{\nu}$ in the spectrum. The second one is the spectral resolution, which expresses the ability to distinguish two closely spaced $\tilde{\nu}$. It is related to the sampling region. The larger the sampling region, the more frequencies are added to the analysis.

The sample resolution can be improved by a technique called zero-padding where the sampling region is artificially extended by adding zeros to the ends of the interferogram. It interpolates the spectrum to contain more data points. However, since the zeros do not contain any spectral information, this does not affect the spectral resolution. The only way to increase the spectral resolution is by performing an actual measurement over longer path length delays.

The interferogram of a non-monochromatic beam will have a large signal at zero path length difference $x = 0$. For larger values of x, the different $\tilde{\nu}$ will be increasingly out of phase such that $\mathcal{I}(x \rightarrow \pm\infty) = 0$. This could already be seen in the sketches of figure 1.5b. A measurement contains noise, which will dominate the signal at the tails. A window function can be used to progressively suppress the noisy tails of an interferogram. It is a symmetric function with a maximum in its center and with value 0 outside a certain range[107]. Multiplying a window function to the data improves the signal-to-noise ratio of the measurement and ensures a smooth transition in case that zero-padding is used.

Both zero-padding and windowing are important tools for the improvement of the spectrum in Fourier transform spectroscopy. This is especially true at the single molecule level, where the signal-to-noise ratio is generally low due to the weak fluorescence signal emitted by the molecules. The effectiveness of zero padding and windowing will be demonstrated in the next chapter.

1.5   Conclusions

This chapter gave an overview of the concepts and methods used for single molecule detection in chapters 2 to 4. In chapter 2, the Fourier transform fluorescence excitation spectroscopy technique will be tested in proof-of-principle studies on a synthetic rylene dye. They are complemented by fluorescence spectra. The single molecule features such as blinking, photobleaching and especially spectral wandering and jumping will be revisited. In chapter 3 the Fourier transform method will be successfully applied to unravel the spectral variability in weakly fluorescing photosynthetic antenna complexes, demonstrating its suitability to obtain excitation spectra from systems with a poor signal-to-noise ratio. In chapter 4, the focus will be shifted towards pump-probe experiments. A setup has been developed to measure stimulated emission which reached the sensitivity level of $\sim 10^{-7}$ necessary to measure against large background levels. In the last chapter of this thesis, chapter 5, plasmonic nanoantennas placed into the pump-probe setup described in chapter 4 will be used to measure the photothermal effects. The use of the confocal microscope is universal throughout the entire thesis.

2 | Single molecule excitation and emission spectroscopy

In this chapter, Fourier transform excitation spectroscopy is introduced as a sensitive and robust technique to probe the excited state manifold of single molecules. Its performance will be compared to that of the already well-established emission spectroscopy, which probes the ground state manifold. Synthetic quatterylene diimide (QDI) dye molecules are used in these in proof-of-principle studies due to their excellent photostability and brightness. It was found that these molecules exhibit extensive spectral shifts of more than 100 nm. These results do not only demonstrate the robustness of the technique, and the potential of single molecule spectroscopy to lift ensemble averages, but they are also used to discuss the biases that can be introduced when choosing a too narrow excitation and detection window.

This chapter is based on:

- L. Piatkowski, E. Gellings, and N. F. van Hulst. "Multicolour single molecule emission and excitation spectroscopy reveals extensive spectral shifts". *Faraday Discuss.* 184 (2015), pp. 207–220.

- L. Piatkowski, E. Gellings, and N. F. van Hulst. "Broadband single-molecule excitation spectroscopy". *Nat. Commun.* 7 (2016), p. 10411.
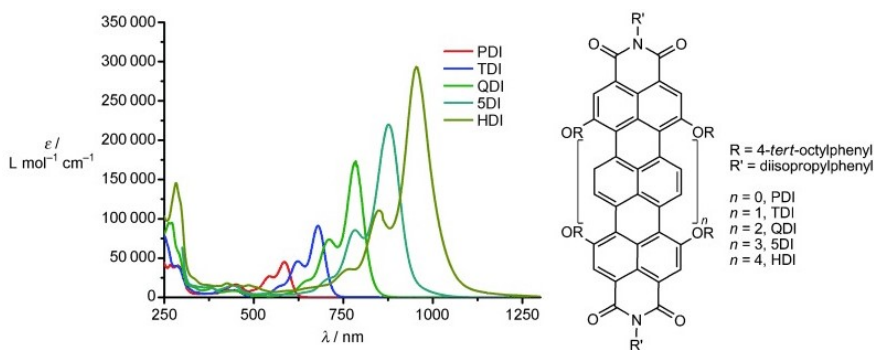
Figure 2.1: *The rylene diimide series.* Absorption spectra of the rylene diimide series, where the molecule had an additional naphthalene unit for each red-shifted spectrum as depicted on the right hand side. (Adapted from [108]).

After introducing quatterylene diimide, the molecule used in this chapter, the fluorescence emission spectroscopy setup will be presented. When looking at the emission spectra, single molecule features like blinking, photobleaching, spectral wandering, and jumping are revisited. Next, the experimental methods of Fourier transform excitation spectroscopy are introduced. Due to the novelty of interferometric methods at the single molecule level, details of the signal processing are given and the robustness of the technique against spectral instabilities demonstrated. Both excitation and emission spectra showed large spectral shifts of more than 100 nm. Based on these shifts, the bias of single molecule techniques towards experimental parameters such as the excitation wavelength will be discussed.

2.1   Quatterylene diimide (QDI)

Rylene dyes are good candidates for proof-of-principle single molecule studies due to their extraordinary photostability and high fluorescence quantum yield[109]. The synthetic quatterylene diimide (QDI) molecules used in this chapter belong to a series of core extended rylene dyes. This is sketched on the right side of figure 2.1, where perylene diimide (PDI) is enlarged along its long axis by adding more naphthalene units to the two it already has[94, 108]. For each additional naphthalene unit, which consists of ten carbon atoms organized in two rings, the absorption spectrum of the dye shifts by about 100 nm due to a larger delocalization of the electrons along the core. This can be seen in the absorption spectra, given on the left side of figure 2.1. QDI contains two additional naphthalene units, so four in total. This particular rylene dye was chosen, because the two main ensemble absorption peaks overlap best with the spectrum of the available broadband laser source.
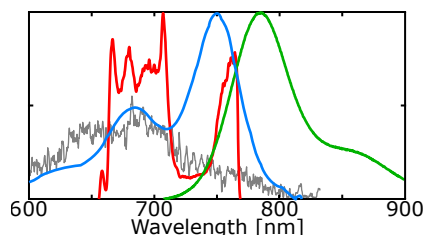
Figure 2.2: *Quatterylene Diimide (QDI).* The ensemble absorption (blue) and emission (green) spectrum of QDI measured in solution, and the solidified ensemble absorption spectrum embedded in PMMA (gray), as well as the excitation laser (red).

The QDI molecules were obtained from the Müllen group (Max Planck Institute for Polymer Research, Mainz, Germany). The samples were prepared by spin-coating a solution of QDI molecules at a ~1 nM concentration in Poly(methyl methacrylate) (PMMA)/toluene mixture (~1 %w/v). 50 µl of the solution was spin-coated onto a #1 microscope cover slip for 60 s at a spinning rate of 2000 rpm. Before sample deposition, the microscope cover slips had been cleaned by leaving them in a piranha solution (1:2 ratio hydrogen peroxide to sulfuric acid) for about ~30 min, then rinsing them with deionized water and blow-drying them with nitrogen. This procedure yielded no or very little contamination on the cover slips.

Figure 2.2 shows the ensemble solution absorption spectrum (blue, measured with NanoDrop 2000, Thermo Scientific) and emission spectrum (green, measured in the setup with a highly concentrated sample) together with the laser spectrum (red, measured with USB2000+, Ocean Optics). The absorption spectrum consists of the 0-0 transition at ~750 nm and two vibronic sidebands at ~680 nm and ~630 nm. The solution fluorescence emission spectrum is a rough mirror image of the solution absorption spectrum. However, only the main transition at ~785 nm and the first vibronic sideband at ~860 nm are visible. When depositing QDI solution onto a coverslip and measuring the absorption spectrum inside the setup with a halogen lamp, it coincides with the sketched one for the first few minutes. Once the solvent is evaporated and the PMMA solidifies, the surrounding PMMA affects the molecules, which leads to a large spread of the spectral position, and the spectral features are lost in the average (gray).

2.2 Single molecule emission spectroscopy

Emission spectroscopy of single molecules is a well-established technique at both cryogenic and room temperatures[16, 87]. While other single rylene dyes have already been studied spectroscopically, this is the first study on individual QDI molecules. It is a relatively straightforward experiment, which gives great insight into the spectral shifts and dynamics that one can expect from these molecules.
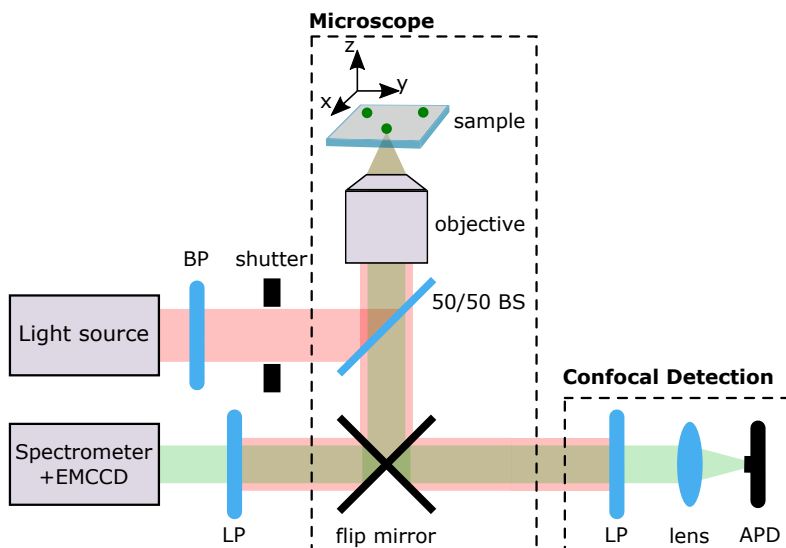
Figure 2.3: *Emission spectroscopy setup.* The laser light (red) is cleaned by a band-pass filter (BP), and focused onto the sample with a 50/50 beamsplitter (BS) and an objective. The sample is placed on a xyz stage. The molecule's fluorescence emission (green) is collected through the same objective and sent to either a spectrometer or focused onto an APD via a flip mirror. In both cases, a long-pass filter (LP) blocks reflected laser light. A shutter blocks the light in between measurements.

Methods

Figure 2.3 shows the setup used for emission spectroscopy. The light source was either a 632.8 nm helium-neon laser (HeNe, Melles Griot) or the ~670 nm range of a broadband titanium-sapphire laser (Ti:Sapphire, Octavius-85M, Thorlabs). Both beams were guided through a telescope including a 25 µm pinhole to collimate the beam, clean its profile, and expanded it to a diameter that overfills the objective. The HeNe (Ti:Sapphire) beam is cleaned spectrally with a narrow band-pass filter centered at 633 nm (680 nm) (FL632.8-10, Thorlabs resp. FF01-680/13-25, Semrock) in front of the microscope. A neutral density filter wheel can adjust the intensity of the beam entering the microscope. A mechanical shutter prevents sample illumination in between measurements.

Inside the microscope (Observer D1, Zeiss), the beam was reflected off a 50/50 beam splitter and focused onto the sample through a high *NA* oil immersion objective (1.3*NA*, 100x, Zeiss Fluar). The sample was moved through the laser focus via a piezo-controlled stage (Nano-LPS300, Mad City Labs). The fluorescence emitted by the sample was collected through the same objective and then either focused onto an APD (Perkin-Elmer) for confocal intensity detection or sent to a spectrometer equipped with and electron-multiplying charge-coupled device (EMCCD, Newton, Andor) for spectral measurements. A filter was placed into both detection paths to block any reflected laser light. For HeNe (Ti:Sapphire) excitation, a 635 nm
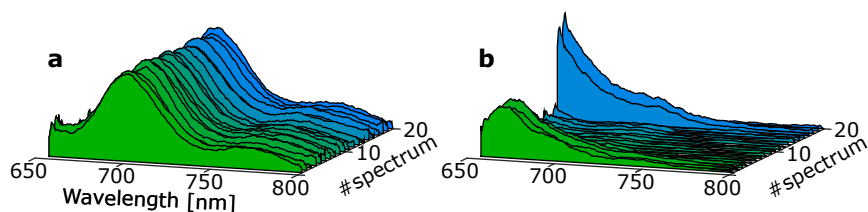
Figure 2.4: *Emission spectra.* 20 consecutive measurements of emission spectra of **(a)** a stable molecule and **(b)** a molecule exhibiting spectral jumps and blinking. The spectra have been smoothed to improve the visibility of the individual traces.

(740 nm) long-pass filter (FF01-635/LP, Semrock resp. 740AELP, Omega Optical) was placed in the APD detection path and a 633 nm notch (tilted 690 nm long-pass) filter (NF01-633U-25, Semrock resp. 690ALP, Omega Optical) was used in front of the spectrometer. For the spectrometer, the filters were chosen as close to the excitation wavelength as possible to detect the largest possible spectral range. For the APD this was not as crucial, since it was only used to localize the molecules.

In all experiments presented in this thesis, the position of the piezoelectric stage was controlled in a closed-loop fashion via an ADwin system (ADwin Gold II, Jäger GmbH), which was also used to record the fluorescence counts on the APD. Each experiment started with the recording of a confocal image for which the sample was raster-scanned over the laser focus in the xy-plane while measuring fluorescence intensity at each pixel. An example confocal image had already been shown in figure 1.4b in the previous chapter. For a well-aligned setup, these spots had a diffraction-limited size. Once a single molecule had been aligned into the microscope focus, 20 emission spectra were recorded sequentially in a kinetic series with an integration time of 1 s/spectrum at a camera gain of 200. Consequentially, the recorded spectra not exhibiting any blinking or photobleaching were averaged to increase the signal-to-noise ratio. The background level of the measurement was determined by performing the same measurement at another position where there were not any molecules. It was averaged and then subtracted from the recorded emission spectra.

Blinking, bleaching, and spectral diffusion

Two background-corrected sequences of emission spectra are shown in figure 2.4. The data has been smoothed to improve the visibility on the individual spectra. It can be immediately seen that the consecutive scans in figure 2.4a all resemble each other. The individual spectra were fitted with a Gaussian function, and the average main peak position was on average at 698.6 nm with a standard deviation of 1.4 nm. The full width at half maximum (FWHM) of the spectra was 39.3 nm with a standard deviation of 1.6 nm. These small differences in spectral positions and width over time were attributed to spectral wandering. Averaging the 20 scans

is equivalent to measuring the spectrum over 20 s. It results a peak position at 698.6 nm and a FWHM of 39.4 nm, which is slightly broader than the individual spectra. Comparable variations were obtained for other stable molecules.

Occasionally, a molecule blinks during a measurement. This manifests itself as a dark period without any emission. Figure 2.4b shows this, where an emission spectrum was recorded during scans 1-4, before the molecules was in a dark state. During scans 17-18 it started blinking again, though with a different spectrum, before photobleaching. In some cases, the emission spectrum before and after the blinking event were the same, but in other cases their shape and position differed. These abrupt changes in spectral position or shape is known as spectral jumping. Blinking with and without spectral jumping had been noticed in 19 out of the 120 measured molecules. When the blinking period is shorter than the integration time of 1 s the temporal resolution is not large enough to detect it as a dark period. However, a temporary lowering in the emission intensity would give an indirect means to identify the blinking. No spectral jumps without blinking have been observed in any of the emission spectra.

Statistical analysis

For a more in depth quantitative analysis, the recorded spectral sequences were averaged and then fitted with a Gaussian function to determine the position of the main emission peak. Whenever the main emission peak was so blue-shifted that it was blocked by the laser cut-off filter, like the spectrum in figure 2.4b after the blinking event, the measurement was discarded from the fitting. Since the filter's cut-off wavelength (654 nm) was situated relatively close to the laser excitation wavelength (632.8 nm), it was assumed that the filter blocked no more than part of the main emission peak at any time. Consequentially, the leftmost peak (or rise) was always assigned to the main emission peak.

In total, 19 emission spectra with the Ti:Sapphire excitation at ∼670 nm and 69 emission spectra with HeNe excitation at 632.8 nm were successfully fitted. Three normalized exemplary spectra are shown in figure 2.5a. They all approximately resemble a spectrally shifted ensemble emission spectrum, which was added to the figure in gray for comparison. This graph already gives a good idea of the large extent of the spectral shifts.

The distribution of main emission peak positions for the two excitation wavelengths is shown in figure 2.5b, divided into excitation by HeNe (blue) and Ti:Sapphire (red). The position of the maxima of the emission spectra ranged from the cut-off wavelength of the long-pass filter to about 760 nm, but did not quite reach the position of the ensemble spectrum at 785 nm (gray arrow). The distribution clearly peaks towards shorter wavelengths, close to where the excitation wavelength was. This is understandable, as these were the molecules that had their maximum absorption
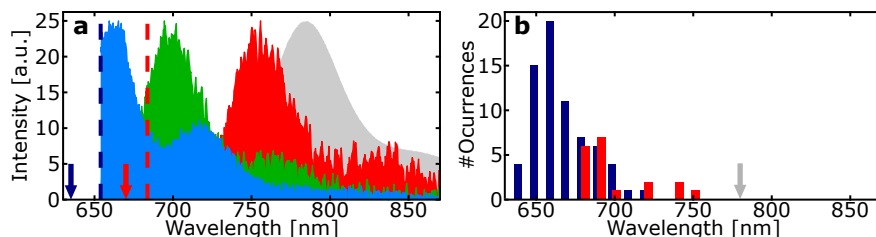
Figure 2.5: *Heterogeneity of single molecule emission.* **(a)** Exemplary emission spectra associated with molecules absorbing at different wavelengths together with the ensemble emission spectrum (gray). The blue and red arrow (dashed line) mark the excitation (cut-off) wavelength 633 nm (654 nm) resp. ~670 nm (690 nm). **(b)** Histogram representing the peak positions of the emission spectra excited at 633 nm (blue) and ~670 nm (red). The gray arrow represents the peak position of the solution spectrum.

overlap most efficiently with the excitation laser and thus appeared brighter on the image. In single molecule spectroscopy there is a bias towards picking only brighter molecules as the weaker ones disappear into the background noise. Therefore, the choice of excitation wavelength and detection bandwidth determines which molecular sub-ensemble is probed most efficiently, especially when dealing with a large spectral distribution like in this case. This is due to the poor overlap between the excitation wavelength with the absorption spectrum, which is already reflected in the most red-shifted spectrum of figure 2.5a (red) being noisier than the other two.

So far, it has been shown that QDI has a large spectral variety with significant shifts to lower wavelengths. As a result, a different subsection of the molecular ensemble is probed depending on the excitation wavelength. Due to the link between the absorption and emission spectrum, a similar spread in spectral positions is expected when measuring fluorescence excitation spectra in the next section.

2.3 Fourier tranform excitation spectroscopy

As opposed to emission spectroscopy, excitation spectroscopy of single molecules at room temperature has first been performed by scanning a narrowband laser over the absorption spectrum only in 2014, while it is a standard technique at cryogenic temperatures[32, 42, 43]. An important advantage of interferometric over scanned narrowband excitation spectroscopy is the robustness of the technique against blinking and bleaching. Provided that the main part of the interferogram around zero time delay is largely intact, the full spectral information is still contained in the measured (though incomplete) interferogram, with no significant effect on the quality of the measured excitation spectrum. The insensitivity of the interferometric approach to fluorescence intensity fluctuations and spectral jumps had already been demonstrated for interferometric detection of the emission spectra of individual molecules at cryogenic temperatures[110].
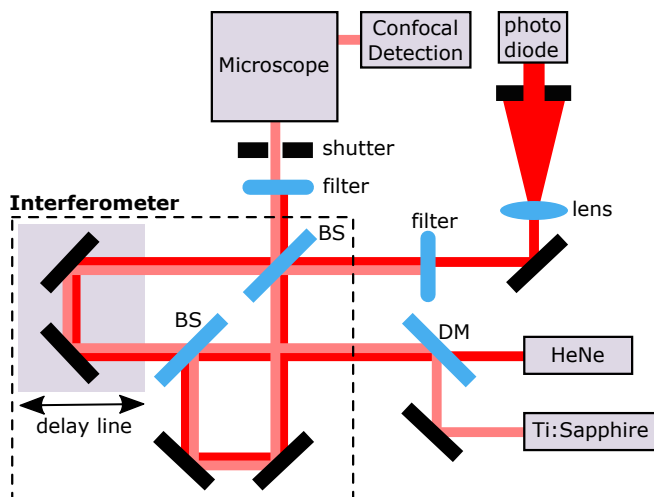
Figure 2.6: *Excitation spectroscopy setup.* A broadband Ti:Sapphire laser (light red) is sent to the microscope via an interferometer using two 50/50 beamsplitters (BS) and a delay line. The reference HeNe laser (red) is coaligned through the setup using a dichroic mirror (DM) and expanded onto a photodiode.

Methods

An interferometer and a reference beam were added to the emission spectroscopy setup as sketched in figure 2.6. The Ti:Sapphire laser first passed through a 4-f pulse shaper[111] (not sketched), which was only used to select the 650-770 nm wavelength range by physically blocking the spectral components above 770 nm in the dispersed beam. 650 nm was already the lowest available wavelength of the laser. This particular wavelength range overlaps well with the QDI ensemble spectrum as seen in figure 2.2.

A Mach-Zehnder type interferometer was used, where two equal 50/50 beamsplitters were used to separate and recombine the two beams[112, 113]. The optical path length difference was controlled by a mechanical delay line (NRT 100/M, Thorlabs), which was placed in one of the two arms. The HeNe was coaligned through the interferometer using a 650 nm short-pass dichroic mirror and served as a reference beam.

One output arm of the interferometer recorded the laser autocorrelation of the HeNe laser. Since the two lasers were spectrally separated, the Ti:Sapphire light could easily be removed from this arm by a 617 nm and 632 nm band-pass filter(FF01-617-73-25 and FF01-632/22-25, Semrock). To increase the resolution of the HeNe interferogram, a lens and an iris were placed in front of the photodiode (PDA36A, Thorlabs) to diverge and partially block the beam such that the width of interference fringes had approximately the same dimensions as the iris. The derived reference interferogram was used to precisely determine the optical path length difference

between the interfering Ti:Sapphire pulse-pair. This will be explained in detail in the next section.

At the other output arm, the recombined Ti:Sapphire beam was propagated colline-arly into the confocal microscope. At the short wavelength side, a 635 nm long-pass filter (FF01-635/LP-25, Semrock) separated the Ti:Sapphire beam from the HeNe, while on the long-wavelength side, a tilted 842 nm short-pass filter (FF01-842/SP, Semrock) blocked any stray light above the maximum laser frequency of 770 nm.

For Fourier transform excitation spectroscopy, the total fluorescence intensity was measured using the APD. A 780 nm and 785 nm long-pass filter (ET780LP, Chroma and LP02-785RU-25, Semrock) were placed in front of the APD to separate the fluorescence from the laser light. Once a molecule had been positioned into the laser focus, interferograms were recorded by scanning the delay line until the molecule photobleached. This procedure was repeated for all molecules in the confocal image. The laser spectrum was measured by exchanging the long-pass filters in the detection path for a diffuser. A diffuser was chosen instead of a neutral density filter because their optical density varies over the wavelength range, distorting the spectrum.

The Ti:Sapphire power was set to ~1 µW for a single beam at the sample position. For an average molecule, 2000-3000 counts s^{-1} were detected out of which about 200-300 counts s^{-1} remained when measuring on a sample spot without any mo-lecules, i.e. the background. The APD had ~10 counts s^{-1} dark counts, so that the background noise was mainly ascribed to stray ambient light above the cut-off wavelength of the long-pass filters.

The delay line was scanned over 60 µm, which is equivalent to an interpulse delay ranging from -200 to 200 fs. The delay line velocity was set to 0.5 µm s^{-1} which re-sulted in a measurement time of 2 min/scan. The acquisition time was set to 10 ms per data point. The data acquisition in LabView was set up in such a way that after each 10 ms data point measurement, there was a ~20 ms interval of processing without any further data acquisition. This had been fixed for the measurements on light harvesting complexes in the following chapter, where a different delay stage had been used. Even with this less than ideal data acquisition, 12-13 mea-surement points were recorded per oscillation period of the broadband laser. This corresponds to a measurement point for every ~0.2 fs interpulse delay. According to equation (1.14), at 770 nm a point should be measured at least every 1.3 fs to meet the Nyquist criterion.

To obtain the spectra, the interferograms of the laser and fluorescence response of a molecule upon excitation were Fourier transformed by a fast Fourier transform (FFT) algorithm in matlab (`fft(X)`). The total fluorescence spectrum was then di-vided by the laser spectrum to obtain the excitation spectrum. Having data points at
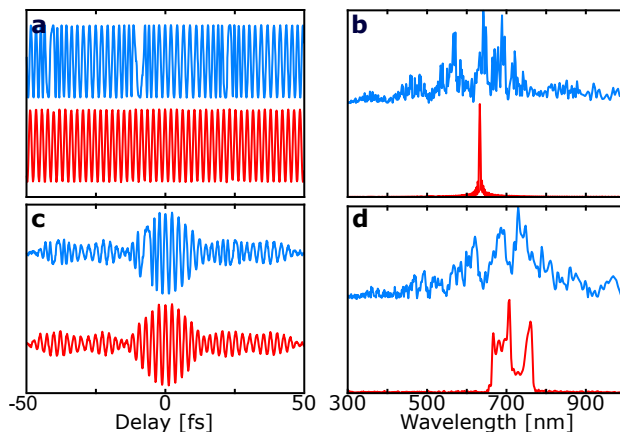
Figure 2.7: *Reference signal.* Zoomed-in interferograms of the measured (blue) and corrected (red) laser autocorrelations of **(a)** the HeNe and **(c)** the Ti:Sapphire laser. In **(b)** and **(d)** the corresponding Fourier transformations are plotted.

equidistant time intervals was crucial for the correct working of the FFT algorithm which was ensured by the reference signal.

Intermezzo: The reference signal

For the Fourier transform approach to work, the time axis needs to be known to high precision, and divided into equidistant time intervals. The monochromatic HeNe reference beam was introduced into the setup exactly for that purpose. It generated a sinusoidal interference pattern from which the actual time difference between data points could be determined under the condition that the setup has adequate amplitude and phase stability. Since both laser beams propagated through the same interferometer, it is automatically valid for the fluorescence interferogram measured at the APD as well.

The time delays can be extracted from the normalized sinusoidal interference pattern $\mathcal{I}_{ref}(t)$ with the help of equation (1.7), using $x = ct$ and $\tilde{\nu} = 1/\lambda$:

$$\mathcal{I}_{ref}(t) = \cos(2\pi ct/\lambda) \iff t = \frac{\arccos\left(\mathcal{I}_{ref}(t)\right)}{2\pi c/\lambda}. \tag{2.1}$$

Figure 2.7 shows an example for the simultaneous measurement of the HeNe and Ti:Sapphire autocorrelation and their respective Fourier transformations. The blue graphs represent the measured data, where the time axis was based on the assumption of a constant delay line speed of $0.5\,\mu m\,s^{-1}$. The uncorrected HeNe interferogram in figure 2.7a exhibits a broadening and narrowing of the interference fringes. This effect is mirrored in the Ti:Sapphire autocorrelation in figure 2.7c. It was attributed to the periodic slowing down and speeding up of the mechanical delay line during each motor revolution.
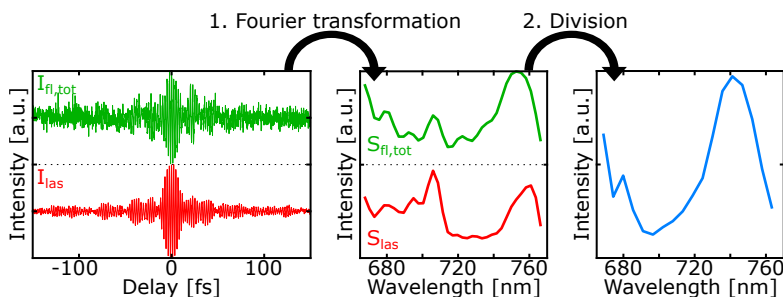
Figure 2.8: *Obtaining an excitation spectrum.* The interferograms of the total fluorescence (green) and laser (red) spectra are Fourier transformed. The two resulting spectra are then divided to obtain the fluorescence excitation spectrum (blue).

Using equation (2.1), the actual time delay t was calculated for each data point and both laser and fluorescence interferogram were interpolated to a time vector with equidistant time intervals as required by the FFT algorithm. Since only the relative time delay could be calculated, zero time delay was manually assigned to the central peak for each interferogram. The success of this method can already be seen in the corrected interferograms in figure 2.7a and c (red), which now show smooth oscillations. It becomes even more apparent when looking at the Fourier transformations of the interferograms before and after the correct assignment of t. In figure 2.7b and d, the HeNe and Ti:Sapphire spectrum was unrecognizable prior to the corrections (blue), whereas it clearly resembled that measured with a conventional spectrometer after the corrections (red, see figure 2.2). Often, interferograms were measured repeatedly on the same molecule in order to average them. In those cases, the same data range, i.e. the same HeNe oscillations, were selected for each scan and the data interpolated with a common time vector to facilitate averaging.

Data processing

Several steps are necessary to turn an interferogram into an excitation spectrum. The formulas and concepts established in section 1.4 in the previous chapter were applied here step by step. Figure 2.8 shows the interferogram of the convoluted total fluorescence signal $\mathcal{I}_{fl,tot}$ (green) and the laser autocorrelation $\mathcal{I}_{las}$ (red). They were both Fourier transformed and converted from frequency to the wavelength scale. The laser spectrum $\mathcal{S}_{las}$ was interpolated to have the same time-axis as the total fluorescence signal $\mathcal{S}_{fl,tot}$. Dividing $\mathcal{S}_{fl,tot}$ by $\mathcal{S}_{las}$ finally yielded the excitation spectrum (blue). All spectra were truncated to the spectral range of the laser spectrum.

As explained in section 1.4.3, the application of averaging and windowing can improve the quality of the spectrum, while zero-padding increases the sampling resolution. Figure 2.9 demonstrates the effect of these techniques on the obtained excitation spectrum. In figure 2.9a, a single fluorescence interferogram was taken
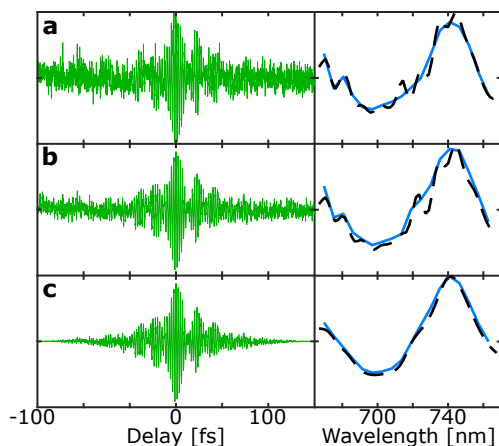
Figure 2.9: *Data processing.* The fluorescence interferograms (left) and excitation spectra (right, dashed lines: zero-padding) of the molecule from figure 2.8, using **(a)** one scan, **(b)** the average of three scans, and **(c)** a Hann window.

from the same molecule as figure 2.8 to obtain the excitation spectrum (blue). The dashed black line was achieved when increasing the number of data points of the interferogram threefold through zero-padding. It is not noisier, but simply resolves the noise better. In figure 2.9b, three fluorescence interferograms were averaged. The noise level of the interferogram has noticeably decreased. However, the resulting spectrum remains relatively noisy. In figure 2.9c a Hann-window[107] was applied to both laser and averaged fluorescence interferogram to suppress noise far from zero time delay. The interferogram approached zero at the edges, suppressing much of the leftover noise. In the excitation spectrum, the kinks disappeared from the data, and a smooth spectrum was obtained. The interferograms of all measured molecules were processed using the above presented steps.

Robustness

One of the advantages of Fourier transform spectroscopy over narrowband scanning is the robustness of the technique against blinking and bleaching. This is demonstrated in figure 2.10, where blinking and bleaching events and changes in the scanning parameters were artificially added to the interferogram, and their effect on the excitation spectrum analyzed. The processed excitation spectrum from figure 2.9c has been added to the spectra for comparison (dashed lines).

Figure 2.10a shows the original scan. When halving the measuring range to $\pm 75\,\text{fs}$ in figure 2.10b, the resulting spectrum has less spectral resolution as expected, but still gives the correct signal. This means that if spectral resolution is not needed, measurement time could be reduced by half. However, when instead cutting the interferogram shortly after the maximum interference in figure 2.10c, which corre-
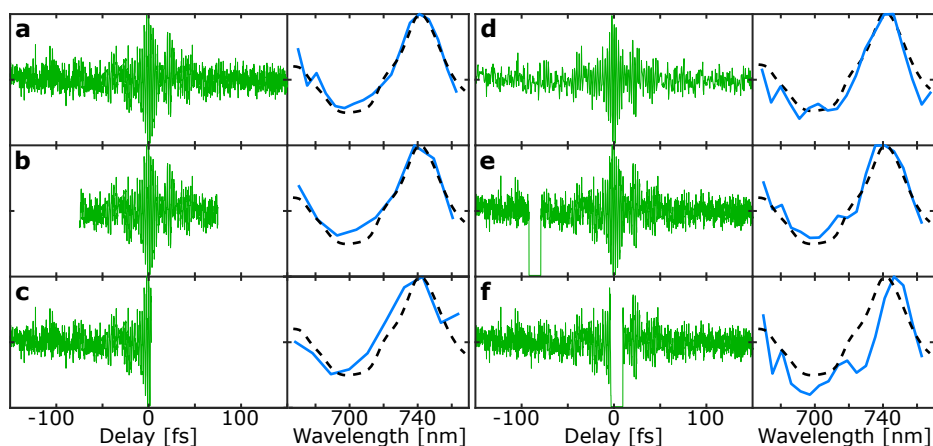
Figure 2.10: *Robustness of Fourier transform measurements.* Modified fluorescence interferograms (left), and the resulting excitation spectra (blue, solid), compared to the processed spectrum from figure 2.9c (black, dashed). **(a)** Original trace, **(b)** truncation to half the time window. **(c)** bleaching after peak, **(d)** data acquisition with 25 % of data points, **(e)** blinking far from center, and **(f)** blinking at center.

sponds to a photobleaching event, the spectrum shifts towards lower wavelengths, therefore yielding an incorrect result. When the interferogram is measured with only 25 % of the data points in figure 2.10d, the Nyquist criterion of a data point every 1.3 fs is still met. Since the data range of the interferogram remained unchanged, the same spectral resolution as in the original spectrum was achieved, even though it is narrower and noisier. This means that if noise is not important, the measurement could be performed at least four times faster. Finally, the effect of blinking will be considered. A 12.5 fs blinking event far from the main features of the interferogram in figure 2.10e mainly increases the noise level. Only when the blinking happens around the main interferometric feature in figure 2.10f, is the spectrum seriously compromised.

Therefore, unless the main feature of the interferogram is compromised by blinking or photobleaching, the correct peak positions were obtained in the excitation spectrum in all cases. When averaging several interferograms, blinking and bleaching events were removed from the averaging. Since all wavelengths are probed simultaneously at all time delays, the averaging improves the entire spectrum equally regardless of the position of the blinking and bleaching, while it would lead to noisier spectra where blinking events occurred when averaging narrowband line scans of blinking molecules.

2.3.1 Measurements

The fluorescence excitation spectrum has been measured for a total of 25 molecules. On the left hand side of figure 2.11, five spectra of the total fluorescence signal
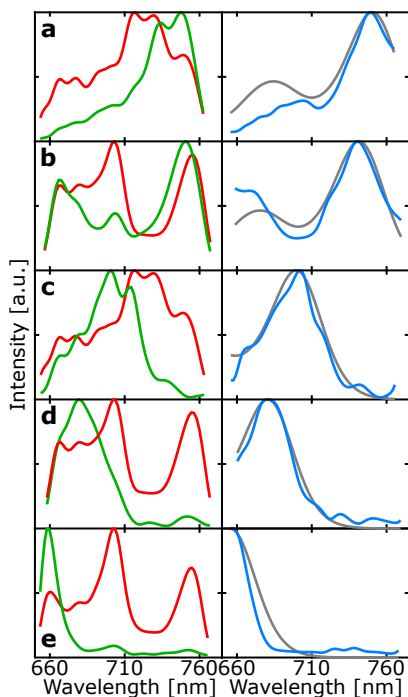
Figure 2.11: *QDI excitation spectra.* **(Left)** the laser spectrum (red) and product spectrum (green) of 5 different molecules. **(Right)** The corresponding excitation spectra (blue) together with a QDI ensemble spectrum which was spectrally shifted to match the single molecule peak.

are given (green) along with the laser spectrum with which the molecule had been excited (red). The excitation spectra obtained after dividing these two spectra are shown on the right hand side (blue) together with a spectrally shifted QDI ensemble spectrum (gray) to overlap with the measured spectrum. These particular graphs were chosen to illustrate the extent of the spectral shift of the single QDI excitation spectra. While the laser spectrum changed a bit every day, it was altered on purpose in figure 2.11a and c to demonstrate that the technique and the division by the laser spectrum works independently of the applied laser spectrum. Besides the spectral shift, it can be clearly seen that in all cases the single molecule spectrum has a narrower main peak than the ensemble spectrum. This is the result of the inhomogeneous broadening when superimposing many shifted spectra.

Figure 2.12 shows the spread of the main peak positions for the measured excitation spectra. The distribution has a double peak following the laser spectrum (shown in red). More spectra were measured whenever the main absorption peak overlapped with one of the more intense parts of the laser spectrum. Since the fluorescence is detected above 785 nm for all excitation spectra, less emission is collected for blue-shifted molecules, making them underrepresented. This once again underlines the importance of the right choice of excitation wavelength, detection range and
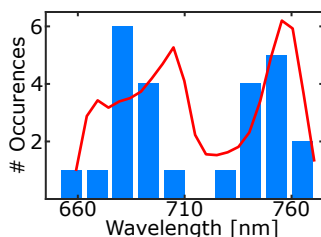
Figure 2.12: *QDI main peak position.* The main peak position of 25 molecules. In red, the laser spectrum.

especially intensity distribution of the laser spectrum in single molecule experiments. As figure 2.2 showed, the ensemble spectrum of figure 2.2 exhibits a Stokes shift of 35 nm. Yet, careful comparison of the measured single molecule excitation and emission spectra shows that the maximum measured excitation peak is around 765 nm, which is slightly above the ensemble value (750 nm), whereas the largest measured emission peak value is around 750 nm, far below the ensemble value (785 nm). On top of that, the main emission peak is blue-shifted with respect to the absorption peak. This originates from the choice of excitation wavelengths and not from molecules emitting light below the excitation wavelength. Emission spectra at higher wavelengths do exist, they were simply not excited efficiently by the chosen excitation wavelengths.

The existence of emission spectra at higher wavelengths was verified via the simultaneous measurement of excitation and emission spectra. For this, a 50/50 beamsplitter was placed into the detection path, where one arm was directed to the APD to record interferograms and the other arm to the spectrometer to record emission spectra. Figure 2.13 shows one of these measurements. The main absorption peak is at 735 nm, while the main emission peak is below the cut-off wavelength of the long-pass filter of 785 nm. The ensemble excitation and emission spectra were added to the graph and spectrally shifted by the same amount to overlap with the excitation spectrum. The overlap for the emission spectrum is reasonable as well so that it can be concluded that the ensemble Stokes shift is approximately maintained. This is in line with what has already been reported for other single rylene based dyes at room temperature[32, 42, 43].

It should be noted at this point that both the excitation and emission spectra kept their shape while shifting to lower wavelengths by more than 100 nm with respect to the solution spectrum. When exciting the sample with 800 nm, no molecules were detected on a confocal image, so that no significant spectral shifts to higher wavelengths took place. The blue-shift without shape changing is attributed to the interaction of the dyes with the PMMA matrix. The absorption spectrum of a dried up sample in figure 2.2 already was one indication of that. The rylene diimide series has more red-shifted spectra, the longer the core due to a larger electron
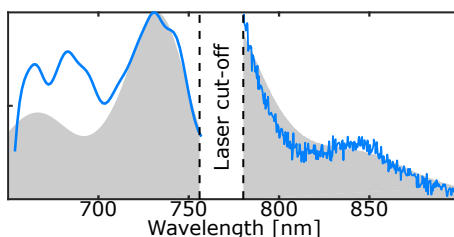
Figure 2.13: *QDI excitation-emission spectrum.* Simultaneous measurement of the excitation (left) and emission (right) spectrum of a single QDI molecule. The shifted ensemble spectra are added in gray.

delocalization without significant changes in the spectral shape. Therefore, the truncation of the core by the PMMA matrix, for example via twisting would be a plausible explanation, which has already been reported for single perylene diimide (PDI) molecules, a shorter rylene dye from the same series[31].

The presented approach enabled the detection of excitation spectra of single molecules at room temperature. Due to the novelty of the technique, further improvements are still conceivable. The experiment is constrained by the available spectral window of the Ti:Sapphire laser, which starts at ~650 nm. This implies that the excitation spectra at lower wavelengths was missing. However, since the spectra were not significantly red-shifted, the main absorption peak always fell within the detection window when setting the maximum wavelength of the laser to ~770 nm. Expanding the spectral window of the excitation laser would allow seeing a larger fraction of the excitation spectrum of a specific molecule, even though it does not necessarily enable the detection of more blue-shifted molecules. This is because, the larger the blue-shift of a molecule, the less the excitation spectrum will overlap with the spectral range set by the excitation laser until the blue-shift would be so large that the molecular emission is completely blocked by the laser cut-off filter. Choosing a distinct spectral window at lower wavelengths would be more suitable in that case, especially when studying molecules with a narrow range in excitation and emission spectra.

The excitation spectrum of an individual molecule had been acquired in a time that is comparable to that of its emission spectrum. A single interferogram was acquired for ~2 min, which yielded a decent excitation spectrum for the ~0.2 fs resolution in delay. Reducing the sampling frequency and data range (which decreases spectral resolution and the spectral range respectively), it would be possible to record an interferogram within ~20-30 s without significantly affecting the shape of the acquired excitation spectrum. Up to another factor of 3 in acquisition time could be gained, when circumventing the dead time in the data acquisition in LabView. The acquisition time to obtain a reasonable fluorescence emission spectrum with

the same excitation power was typically 1-20 s (with 200 cameragain), depending on the brightness of the molecule.

Both fluorescence excitation and emission experiments are based on the detection of fluorescence. In excitation spectroscopy, a broadband laser excites the entire absorption band, so that the lower wavelength edge of the fluorescence will always be cut by the laser cut-off filter. For emission spectra, the excitation wavelength and cut-off filter are ideally chosen such that the entire fluorescence emission spectrum can be resolved. Therefore, emission spectra typically collect more fluorescence counts in total. However, these fluorescence counts are divided into hundreds of pixels at the EMCCD camera, whereas they are all measured on just one pixel at the APD. In this case, considering perfect conditions, the APD has ∼10 counts/s dark counts, whereas the EMCCD camera has ∼0.005 counts/pixel/s based on their technical datasheets. Here the signal using 8000 pixel, which yields a comparable noise level of ∼40 counts/s. In practice, the choice between emission and excitation spectroscopy should be based on the availability of measurement equipment more than anything and it is beneficial to measure both on the same molecule since they probe different electronic energy levels.

The presented fluorescence excitation technique required a broadband laser source and a (Mach-Zehnder) interferometer. It did not need any other modifications with respect to existing single molecule fluorescence detection schemes and should thus be compatible with any confocal detection setup. The time that was necessary to measure a single molecule's excitation spectrum was comparable with the lifetime of many biologically relevant fluorescent molecules, even those with low photostability such as light harvesting complexes[41], making them a potential candidate for this technique. The feasibility of the technique to study these light harvesting complexes will be demonstrated in chapter 3.

The experimental approach presented here is similar to already existing Fourier transform methods, though with two important differences. First, commercially available Fourier transform spectrometers do not offer single molecule sensitivity and second, they do not provide active control over the excitation process. Not only the time delay, but also the phase and chirp of the pulse pair of the coherent broadband light could be manipulated. The pulses could also be compressed to their transform limit of ∼15 fs) to coherently probe single molecule femtosecond dynamics and their (de)coherence behavior. Additionally, using two interfering excitation beams, it might be possible to measure the excitation spectrum of non-fluorescent (single) molecules by detecting stimulated emission photons, a detection scheme which has already shown to reach nearly single molecule sensitivity[91]. This would give access to the information normally obtained through fluorescence, but from non-fluorescent molecules. Stimulated emission spectroscopy will be discussed in more detail in chapter 4.

2.4   Conclusion

Fourier transform spectroscopy has been successfully introduced to the repertoire of available single molecule methods in one of the first ever fluorescence excitation spectroscopy measurements at room temperature. It is more robust against blinking and photobleaching than spectral line-scans. Measuring excitation together with emission spectra allows to access the excited state manifold alongside the ground state manifold and thus to obtain more information about the molecule. It has also be shown that molecular spectra can significantly shift from the ensemble average, and that only subensembles depending on the chosen excitation wavelength can be probed at once.

3 | LH2 excitation and emission spectroscopy

Excitation and emission spectra probe different molecular energy levels, which together offer a more complete picture of the molecular structure. With the robust Fourier transform excitation spectroscopy method from the previous chapter, the variability of the excited state manifold of weakly fluorescing photosynthetic light harvesting complexes LH2 was probed for the first time. These complexes have already been studied extensively both theoretically and experimentally to understand their near-unity energy transfer efficiency despite large variability in their environment. So far, the absence of single complex excitation spectra at room temperature made it necessary to rely on assumptions about the spectral disorder of the excited state manifold for both data analysis and modeling. Here, this limitation is overcome and excitation and emission spectra measured side by side. It will be shown that the complexes show little spectral variability. The variations in the two absorption bands B800 and B850 are uncorrelated, while the Stokes shift between the B850 and emission band becomes larger for more red-shifted complexes. Additionally, it will be demonstrated that ensemble measurements are biased by the experimental parameters, where the measured ensemble Stokes shift was about 20 % smaller than the average single complex result, stressing the importance of single molecule studies even for systems that do not show a large variability.

This chapter is based on:

- E. Gellings, R. Cogdell, and N. F. van Hulst. *Room temperature excitation-emission spectra of single LH2 show remarkably little variation.* [manuscript written].
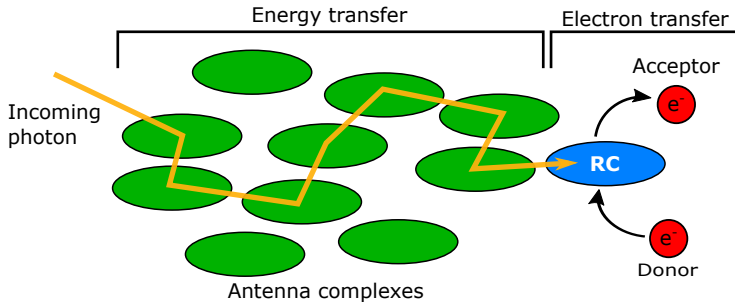
Figure 3.1: *Energy transfer during photosynthesis.* An incoming photon (orange) is captured by an antenna complex and its energy is consequentially transferred to the reaction center (RC), where it is stored long-term by an electron acceptor molecule.

Over billions of years, nature has developed and optimized the ultimate system to convert light energy into chemical energy: photosynthesis. As sketched in figure 3.1, photosynthesis begins with the capture of a photon by one of many light-harvesting antenna complexes. From this complex, the energy is transferred from complex to complex via resonant energy transfer until a reaction center is reached. At the reaction center, long-term energy storage is achieved by transferring an electron to an electron acceptor molecule.

Antenna complexes are able to handle several magnitudes of light intensity[114, 115], they adapt to spectral changes[114] and the photon energy transfer is very efficient, typically 80-95 % under ideal conditions[116]. Interestingly, this efficiency might be facilitated by persistent coherent responses which have been observed even under physiological conditions[90, 117–119].

Understanding the working principles of these complexes is fundamentally interesting, and also important for harnessing their potential, for example in solar cell design[120, 121]. The coherent processes of different photosynthetic systems to transfer their energy have already been studied extensively with 2D electronic spectroscopy (2DES), yet only on ensemble samples. They revealed intrinsic details on the internal coupling and energy transfer paths within the multi-chromophoric antenna complexes that manifested themselves as long-lasting oscillations in the 2DES spectra[119, 122, 123]. The antenna complexes exhibit spectral and dynamical disorder due to variations in the dipolar interactions between their chromophores that arise from both intrinsic differences and environment-induced changes. This typically makes the observed collective oscillatory response of the ensemble spectra too complicated to interpret in detail. A good way to overcome the spectral congestion would be to move to the single complex level, though at the cost of weak signals.

In this chapter, single light-harvesting complexes (LH2) of the purple bacteria *Rps. acidophila* will be examined. Due to its highly symmetric structure[124, 125], LH2

has already been studied extensively at both cryogenic[126–131] and ambient[115, 132, 133] temperatures. Despite LH2 containing several chromophores, it showed antibunching, proving that the LH2 complex behaves as a single photon emitter[134]. Recently, femtosecond pump-probe excitation was successfully applied to measure the excited state energy transfer dynamics of single LH2 complexes[90]. It revealed transient femtosecond traces that show coherent energy transfer pathways. The oscillations of the coherent state were well-defined and easy to extract compared to ensemble data because they exhibited just a single oscillatory component with periods ranging from 140-400 fs.

The electronic structure of the light-harvesting complex and its level of disorder are assumed to play an important role in the distribution of the oscillatory periods[135]. Due to the difficulty and novelty of excitation spectroscopy at room temperature, the excited state levels and their variability remain unknown for LH2 or any other light harvesting complex. Only indirect conclusions about its variability could be drawn from single complex emission spectra[127, 133, 136, 137], or from studies at cryogenic temperatures, where the spectrum differs significantly from its room temperature counterpart. Besides helping with the interpretation of the coherences, the level of disorder at the single complex level is also an important parameter for modeling[135, 136].

This shows that having room temperature single complex excitation and emission spectra available side by side would be a great asset to both experiments and modeling. In this chapter, the inhomogeneity of and the correlations between the excitation and emission bands were examined with a focus on the variation in spectral band positions and interband distances with a special interest in the Stokes shift. For the excitation spectra, moving from proof-of-principle studies on synthetic dyes[32, 42, 138] to biologically relevant systems like LH2, it has been necessary to develop more sophisticated ways to overcome challenges such as the low photon yield and spectral instability inherent to these systems.

3.1 Light-harvesting complex LH2 of *Rps. acidophila*

LH2 contains 27 bacteriochlorophyll (BChl a) pigments that are arranged into two concentric rings, called B800 and B850. As figure 3.2a shows, the B800 ring (blue) contains 9 well-separated pigments and the B850 ring (red) consists of 18 tightly packed pigments. Figure 3.2b shows the complete antenna complex, which also contains a carotenoid ring (orange), embedded in a protein scaffold (gray). The exact spectral position of the different bands depends strongly on the binding of the pigments to the protein scaffold and on the distance and mutual orientation between the individual pigments. The weakly coupled pigments ($\sim$24 cm^{-1}) of the B800 band act localized and absorb around 800 nm, while the strongly coupled pig-
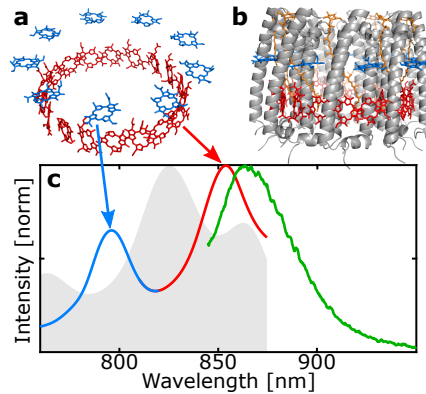
Figure 3.2: *LH2 structure and thin film spectrum.* **(a)** The 27 Bchl a pigments of the LH2 complex divided into the B800 (blue) and B850 ring (red). **(b)** The complete protein, including carotenoids (orange) and the protein scaffold (gray). **(c)** Thin film ensemble excitation (B800 in blue, B850 in red) and emission (green) spectrum, alongside the excitation laser (gray).

ments ($\sim$300 cm^{-1}) of the B850 ring form a delocalized excitonic state over several chromophores that absorbs light around 850 nm[139]. Energy is transfered from the B800 to the B850 band via electronic coupling[90], and fluorescence emission occurs from the B850 band with a quantum yield of $\sim$10 %[140]. The carotenoids absorb light around 500 nm[141], which is outside the spectral window of the current experiments. The two figures were adapted from Protein Data Bank ID 1KZU[142].

Already purified LH2 (strain 10050, see Gardiner et al. for details[29]) was diluted in an aqueous 1.8 % PVA solution. The solution included 10 mM sodium phosphate dibasic (Na$_2$HPO$_4$) to keep a constant pH of 8.1, and 0.03 % α-dodecyl maltoside as a detergent to make the proteins soluble in water and to prevent aggregation. For single molecule studies the dilution was 80 000 times and for thin film measurements 12 times. The solution was spin-coated onto a clean glass coverslip at 1500 rpm for 60 s.

Figure 3.2c shows the excitation and emission spectra of a thin film sample. This sample has been prepared and measured using the same procedures as the single complex studies. The absorption maxima are at around 796 nm for the B800 band and around 854 nm for the B850 band. Emission occurred around 865 nm. This ensemble spectrum will be compared to the single molecule spectra at a later stage.

3.2 Experimental parameters

The setup from chapter 2 was adapted to the parameters needed for LH2 (see figure 2.6). Specifically, the 750-880 nm wavelength range of the Ti:Sapphire laser was chosen, and the spectral output cleaned with a band-pass filter with a spectral width of 160 nm centered around 794 nm (FF01-794-160-25, Semrock). The result-
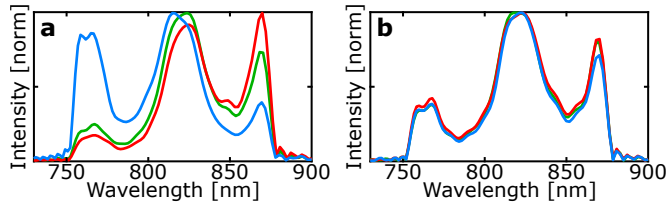
Figure 3.3: *Chromatic aberration.* Laser autocorrelation when reflecting off a coverslip with the position of maximum beam intensity before (red), at (green) or after (blue) the coverslip. For **(a)** 1.3*NA*, 100x, Zeiss Fluar and **(b)** 1.4*NA*, 60x, Nikon Plan Apo λ.

ing laser excitation spectrum is shown in figure 3.2c. The mechanical delay line was exchanged for an actuator (M-230.10, Physik Instrumente) that was mounted onto a manual linear stage (9063-COM-M, Newport). This substitution got rid of most of the scanning speed variations, making it easier to assign the correct time vector. In the microscope, the 50/50 beamsplitter was replaced by a 10/90 beamsplitter, reflecting 10 % of the laser power onto the sample and letting 90 % of the fluorescence through to the detector. This maximized the fluorescence collection at the cost of excitation power, the latter not being critical due to enough excitation power being available.

Chromatic aberrations occur when not all colors are focus in the same position. Microscope objectives are typically corrected for them within a certain wavelength range. The 1.3 *NA* objective used for QDI measurements in the 650-770 nm wavelength range showed large chromatic aberrations in the 750-880 nm wavelength range used for the LH2 measurements. This is shown in figure 3.3a. The autocorrelation of the reflection of the highly attenuated laser beam was measured on the APD at three positions: at maximum intensity (green) as well as moving the focus up (blue) and down (red) until the counts on the APD drop to half the maximum value. The graph shows that when focusing before the coverslip, the lower wavelength part of the beam is much stronger than the higher wavelength part, while when focusing after the coverslip, it is the opposite way around. Therefore, depending on the focus, the molecule would be excited with different laser spectra. That is why the experiments on LH2 were performed with a different objective whose chromatic aberrations were minimal for the wavelength range used (1.4*NA*, 60x, Nikon Plan Apo λ). When measuring the laser autocorrelation for this objective the same way as the other one, hardly any changes in the laser spectrum are perceived, as shown in figure 3.3b.

Photoinstabilities in the LH2 complexes mainly originate from oxygen in the environment[127] or they are photoinduced[115]. The former can be overcome by removing the oxygen from the sample by flushing the sample with nitrogen. That is why during all experiments, a small box was placed around the sample and the oxygen was removed from the sample by supplying a constant nitrogen flow into

the box throughout the experiment. The latter can be minimized by choosing a low excitation power.

Two different measurement schemes were applied:

1. The excitation spectrum of the B800 band was measured simultaneously with the emission band.
2. The full excitation spectrum was measured sequentially with the emission spectrum.

In both cases, to measure emission spectra, the excitation beam was blocked above 820 nm with a tilted 842 nm short-pass filter (FF01-842/SP, Semrock) that had been mounted on a flip mount in front of the microscope entrance. In the detection path, two 830 nm long-pass filters (BLP01-830R-25, Semrock) filtered out any scattered laser light. Emission spectra were recorded using a series of 1 s spectra at 250 gain and the background signal measured away from the molecules was removed.

In the first measurement scheme, excitation and emission spectra were measured simultaneously by splitting the fluorescence signal in the detection path with a 50/50 beamsplitter that had been placed after the long-pass filter. One arm was sent to the APD and the other to the spectrometer. In this scheme, the excitation laser bandwidth was limited to 750-820 nm so that the B850 band fell out of the spectral window. In the second measurement scheme, the excitation spectra were measured using the full laser bandwidth of 750-880 nm. Detection took place at a separate microscope detection port similar to the QDI measurements. Two 885 nm long-pass filters (HG885LP, Chroma) cleaned up the scattered laser light in front of the APD.

In both schemes, excitation spectra were measured while scanning the time delay continuously over 400 fs (600 μm) with a scanning speed of 0.5-1 nm/s. An interferogram was measured with 10-20 ms time bins, resulting in a collection time of 1 min/scan. The data acquisition with LabView had received an overhaul after the incorporation of the actuator. Compared to the previous chapter it is now possible to record data continuously without any dead time.

All measurements were performed at relatively low excitation powers of around 0.5 μW (100 W/cm^2 in focus) to minimize photoactivated spectral instabilities which increase linearly with the excitation power[132], and to avoid saturating the system which occurs at excitation intensities of more than 100 W/cm^2[97]. Under these low-light conditions, most complexes were photostable during the duration of the experiment of 10 min or more, and hardly any spectral or intensity jumps were observed. Going to higher powers would reduce the photostability noticeably without resulting in a significant increase in signal due to the saturation of the system. At the chosen low excitation powers hardly any spectral jumps took place so that switching between excitation and emission spectra could be done without needing
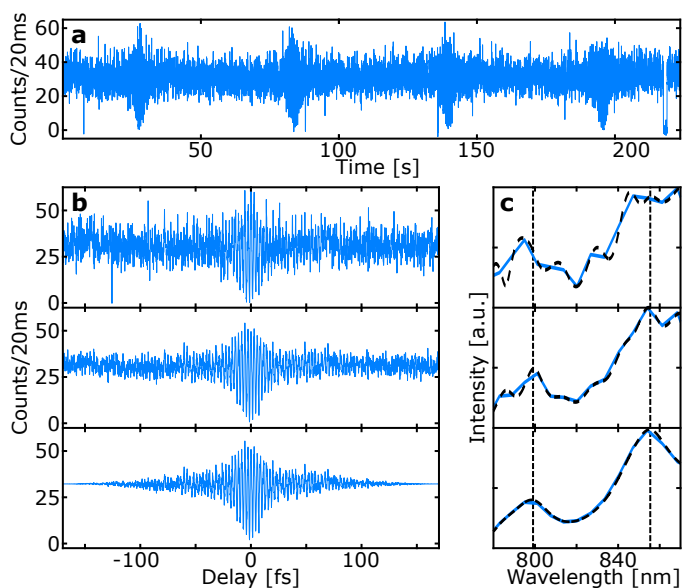
Figure 3.4: *Data processing.* **(a)** Four consecutive fluorescence interferograms of the same single LH2 complex. **(b)** From top to bottom: the first scan, the 4 scans averaged and excluding blinking events, and windowing added. **(c)** The corresponding excitation spectra. The dashed black spectra have zero-padding added to increase the sampling frequency. The vertical dotted lines are added at the peak positions.

to worry about spectral changes during the switching. Nonetheless, when measuring sequentially, first an excitation spectrum was measured, then an emission spectrum, and finally another excitation spectrum. In case of significant differences between the two excitation spectra the results were discarded.

The combination of low fluorescence quantum yield, low laser excitation power, and the blocking of most of the fluorescence counts by the long-pass filter for measurements of the full excitation spectrum, resulted in a poor signal-to-noise ratio for the measured interferograms. That is why a background interferogram was measured away from the molecules (~2 counts/20ms), which mainly consisted of leaking laser light, and which was then subtracted from the fluorescence interferogram (10-30 counts/20ms). Figure 3.4a shows the background-corrected timetrace of four consecutive scans on a somewhat unstable LH2 complex. During the scans, the molecule blinked a few times, most prominently at around 230 s.

The raw interferograms were processed in the same fashion as had been done in the previous chapter for QDI molecules, where the effects of averaging, windowing and zero-padding had been demonstrated in figure 2.9. Figure 3.4b demonstrates the processes on LH2. A single scan (top) has a noticeably lower signal-to-noise ratio than the four averaged scans (middle). All blinking events were excluded from the averaging to prevent Fourier transform artifacts. Consequentially, the applied

Hann-window suppressed the signal far from time zero that mainly consisted of noise (bottom). Figure 3.4c shows the excitation spectra obtained by Fourier transformation of the interferograms shown in Figure 3.4b. The two absorption bands become distinguishable only after averaging and removal of the blinking events while the signal-to-noise level of the spectrum increases drastically after windowing. Lastly, increasing the sampling frequency through zero-padding, (black dashed lines) helps resolve the peaks better without changing the results otherwise.
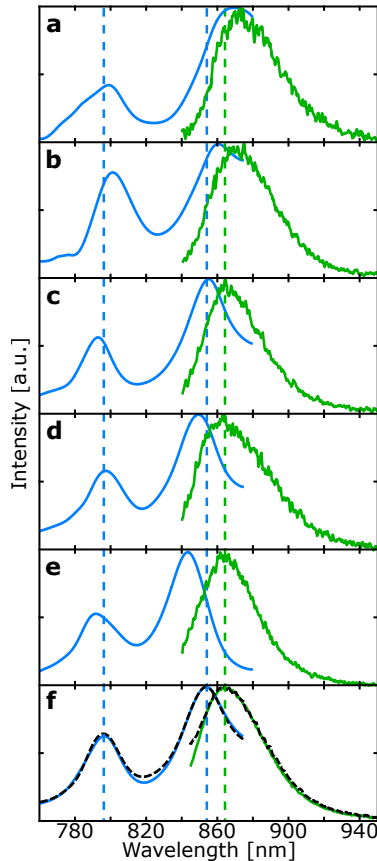
Figure 3.5: *Single complex excitation and emission spectra.* **(a-e)** Excitation (blue) and emission (green) spectra of five distinct LH2 complexes with distinct B850 band position, but comparable emission band positions. **(f)** The sum of all measured excitation (blue) and emission (green) spectra alongside the thin film spectra (black dashed line). Dashed vertical lines: thin film peak positions.

3.3 Excitation and emission spectra

The excitation and emission spectra of hundreds of LH2 complexes were measured. Figure 3.5a-e shows examples of spectra of individual LH2 complexes where the B850 band position varies between 840-870 nm whereas the fluorescence spectra

	B800	B850	emission
Sum	796.5 nm	853.8 nm	864.7 nm
Thin film	796.1 ± 0.2 nm	853.8 ± 0.5 nm	864.8 ± 1.1 nm
Single complex	796.1 ± 3.6 nm	853.7 ± 5.4 nm	866.0 ± 5.4 nm

Table 3.1: *Peak positions.* The band positions for the sum of all single complex spectra, and the average for individual thin film, and single complex measurements.

remain at a relatively constant position. The subtle differences between the individual spectra will be studied statistically in the following. Finally, the bottom panel (figure 3.5f) shows the spectrum obtained when summing the not-normalized spectra of all individual complexes (solid lines). In the same graph, the ensemble spectrum measured on a thin film is shown (dashed lines). The sum spectrum resembles the thin film spectrum despite the spectral heterogeneity of the individual spectra. With the spectral spread of QDI molecules over more than 100 nm and the spectral bias due to the measurement parameters still fresh in mind from the previous chapter, this is not an obvious result. However, at first glance none of the individual spectra deviated dramatically from the ensemble spectrum in either shape or position. That is why the resemblance between the two spectra does not surprise much in this particular case, even though smaller differences will be pointed out later in this chapter.

To quantify the results obtained from the different spectra, the peak positions of the sum, thin film and single complex spectra were determined. For the excitation spectra, the peak finder function in matlab was used (`findpeaks(data)`). The emission data was fitted by a skewed Gaussian function adapted from Rutkauskas et al.[115]. Using these results, not only the peak positions, but also the interband distances were compared to look at both absolute positions as well as relative positions compared to the other bands.

3.3.1 Peak positions

The results of the fitted band positions are given in table 3.1. The thin film data was based on 12 measurements of different positions on the same sample. The single complex data was based on 472 measurements for the B800 band position, 433 for the B850 band position and 283 for the emission band position, using both sequentially and simultaneously recorded data. It can be seen that all values agree well with one other. It is worth noting that the single molecule distribution is quite narrow, especially in comparison to the spectral shifts of more than 100 nm presented in the previous chapter.

The largest outlier in the results is the single complex emission spectral position. While still within the error margin, it is on average red-shifted by approximately 1.2 nm with respect to the sum and thin film result. For the sum spectrum, the
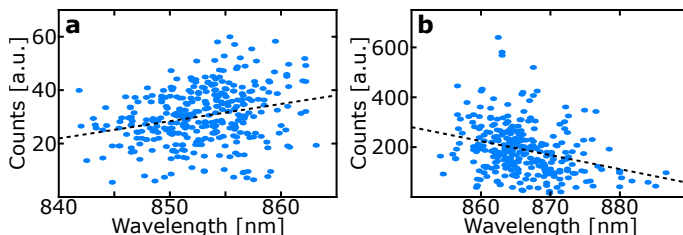
Figure 3.6: *Peak position versus peak intensity.* **(a)** The position of the B850 peak in comparison to the peak intensity. **(b)** The position of the emission peak in comparison to the peak intensity. Dashed lines: least square fit.

spectra of all not-normalized complexes were added up whereas the peak positions were averaged for the single complex spectra. Looking at figure 3.6b, the measured emission spectra had an on average higher emission peak intensity for spectra shifted to lower wavelengths. This implies that for the sum and thin film spectra brighter complexes are weighted stronger while for the single complex spectra all complexes are weighted equally. Therefore, there was an intensity bias towards lower wavelengths for the thin film and the sum spectrum. This bias gets lifted when summing normalized single complex emission spectra, which result in a sum emission peak at 865.6 nm. This shows that the 1.2 nm discrepancy between the ensemble and single molecule measurement is not just a measurement artifact, but due to the ensemble fluorescence spectrum being biased towards lower wavelengths.

The same bias did not occur for the excitation spectra. Here, the intensity scaled with the total rather than the peak fluorescence intensity. In the case of brighter blue-shifted molecules, the laser clean-up filter blocked a larger fraction of the total fluorescence intensity, effectively compensating the increase in fluorescence. Figure 3.6a shows how the trend is in fact reversed, and red-shifted complexes give more counts on average, though the effect is smaller. Though a subtle effect, this illustrates how going to the single particle level does not only lift the ensemble average, but also removes biases imposed onto the system by the experimental parameters. One consequence is that the value found for the Stokes shift in an ensemble measurement would be 1.2 nm (16 cm^{-1}) smaller than the average one for single complexes when looking at them individually.

Figure 3.7a shows the distribution of the peak positions of the excitation and emission bands for a better visualization of the spectral variability. It can be seen that the distribution of the B800 band (blue, FWHM 133 cm^{-1}) is about 25 % narrower than that of the B850 band (red, FWHM 173 cm^{-1}) or the emission band (green, FWHM 168 cm^{-1}), which have a similar width. Dashed lines indicate the average values found for the thin film measurement for comparison.

The narrower distribution of the peak position of the B800 band than that of the B850 and emission band can be explained by the different coupling strengths be-
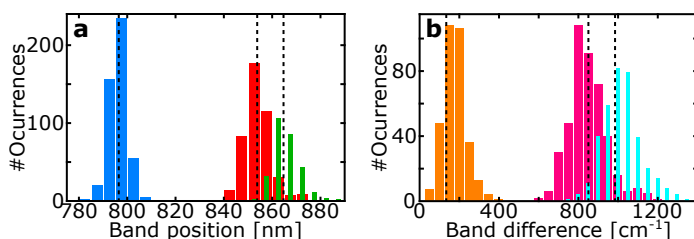
Figure 3.7: *Histograms of peak positions.* **(a)** The distribution of the B800 (blue), B850 (red) and emission (green) band position. **(b)** The interband distance between B850 – emission, i.e. Stokes shift (orange), B800-B850 (magenta) and B800-emission (cyan).

tween nearest neighbors within the two excitation bands. The exact position of the weakly coupled B800 band depends mainly on the energy of the individual chromophores, whereas the strongly coupled B850 band is also influenced by changes in the interactions between the chromophores. As a result, the B850 band exhibits more spectral variability due environmental changes such as temperature or ring deformations[128, 143, 144]. Emission takes place from the B850 band, which is reflected in the similar width of the two distributions.

The small variability of the spectral positions exhibited by the LH2 complexes is quite a rare feature at the single particle level[145, 146]. In LH2 complexes, the protein scaffold effectively holds the chromophores in place and screens them from their environment. The similarity between the thin film spectrum, where LH2 complexes are mainly surrounded by other LH2 complexes, and the sum spectrum of single molecules, where each complex is surrounded by only PVA, supports this explanation. The narrowness of the spectral distribution exhibited by LH2 complexes is favorable for experimental design since all complexes can be efficiently excited with the same narrowband laser and no large spectral shifts need to be taken into account. Only when going to high excitation powers, do significant spectral shifts of up to 100 nm arise in the emission spectra[132].

3.3.2 Interband distances

Besides comparing the positions of the excitation and emission bands, it is also important to look at the relative distance between the different bands within the individual complexes. As was already apparent from figure 3.5, the interband distances are not constant, but vary from complex to complex. The results for the sum, thin film and single complex spectra are summarized in table 3.2. The different measurements agree well with one another.

The intensity bias discussed in section 3.3.1 leads to an ensemble emission spectrum that is biased towards lower wavelengths, while the excitation spectrum is unaffected. That is why the thin film results for the B800-emission and B850-emission interband distances are on average about 30 cm^{-1} shorter than that found for single

	B800-B850	**B800-emission**	**B850-emission**
Sum	$843\,\mathrm{cm^{-1}}$	$978\,\mathrm{cm^{-1}}$	$136\,\mathrm{cm^{-1}}$
Thin film	$848 \pm 8\,\mathrm{cm^{-1}}$	$991 \pm 6\,\mathrm{cm^{-1}}$	$144 \pm 9\,\mathrm{cm^{-1}}$
Single complex	$845 \pm 96\,\mathrm{cm^{-1}}$	$1019 \pm 96\,\mathrm{cm^{-1}}$	$177 \pm 58\,\mathrm{cm^{-1}}$

Table 3.2: *Interband distances.* The interband distances between the two absorption and the emission band the sum of all single complex spectra, and the average for individual thin film, and single complex measurements.

complexes, whereas the B800-B850 interband distance is comparable. This result is even larger than the $16\,\mathrm{cm^{-1}}$ discrepancy found when looking at the average peak positions in table 3.1. This means that when studying the Stokes shift (i.e. the B850-emission interband distance), the ensemble measurement gives a result that is about 20 % too small when measured in a similar fashion. This comparison between ensemble and single molecule results underlines the importance of looking at single molecule data to lift the ensemble average.

Figure 3.7b shows the distribution of the interband distances between the B850 and the emission band (orange, FWHM $135\,\mathrm{cm^{-1}}$), the B800 and B850 band (magenta, FWHM $226\,\mathrm{cm^{-1}}$) as well as the B800 and emission band (cyan, FWHM $225\,\mathrm{cm^{-1}}$). Dashed lines again indicate the corresponding thin film values. It should be remarked that even though the position of the B800 band has a 25 % narrower distribution than the position of the B850 and emission band, the B850-emission interband distance, i.e. the Stokes shift, is 40 % less variable than that between the B800 and B850 band that constitute the exictation spectrum. The relative narrowness of the Stokes shift distribution strongly pinpoints towards a stronger correlation between the B850 and emission band position than between any of the other bands, which will be further looked into in the next section.

The upper limit for the measurement inaccuracy was estimated to be about $30\,\mathrm{cm^{-1}}$. This number was determined by comparing the fitting result of the individual scans of weakly fluorescing complexes before averaging. For most complexes, this value was much smaller. Even so, the $30\,\mathrm{cm^{-1}}$ is significantly smaller than the width of the Stokes shift distribution of $135\,\mathrm{cm^{-1}}$which indicates that the Stokes shift indeed varies from complex to complex and the system exhibits disorder to some degree.

As a last remark, it should be noted that the B800 and emission band are blue-shifted by approximately 3 nm and the B850 band by 5 nm from thin film results published elsewhere[144]. This leads to an even smaller thin film Stokes shift of $120\,\mathrm{cm^{-1}}$ compared to the one found in this work of $144\,\mathrm{cm^{-1}}$. Since the B800 band, that shifted by 3 nm, and the B850 band, that differed by 5 nm, were measured together, it is unlikely that it is a mere measurement artifact. Changes in the growth conditions and environment are known to affect the spectral features[147] which could explain the observed differences. Another possible explanation is the use of
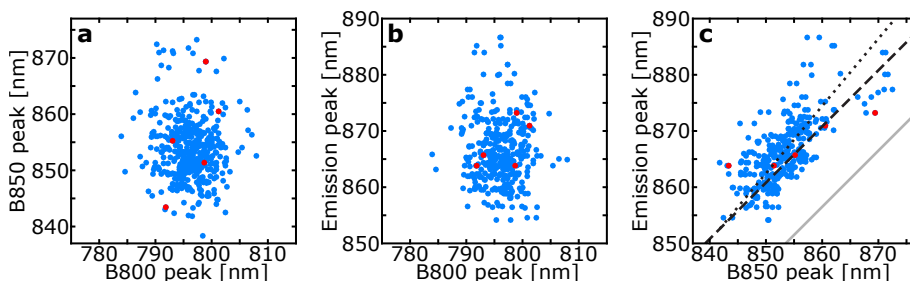
Figure 3.8: *Scatter plots.* **(a)** B800 vs B850 band, **(b)** B800 vs emission band, and **(c)** B850 vs emission band. The dashed line indicates the interpolated value of the thin film result assuming a constant Stokes shift and the dotted line the total least square fit. The solid gray line is the unit-line. The red dots correspond to the spectra in figure 3.5.

different sample preparation or measurement techniques. Minor spectral offsets due to misalignment of the spectrometer may be present, but would not affect the results to this extent.

3.3.3 Scatter plots

The results of the last two sections have already shown that the distribution of the B800 band position has about 25 % less variability than that of the B850 and emission band, while the distribution on interband distances between the B850-emission band is 40 % narrower than that of the B800-B850 or the B800-emission band. This latter result shows that there is a stronger correlation between the B850 and emission band position, than between any of the other bands. To visualize the correlation and see if there exists one between any of the other bands as well, the single complex band positions were plotted in scatter plots in figure 3.8. The positions of the complexes shown in figure 3.8 are highlighted in red.

Figure 3.8a plots the B800 against the B850 band positions. It can be seen that the distribution is taller than it is wide. This is due to the spread in B850 band positions being larger than that of the B800 band. However, no correlation between the two bands can be seen. Since the B800 and B850 band make up the absorption spectrum together, this was not an obvious result. It means that the two absorption rings of the LH2 complex tune their absorption band independent from one another as they react differently to their nanoenvironment. The same elongated shape and lack of correlation can be found when comparing the B800 with the emission band position in figure 3.8b. This is consistent with the emission taking place from the B850 band and the lack of correlation between the B800 and B850 bands.

However, there is a clear correlation between the B850 and emission band, as seen in figure 3.8c. It exhibits a wide distribution of points over a relatively narrow spectral range, making it difficult to determine the linear dependency of the Stokes shift on the band position. As a first approximation, the thin film result is used. Assuming

a constant Stokes shift, it is interpolated on the graph with slope 1 (dashed line). This line does not only sit below the majority of data points as expected, but the slope needed to correctly fit the data appears to be larger than unity. With a total least square fit, a slope of 1.2 was obtained, resulting in a larger Stokes shift for more red-shifted complexes (dotted line). This is in line with a model developed by Novoderezhkin et al. which predicted a larger energy separation between the B850 peak and emission peak for red-shifted complexes due to static disorder and differences in couplings to phonons[136].

3.4   Conclusion

The feasibility to routinely record excitation and emission spectra of weakly fluorescing individual LH2 complexes under physiological conditions was demonstrated. For this, the broadband Fourier transform excitation spectroscopy method was developed from proof-of-principle experiments on synthetic dyes to measurements on biologically relevant systems, demonstrating its potential as a spectroscopic tool to access the excited state manifold. The instability inherent to LH2 complexes at room temperature was circumvented by going to low excitation powers while the resulting low signal levels were overcome by effective data analysis. The results show a remarkably little spectral variation (130-170 cm^{-1}), far below that observed for isolated dye molecules. The lack of correlation between the B800 and B850 band manifests that the two rings react to environmental changes independently, one being weakly and the other strongly coupled. The single complex Stokes shift showed variations and the shift was on average larger for red-shifted complexes, and about 20 % larger than the ensemble Stokes shift. The quantification of this disorder provides important input for both models and the interpretation of experimental results, which will help with the interpretation of the observed long-lasting coherences. This method can be applied to a wide range of systems including those that are weakly fluorescing or with low photostability.

4 | Towards stimulated emission detection of single molecules

With stimulated emission, molecular processes can be probed directly and instantaneously rather than relying on the indirect and slow detection through fluorescence. This comes at the price of signal-to-background ratios of around 10^{-7} that have to be overcome to study single molecules at room temperature. In this chapter, the improvements over earlier efforts to reach single molecule stimulated emission detection are presented together with the steps taken to reach the ultimate sensitivity: shot noise. Stimulated emission depletion measurements verify the alignment of the setup and find the best experimental parameters. Finally, the actual stimulated emission measurements are performed. While sensitivities of up to 10^{-8} were reached, they proved insufficient to detect stimulated emission of a single molecule. Several possible explanations for this and suggestions for further improvements are given.
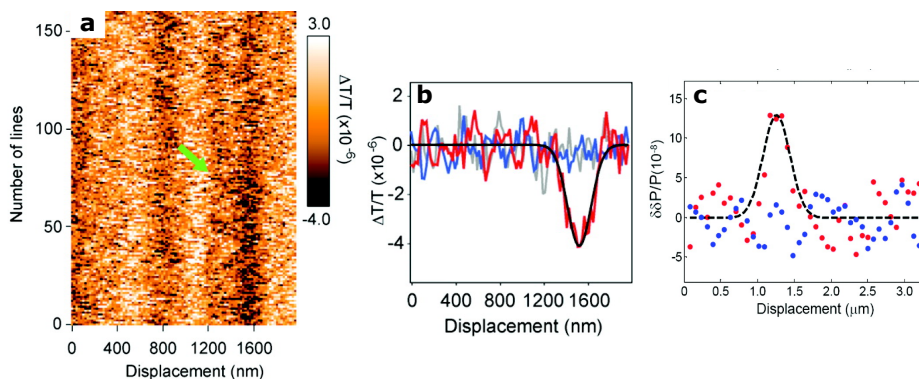
Figure 4.1: *Single particle detection beyond fluorescence.* **(a)** Differential transmission image. The green arrow indicates the photobleaching of the molecule. **(b)** Subtraction of averaged line scans of (a) before from after photobleaching (red). When choosing both averages in on-state (gray) or off-state(blue), no dip is visible. From [48]. **(c)** Averaged line scans of ground state depletion before (red) and after (blue) photobleaching. From [44].

Almost all single molecule experiments at both cryogenic and room temperature rely on the detection of fluorescence[22, 23]. Fluorescence detection is practically background free because of the spectral separation between the excitation beam and the Stokes-shifted fluorescence. However, there are many molecules whose dominant decay pathway is non-radiative, making their detection through fluorescence impossible. One example for this are heme proteins like hemoglobin, which are important in biology and medicine, but which have their fluorescence almost completely quenched[148].

Light harvesting complexes, like LH2 in chapter 3, are another example. They are designed to efficiently transfer energy via non-radiative processes, which goes hand in hand with low fluorescence quantum yields. The measurement on ensembles, at cryogenic temperatures or with increased fluorescence yield through plasmonic enhancement are often necessary[97, 149, 150]. Ensemble spectra are typically too complex to analyze in depth due to an abundance of information, while cryogenic temperatures and the coupling to plasmonic structures change the properties of the complex under investigation.

Several techniques have already moved beyond fluorescence detection at room temperature. Some of these techniques are not fully optical. Examples include the excitation by the electrons of a scanning tunneling microscope[151] or the detection through mechanical force[152]. Various fully optical pump-probe methods have also reached single molecule sensitivity. They include absorption[48], and ground state depletion measurements[44], as well as photothermal contrast[49]. Stimulated emission experiments have almost reached single molecule sensitivity[91].

All of the aforementioned optical techniques relied on the measurement of a very small signal on top of a very large background due to the spectral overlap between the excitation and detection wavelength. A single molecule at room temperature has an absorption cross section of around $\sigma_{abs} \approx 10^{-16}$ cm^2, whereas the beam waist of a diffraction limited beam is about $A \approx 10^{-9}$ cm^2[44]. The size mismatch amounts to $\sigma_{abs}/A = 1 \times 10^{-7}$, i.e. for every photon absorbed by the molecule, at least 10^7 will have passed without any interaction. The level of sensitivity necessary to successfully detect these small differences in signal requires significant noise suppression in the setup independent of the chosen technique. Something that is common to all of them is the population modulation with a pump beam followed by the detection of the changes using a lock-in amplifier.

Figure 4.1 gives examples of measurements on single molecules. In figure 4.1a, the optical absorption was measured through differential transmission using balanced detection, where light, which did not pass through the sample, is subtracted from light that did. Here, a terrylene diimide (TDI) molecule was repeatedly scanned laterally through the focus [48]. The molecule is located at 1500 nm displacement on the x-axis. The green arrow indicates discrete photobleaching, which had been observed in the fluorescence scans that were measured in parallel. Surface roughness and slight variations in the index of refraction give rise to additional features on the scans with roughly the same magnitude and both positive and negative sign. Only when taking the difference between the averaged signal before and after photobleaching as presented in red in figure 4.1b, can the transmission dip due to the molecule be resolved. It has a magnitude of $\Delta T/T \approx 4 \times 10^{-6}$ and averaged for 75 ms/pixel. Ground state depletion measurements have resolved even smaller signals for Atto647N molecules. Figure 4.1c shows the result of averaging several line scans of a ground state depletion measurement before (red) and after (blue) photobleaching[44]. A contrast of $\Delta P/P \approx 1.4 \times 10^{-7}$ was achieved when averaging for 3.5 s/pixel.

It is worth pursuing these techniques despite the increase in experimental complexity and the small signal-to-background ratio compared to fluorescence spectroscopy. Especially stimulated emission should be noted here. Due to the instantaneous nature of the process ($\sim$ fs), it beats all spontaneous energy redistribution channels such as fluorescence and non-radiative decay ($\sim$ ns). Consequently, it can be applied equally well to both fluorescent and non-fluorescent molecules. The time scale at which stimulated emission occurs would also allow for the direct probing of ultrafast coherent excited state processes which currently rely on the indirect probing through fluorescence[46, 47]. According to Einstein, the absorption cross-section σ_{abs} and the stimulated emission cross-section σ_{SE} are equal due to molecular reversibility[153]. Experimentally, it has been shown that $\sigma_{SE} \sim 1 \times 10^{-16}$ cm^2 for single molecules[154] even though the shape of σ_{abs} and σ_{SE} may differ[155]. Still, assuming $\sigma_{SE} \approx \sigma_{abs}$, then the necessary sensitivity is $N_1 \sigma_{SE}/A$ with N_1 the excited

state population. The maximum excited state population of $N_1 = 0.5$ is reached at saturation. Therefore, if the molecule can be found in the excited state with a high probability, stimulated emission can be recorded with $\sim 5 \times 10^{-8}$ sensitivity. Reaching this level to directly measure excited state processes through stimulated emission would therefore be a great asset.

In the following, the journey towards single molecule stimulated emission detection at room temperature is described. First, the adaptations done to the setup used by Min et al.[91] to improve sensitivity are discussed. Then, the steps taken to suppress noise to shot noise levels are discussed. Lastly, preliminary stimulated emission depletion experiments as well as the stage which stimulated emission has reached are described together with an outlook about possible further improvements.

4.1 Dibenzoterrylene (DBT)

The experiments in this chapter were performed with another rylene dye: dibenzoterrylene (DBT, structure shown on cover). The ensemble main absorption peak is at 740 nm when dissolved in toluene[156], while the main emission peak lies around 800 nm for single molecules embedded in an anthracene matrix[157]. When embedded in an anthracene matrix, the molecules are all horizontally aligned in the same direction in the anthracene crystal[157, 158]. They are extremely photostable and can be illuminated for hours under saturation conditions, emitting a total of more than 10^{12} photons[158]. This number is several orders of magnitude higher than that typically reported for single molecules[95–97]. A negligibly intersystem crossing yield due to a large energy separation between the S_0 and S_1 state of around 10^{-7}[159, 160] and a short triplet lifetime of 1.5×10^{-6} s[157] contribute to the photostability. Compared to the fluorescence lifetime of ~ 5 ns[157, 158], the triplet contribution is negligible. At the same time, the molecules are very bright with record photon count rates of around 10^6 photons/s at saturation[157, 158]. Especially the photostability makes DBT an ideal candidate for long stimulated emission measurements at relatively high laser powers.

The sample preparation followed that described by Toninelli et al.[157]. A solution of anthracene in diethyl ether with a concentration of 2.5 mg/ml was prepared. 10 µl/ml of benzene was added to improve the quality of the crystals. The DBT molecules were dissolved in toluene to achieve a 10 µM solution. This solution was further diluted by adding more anthracene/diethyl ether mixture to the desired concentration.

About 20 µL of the diluted solution was spin coated onto a clean glass coverslip at 1000 rpm for 30 s. Afterwards, a solution of 4% PVA in water was spin coated on top of the crystals at 2000 rpm for 50 s. This latter layer helped prevent sublimation of
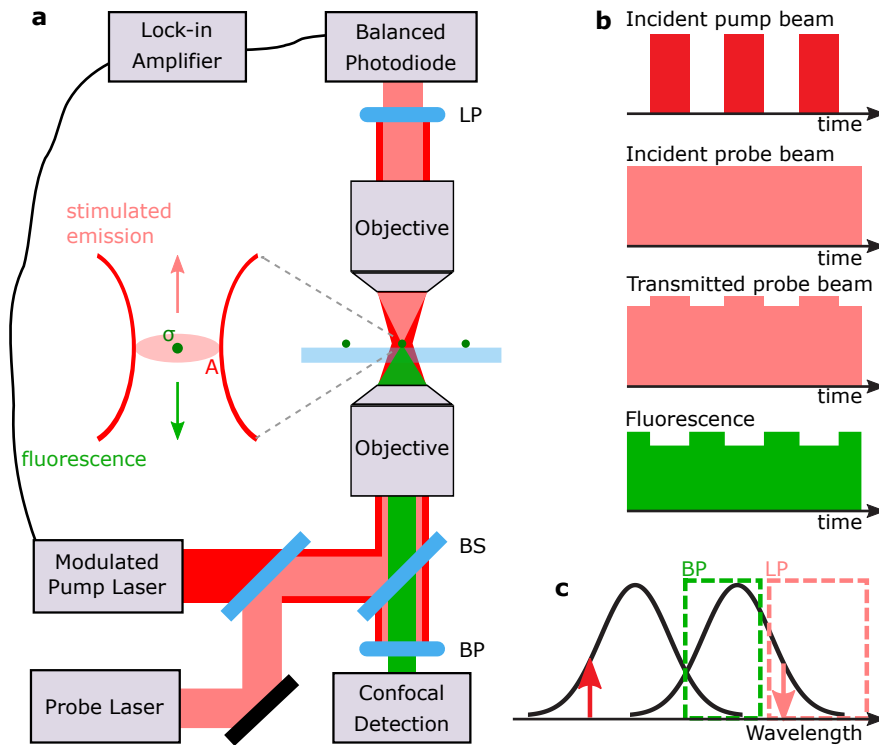
Figure 4.2: *Stimulated emission detection.* **(a)** A modulated pump laser (red) and a probe laser (light red) are coaligned and focused onto the sample. The fluorescence is detected confocally in reflection (green) and the stimulated emission in transmission. **(b)** The incident pump beam creates the population for stimulated emission by depleting fluorescence. **(c)** Detection scheme with a band-pass filter (BP) used for fluorescence and a long-pass filter (LP) for stimulated emission detection.

the crystals from the cover slip and acted as a protective layer for the oil-immersion transmission detection.

4.2 Stimulated emission setup

The setup to measure stimulated emission in pump-probe configuration is sketched in figure 4.2a. The main difference to designs used in previous chapters is that a second objective was placed on top of the sample for stimulated emission detection in transmission.

Two cw laser diodes mounted onto an evaluation board including a high speed module (ic-HG EVAL HG2D and iC-HG iCSY HG8M, iC Haus) were used as light sources. These are integrated circuits designed to drive laser diodes with different settings. The pump laser at 685 nm (QL68J6SA, Roithner Lasertechnik GmbH) was modulated directly at the board, while the probe laser (S8550MG, Roithner Lasertechnik GmbH) was run in cw mode.

Both pump and probe beam were expanded with a telescope to overfill the objective. Before combining them with a hot mirror, part of the probe beam was separated by a beam sampler and focused into an optical fiber for balanced detection (not sketched). The coaligned beams were focused onto the sample with a high NA oil immersion objective (1.4NA, 60x, Nikon Plan Apo λ). The chromatic aberration of the objective was compensated by moving the pump beam slightly out of collimation at the telescope until both beams focused in the same plane.

The fluorescence response of the molecules could be detected confocally in reflection through the same objective as in previous experiments. For this, two band-pass filters were used whose band was situated between the two laser wavelengths (775/50 ET, Chroma and FF01-786/22-25, Semrock). A possible two-photon absorption signal due to anthracene whose emission spectrum lies around 375-500 nm was blocked by a 575 nm long-pass filter (575ALP, Omega Optical).

Stimulated emission was measured simultaneously in transmission with a second high NA objective (Fluar 100x/1.3NA Oil or Achroplan 63x/0.95NA Air, Zeiss). After blocking the pump beam with two 830 nm long-pass filters (BLP01-830R-25, Semrock), the probe beam was focused onto the other input of the balanced photodiode (PDB450C, Thorlabs). The RF output was cleaned by a 1.9 MHz low-pass filter (BLP-1.9+, Mini Circuits) and sent to a lock-in amplifier (HF2LI, Zurich Instruments).

A lock-in amplifier can recover small modulated signals in the presence of an overwhelming background. Through phase sensitive detection, the signal of interest is demodulated while all components that have a different frequency or phase are rejected. In the present case, the pump laser was driven at 1.4 MHz, generated by the lock-in amplifier. The 1.9 MHz low-pass filter had an insertion loss of 0.26 dB at that frequency, corresponding to a 3 % voltage loss.

Only about 25 % of the light entering the microscope reaches the balanced photodiode. About half of this light is lost due to the 50/50 beamsplitter. Another part is blocked by overfilling the bottom objective. The remainder is lost by absorption and scattering along the beam path.

Figure 4.2b sketches the principle of pump-probe stimulated emission and stimulated emission depletion. A modulated pump beam (red) and a probe beam (light red) are focused onto a molecule. Whenever the pump beam is turned on, stimulated emission leads to an increase in the intensity of the transmitted probe beam. At the same time, increases in stimulated emission lead to a decrease in fluorescence signal, a process called stimulated emission depletion (green).

As already discussed in section 1.1.1, excited state absorption, stimulated emission and ground state depletion compete in pump-probe measurements. Stimulated emission and ground state depletion lead to an increase in signal strength of the transmitted probe beam while excited state absorption results in a reduction of the
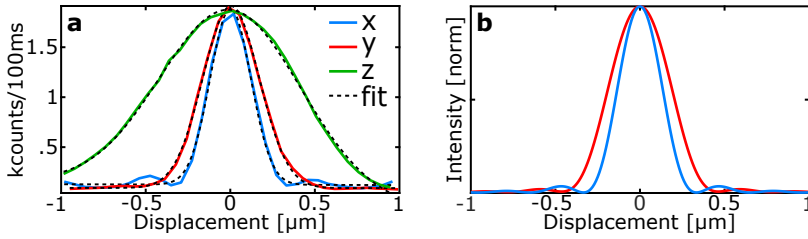
Figure 4.3: *Beam waist of focused* 850 nm *probe beam.* **(a)** Luminescence signal of a gold nanoantenna, when scanning the antenna through the focus in the x, y or z direction (blue, red, green). The Gaussian fit is added as a dashed line. **(b)** Simulated x and y intensity.

signal. To avoid ground state depletion, the pump beam wavelength is chosen such that it only overlapped with the absorption band of the molecule and the probe beam wavelength such that it only overlapped with the emission band as drawn in figure 4.2c. According to models, excited state absorption is not expected at 850 nm excitation[160, 161].

The ideal depletion power for both pump and probe beam is achieved near their respective saturation level. For the pump beam, the excited state population is maximum at this point without losing modulation depth. For the probe beam, the depletion signal starts saturation around 50 % depletion level and can in principle reach up to 100 %[162].

The actual beam waist of the 850 nm probe beam linearly polarized along y has been determined by scanning a gold nanoantenna through the focus in all three dimensions while measuring its luminescence signal. The antenna was chosen such that it could be excited by the 850 nm laser, which is not possible for DBT molecules. The results are shown in figure 4.3a for probe power 90 μW in front of the microscope. In each dimension, 15 consecutive scans were averaged with an integration time of 100 ms/pixel each. The beam in the x-dimension (blue), is slightly narrower than the beam in the y-dimension (red). In the z-dimension (green), the focus is longest. The profile of the focus was fitted with a Gaussian in all three dimensions (black dashed) to determine its $1/e^2$ beam waist (compared to equation (1.5)): In the x-direction it was 240 nm (370 nm), in y it was 333 nm (370 nm), and in z it was 833 nm (867 nm).

The more rigorous description of a focused Gaussian beam waist by Richards and Wolf [163, 164] could be modeled in the xy-plane using a matlab code provided by Li[165, Appendix A]. Using the parameters $\lambda = 850$ nm, $NA = 1.4$, $n = 1.52$ and y-polarized light, the simulated results are plotted in figure 4.3b. The beam waist is 230 nm in the x-direction and 320 nm in the y-direction. These values are in excellent agreement with the experimental results, with only a 4 % discrepancy. Even the Airy rings around 0.5 μm in the x-direction are reproduced.

With this value, the stimulated emission contrast for DBT molecules can be calculated based on a 1.4 NA objective and a probe beam wavelength of 850 nm. DBT has an extinction coefficient ϵ of about 42 000 l/mol/cm^{-1}[166]. From this value, the single molecule absorption cross section can be approximated as $\sigma_{abs} = \ln(10)\epsilon/N_A \approx 1.6 \times 10^{-16}$ cm^2, with N_A Avogadro's number. Taking the larger beam waist in the y-direction at $d = 333$ nm, the detection area is $A = \pi d^2 \approx 3.5 \times 10^{-9}$ cm^2. Assuming $\sigma_{abs} \approx \sigma_{SE}$, and excited state population $n_1 = 0.5$ at saturation, the stimulated emission contrast becomes $n_1\sigma_{SE}/A = 2.3 \times 10^{-8} n_1$, i.e. for every photon absorbed by the molecule, at least 4×10^7 will have passed without interacting with it. This is slightly smaller than the previous estimate for a generic molecule of 5×10^{-8}.

The setup used in this work differs from that used by Min et al.[91] in a few aspects to increase sensitivity and workability. Using a balanced photodiode instead of a regular photodiode compensates for fluctuations in the probe beam intensity. In addition, the DBT molecules used in this experiment were embedded in a crystal matrix so that the polarization of the laser beam could be easily aligned with the dipole moment of the molecule, instead of dealing with random molecular orientations in a flow cell.

Additionally, cw excitation was chosen instead of pulsed ultrafast lasers. This did not only eliminate the necessity to overlap the two beams in time, but also made it possible to get results faster. In cw mode, the molecules could be excited continuously without the limitation of one excitation per laser duty cycle as in pulsed excitation. The faster the signal can be detected, the less problematic instabilities such as drifts become. Still, it could be argued that pulsed lasers should be preferred over cw lasers due to their high peak powers, which lead to saturation at lower average excitation powers. However, higher peak powers, and thus shorter pulse durations, go hand in hand with a reduced probability of finding the molecule in the excited state per excitation cycle[167, 168]. This reduction in excited state population decreases the amount of stimulated emission signal, and is therefore counterproductive.

4.3   Noise analysis

In this section, the steps that were taken to reach shot noise levels are discussed. Careful analysis of the system has identified potential noise sources, which include the light source, reflections in the beam path, electronic noise, background luminescence, and photodamage. In the following, the approaches to minimize their effects are addressed.

4.3.1 Shot noise

There is a discrete amount of photons in each laser beam. While the detected intensity is constant on average, there are random statistical fluctuations that lead to a variation in the number of photons over time. This photon statistical noise is called shot noise and the smaller the number of photons n, the more this effect plays a role. It follows a Poisson distribution, scaling as the square root of the number of photons

$$\text{shot noise} \propto \sqrt{n}. \tag{4.1}$$

The sensitivity S is defined as the smallest fractional change in signal that can be detected by a measurement. The threshold for this is the signal-to-noise ratio SNR=1. Therefore, in an ideal case

$$\text{SNR}_\text{shot} = \frac{Sn}{\sqrt{n}} = S\sqrt{n} \equiv 1$$

$$\Rightarrow S = \frac{1}{\sqrt{n}}. \tag{4.2}$$

For the experiment to be successful, S needs to be as small as possible. This is equivalent to maximizing n, which can be derived by taking the ratio of the laser power P_{las} with the energy per photon $E_{ph} = hc/\lambda$, with h the Planck constant and c the speed of light such that

$$n(t) = \frac{P_{las}\lambda}{hc}t. \tag{4.3}$$

According to this expression, n, can be maximized by either increasing the laser power or by measuring over a longer time interval. Both parameters cannot be increased indefinitely. The higher the excitation power, the faster the molecule is photodamaged and, at some point, the signal may become saturated. The longer the integration time, the longer the experiment takes and the more effects such as sample drift play a role.

In an actual experiment, the signal-to-noise ratio can be determined as the ratio between the mean of the signal and the standard deviation of the noise. The achievable sensitivity becomes

$$\text{SNR}_\text{meas} = \frac{Sn}{\text{std}(n)} \equiv 1$$

$$\Rightarrow S = \frac{\text{std}(n)}{n}. \tag{4.4}$$

Light source

The first step towards shot noise limited signals is a shot noise limited light source. Different laser diodes at 850 nm were compared. They are listed in figure 4.4 (all
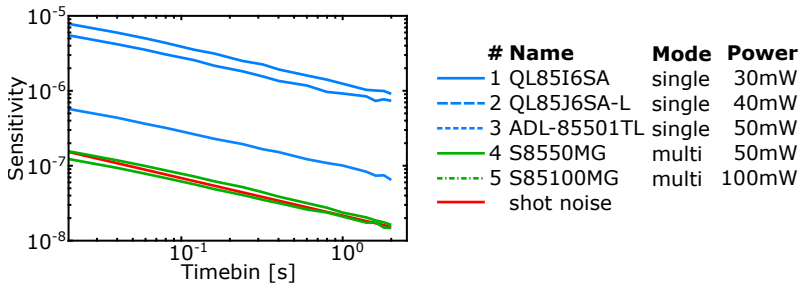
Figure 4.4: *Sensitivity reached with different* 850 nm *laser diodes at* 500 µW *excitation power.* Blue: single mode diodes, Green: multimode diodes, Red: calculated shot noise

Roithner Lasertechnik GmbH). The laser light was split by a 50/50 beamsplitter, where one arm was focused onto one input of the balanced photodiode and the other arm into a fiber connected to the other input. The laser power was chosen such that 500 µW reached the photodiode at each input. The RF output of the balanced photodiode was sent to the lock-in amplifier and the demodulated output was recorded with time bins of 20 ms.

Equation (4.4) was used to calculate the sensitivity of the lasers. The sensitivity for larger time bins was calculated by averaging more and more data points up to integration times of 2 s. The results were compared to the shot noise level calculated with equations (4.2) and (4.3) using $P_{las} = 500\,µW$ and $\lambda = 850$ nm. Figure 4.4 shows the results, where the sensitivity S is plotted against the integration time. Due to the $n^{-1/2}$ relationship of equation (4.2), it is plotted on a log-log scale. The single mode lasers (blue) all have a sensitivity that is one to two orders of magnitude worse than shot noise limit (red). However, the multimode diodes (green) are right at shot noise level. In all ensuing experiments, diode 4 (S8550MG) was used.

Reflections of the beam path

A small fraction of the laser beam is reflected at each interface in the beam path. Interference effects arising from back-reflections can be avoided by slightly tilting all optical elements in the beam path. However, back-reflections cannot be avoided, wherever the laser is focused onto an interface. That is why the beam was only expanded in the telescope without using a pinhole to clean its shape.

The laser focus at the glass-air interface, where the molecules are situated cannot be avoided since a tight focusing onto the molecule is inevitable for single molecule stimulated emission measurements. Whenever the light is focused onto the surface of the coverslip, the noise level of the transmitted beam increases significantly. This effect is illustrated in figure 4.5a. The sample was scanned over 2 µm laterally in 20 steps of 100 nm each with an integration time of 10 ms/pixel while the demodulated signal of the lock-in amplifier was recorded. The positive (red)
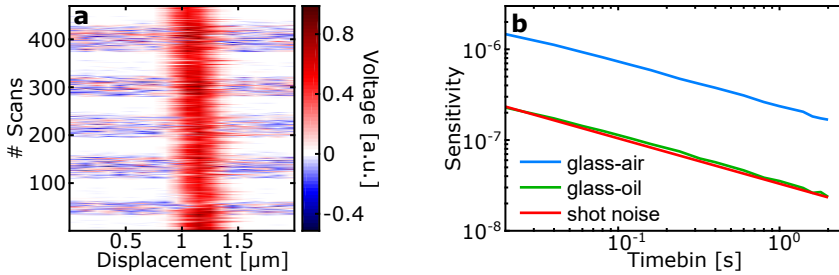
Figure 4.5: *Backreflections off coverslip* **(a)** Repeated measurement of the demodulated lock-in amplifier signal while the focus drifts in and out of the glass-air interface of the coverslip. **(b)** Measurement sensitivity when focusing onto a glass-air (blue) or glass-oil (green) interface, compared to shot noise (red).

signal around $x = 1.2\,\mu$m corresponds to a gold particle in the focus. The scans oscillate between periods of little noise appearing almost white and noisier periods, appearing as blue-and-red areas. The areas of more noise can be linked to the focus at the coverslip-air interface. The standard deviation of the noisy parts is 0.151 V compared to 0.011 V for the less noisy parts, which is about one order of magnitude difference.

A noise increase by one order of magnitude due to a slight focal displacement is not acceptable. While the molecules cannot be moved away from the glass surface, the refractive index mismatch at the glass-air interface ($n_{glass} = 1.515$ vs $n_{air} = 1$) causing it can be avoided by placing an index-matching material on top of the coverslip[55]. A drop of immersion oil was chosen ($n_{oil} = 1.518$, Immersol 518 F, Zeiss) and the transmitted signal was detected with an oil-immersion objective directly immersed into that drop.

Noise analysis similar to that for the laser noise in figure 4.4 was performed to compare the sensitivity levels when focusing on either a glass-air interface or a glass-oil interface. The results are shown in figure 4.5b. The sensitivity when at the glass-air interface (blue) is about an order of magnitude worse than that for the glass-oil interface, which is comparable to the shot-noise level (red). This is in good agreement with the standard deviation calculated found for figure 4.5a, which also showed a sensitivity difference of one order of magnitude.

4.3.2 Electronic noise

Another source of noise is electronic noise. It includes any disturbance in the electrical signal that may lead to interferences or crosstalk[169]. Differences in the potential between different grounded components or any other loops created in the setup are capable of creating interferences. They arise when devices are interconnected in a way that multiple paths to ground exist that form loops.
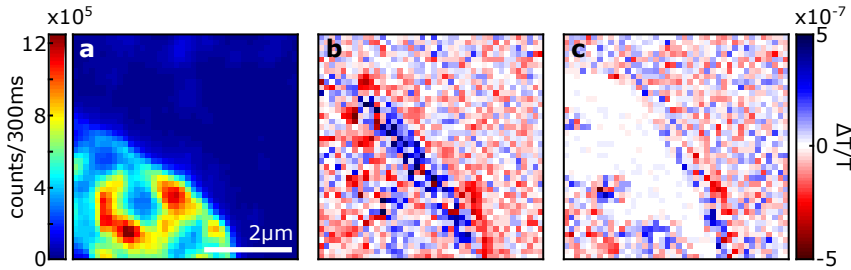
Figure 4.6: *Gain saturation.* **(a)** Fluorescence image with an anthracene crystal with high DBT concentration in the left bottom corner. **(b)** The demodulated signal of the lock-in amplifier when choosing gain 10^4 V/A, and **(c)** 10^5 V/A.

A good example for a loop is one created between the lock-in amplifier, the balanced photodiode and the Adwin. The balanced photodiode is connected to the Adwin through the lock-in amplifier. When connecting one of the monitor outputs of the photodiode directly to the Adwin at the same time, a loop between photodiode, lock-in amplifier and Adwin is created and more noise at the modulation frequency is recorded than without the monitor cable attached.

To address electronic noise issues, the entire setup has been systematically tested for loops and potential differences. In the end, it was possible to get rid of all the electronic noise, with 100 nV of unknown background remaining at the modulation frequency. However, this constant signal does not scale with any of the experimental parameters such as laser power, modulation frequency or gain. When working with signals that are significantly larger than the background noise, for example by choosing a large gain at the detector or measuring at larger probe powers, this noise component consists of a constant offset that disappears into the remaining noise.

Another related source of noise is the saturation of a measurement channel. When one Adwin channel is close to saturation, crosstalk to the other channels occurs. If the signal variability in any of the other channels is of the order of the crosstalk or even smaller, it will be picked up by it as a false signal.

The balanced photodiode used throughout this chapter comes with an adjustable gain between 10^3-10^7 V/A. Only gains up to 10^5 V/A are feasible at a modulation frequency of 1.4 MHz due to bandwidth reduction with increasing gain. When taking into account the quantum efficiency at 850 nm, the conversion factor of the balanced photodiode is 0.255 A/W × gain for 50 Ω impedance. A gain of 10^4 V/A was found to be ideal. At smaller gains, the signal became too small to be fully resolved by the lock-in amplifier. For higher gains, the difference between the two channels of the balanced photodiode occasionally saturated the signal sent to the lock-in amplifier.
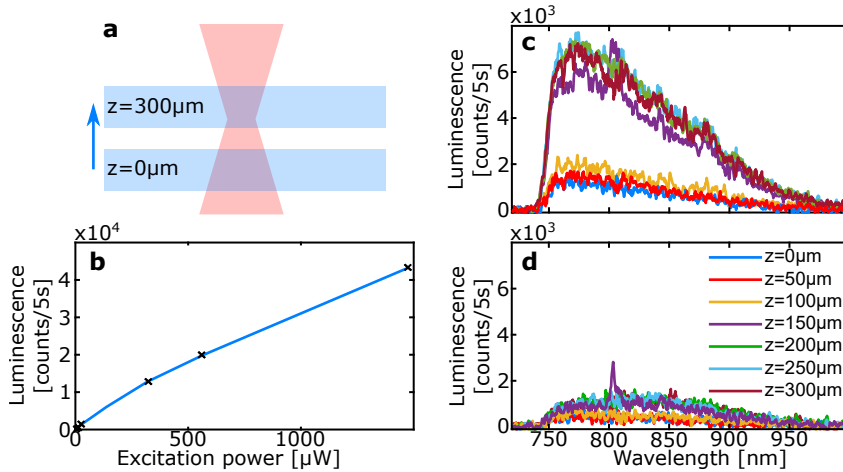
Figure 4.7: *Background luminescence.* **(a)** Schematic of scanning the coverslip through the focus. **(b)** Power-dependence of the luminescence signal. Focus dependent luminescence using an oil immersion objective and **(c)** a glass coverslip, or **(d)** a quartz coverslip.

Figure 4.6 shows an example of this latter challenge. Figure 4.6a depicts the fluorescence image of a highly concentrated DBT sample measured with the APD. In the bottom left corner, an anthracene crystal with a high DBT concentration can be seen as a bright area. The differential signal recorded with the balanced photodiode with gain 10^4 V/A and 10^5 V/A, and demodulated by the lock-in amplifier, is shown in figure 4.6b and c. At gain 10^4 V/A, some features on and especially at the edge of the crystal are visible. They can be assigned to refractive index changes leading to different probe beam intensities reaching the balanced photodiode[48]. At gain 10^5 V/A, these differences in probe beam intensities become so large that they saturate the RF output of the balanced photodiode, leading to a signal that is almost zero.

4.3.3 Background luminescence

The laser beams do not only excite the molecule under investigation, but also anything else in their path that luminesces. The resulting background luminescence does not significantly contribute to the stimulated emission signal. However, it may dominate the fluorescence signal measured on the APD for a saturated system. If the fluorescence signal of the molecules is obscured by the background luminescence, a correct alignment onto a molecule becomes less precise to impossible.

The 685 nm pump laser was used to quantify the effect of background luminescence when scanning a clean coverslip through the laser focus. 850 nm excitation would give a similar result, though red-shifted to wavelengths larger than the excitation wavelength. 140 µW laser power was sent into the microscope via a 10/90 beamsplitter and the reflected laser light filtered out with a 740 nm long-pass

filter (740AELP, Omega Optical) before recording the luminescence on the emccd camera. The coverslip was scanned through the focus using the full 300 μm range of the piezo scanner such that the focus coincided with the glass-air interface at $z = 150$ μm. As sketched in figure 4.7a, this means that for $z = 0$ μm the focus was above the coverslip, whereas for $z = 300$ μm it was inside the coverslip, which has a thickness of 170 μm.

Figure 4.7c shows the luminescence spectrum that was recorded in steps of 50 μm with an integration time of 5 s each. Any ambient background was removed from these traces by also measuring a spectrum with the laser blocked. Around $z = 150$ μm, the counts reaching the spectrometer increase by a factor of 4. Therefore, there is more luminescence when the laser is focused into the coverslip than into air. Repeating the same experiment with a quartz coverslip as shown in figure 4.7d yields the same effect, though reduced by a factor of 2. Exchanging the oil immersion for an air objective removed the remaining factor of 2 such that the background signal did not depend on the coverslip position any more. Finally, the background luminescence disappeared altogether when removing the objective and coverslip and reflecting the signal onto the emccd camera with a mirror instead.

Overall, the glass coverslip contributed most to the background luminescence followed by the immersion oil and the objective. In spite of these findings, glass coverslips were used in all of the following experiments to ensure index-matching which is key to shot noise limited measurements. Instead, the detection scheme sketched in figure 4.2 is employed, where a band-pass filter is placed into the APD detection path. The luminescence due to the higher wavelength probe beam is completely blocked this way and only the part due to the 685 nm pump laser overlapping with the band-pass window remains.

A power-dependent measurement of the background luminescence was performed on a glass coverslip at $z = 150$ μm. In figure 4.7b, the photon counts in the range of 760-790 nm, which roughly overlapped with the detection window of the band-pass filter, were integrated and plotted against the laser power. The resulting curve is linear even at higher excitation powers. Once the fluorescence is saturated for a molecule, the background luminescence continues to grow linearly without any significant increase in fluorescence counts from the molecule until the signal disappears into the noise.

While relevant for fluorescence detection, the luminescence does not affect the stimulated emission signal significantly. The luminescence signal is $\sim 10^3$ photons/s, while the incident power of 14 μW corresponds to around 10^{14} photons/s using equation (4.3). Therefore, the luminescence accounts for $\sim 10^{-11}$ of the signal, and is thus far below the expected stimulated emission signal for a single molecule.
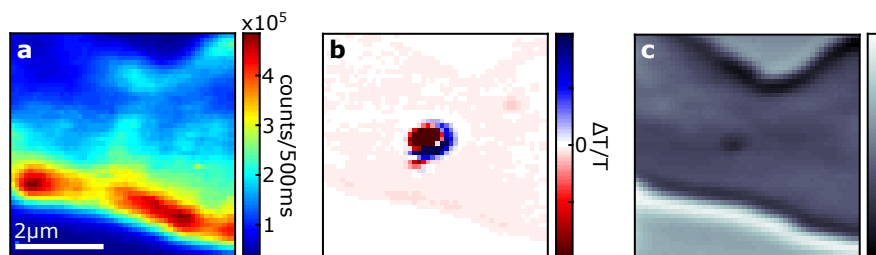
Figure 4.8: *Photodamaged anthracene crystal.* Damage of anthracene crystal in the center of the image visible on all detection channels: **(a)** APD **(b)** demodulated lock-amplifier, and **(c)** monitor signal.

4.3.4 Photodamaged anthracene crystals

When illuminating the anthracene crystals in which the DBT molecules are embedded with a high probe power, they may get photodamaged. Figure 4.8 gives an example of a measurement on a sample with a high DBT concentration, where the center of the image had been exposed to a high probe power for an extended amount of time before the measurement. Figure 4.8a shows the fluorescence counts measured in reflection with the APD. While there is a brighter area in the center of the image, it is still less intense than the fluorescence counts collected at the lower edge of the crystal.

Figure 4.8b shows the demodulated signal of the lock-in amplifier. There is a large signal of both positive and negative amplitude in the center of the image resulting from the photodamage. It is more than an order of magnitude larger than the background at the crystal and even saturated the lock-in amplifier when using the normal settings for stimulated emission detection. This signal disappears when blocking the pump beam. The transmitted probe beam measured at the monitor output of the balanced photodiode is presented in figure 4.8c. It shows a decrease in intensity where the probe beam illuminated the sample. This underlines how the photodamage changed the optical properties of the anthracene crystal.

This effect has been minimized by minimizing the beam exposure time. In between measurements, the shutter blocks the lasers from reaching the sample, which prevents the sample from being photodamaged.

4.4 Stimulated emission depletion of single molecules

In this section, stimulated emission depletion was studied. As a background free indirect measure for stimulated emission, it served to characterize the quality of the setup and its alignment, as well as to determine the appropriate experimental parameters. While the pump beam at 685 nm can excite the molecule efficiently, the probe beam at 850 nm was chosen such that it only overlaps with the emission
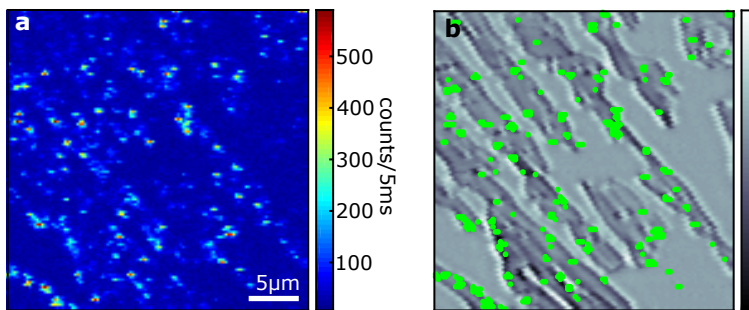
Figure 4.9: *DBT sample.* **(a)** Fluorescence counts detected by APD. **(b)** Transmitted laser power to visualize anthracene crystals (darker areas = less transmission). The green dots correspond to molecules with more than 175 counts/5ms in (a).

spectrum to avoid a ground state depletion signal. A coverslip containing gold nanorods was used to coalign the two beams on the sample and optimize the setup in general. Gold nanorods have a stable luminescence signal and both lasers can excite them efficiently.

Once the full setup was aligned, the DBT single molecule sample was placed onto the microscope. A typical fluorescence image is shown in figure 4.9a, where each bright spot corresponds to a DBT molecule. The stimulated emission depletion signal of several DBT molecules were measured. All of the measurements presented in the following were performed on the same representative DBT molecule. The other measured molecules were equally photostable and had a comparable fluorescence count rate. Before the measurement, the polarization of the two beams was aligned with the dipole moment of the molecule via $\lambda/2$-waveplates placed into both beams. The optimal polarization of the pump beam should lead to maximum fluorescence counts on the APD, while the ideal probe beam alignment should lead to maximum depletion.

Figure 4.10 shows the typical behavior of a single DBT molecule when excited and stimulated down using different pump and probe powers. All graphs have been recorded on the same molecule. Figure 4.10a shows an example of a depleted fluorescence signal of a single DBT molecule for 7 µW pump power and 3 mW probe power measured in front of the microscope. After 5 s of excitation by only the pump beam, the probe beam was added which lead to a noticeable drop in fluorescence counts from around 550 to 190 counts/25ms. Thanks to the band-pass scheme discussed in section 4.3.3, the increase in background luminescence due to the probe beam is minimal. When measuring off the molecule, 11 counts/25ms background remain for the pump beam, but only 2 counts/25ms for the probe beam despite its 3 mW excitation power. In all of the following graphs, the background counts have been removed.
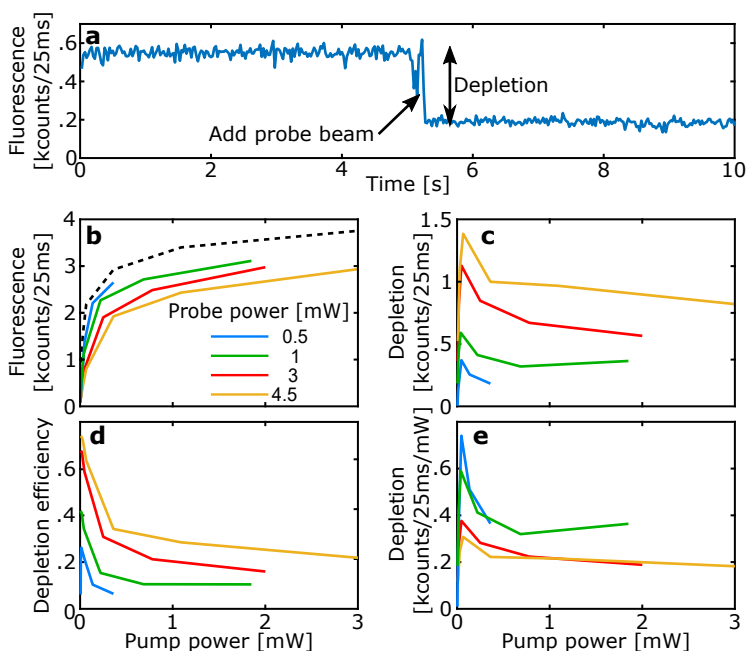
Figure 4.10: *Stimulated emission depletion of a single DBT molecule.* **(a)** Fluorescence, after 5 s the probe beam is switched on. **(b)** Saturation curves using different probe powers. Dashed line: no probe beam. **(c)** Depleted counts, **(d)** depletion efficiency, and **(e)** depleted counts normalized by the probe power.

Ideally, stimulated emission experiments should be performed near saturation power. Then, the maximum amount of population can be found in the excited state without losing contrast by saturating the modulation of the pump beam. Figure 4.10b shows the saturation in the absence of the probe beam as a black dashed line. Saturation curves were also measured using different probe powers between 0.5-4.5 mW. The higher the probe power, the less fluorescence counts are recorded for the same pump power due to stimulated emission depletion.

The saturation level is ~100 μW pump power or ~70 kW/cm² intensity assuming a focal area of 7×10^{-10} cm² and that 50 % of the excitation power reached the sample, leading to a maximum fluorescence count rate of around 2×10^5 counts/s. The fluorescence count rate agrees well with the ones reported in literature of 4×10^5 counts/s[158] and 1×10^6 counts/s[157]. However, the reported saturation intensity was 75 kW/cm²[158] or 1000 kW/cm²[157]. It is unclear how the larger value in the latter case was obtained. As discussed in section 4.1, the triplet state of DBT can be neglected due to a combination of a low intersystem crossing probability ($\sim 10^{-7}$) and a low triplet state lifetime (~ 1.5 μs). Therefore, the saturation should be almost completely ascribed to the S_1 lifetime of ~ 5 ns $\gg 10^{-7} \times 1.5$ μs. A fluorescence lifetime of 5 ns corresponds to a fluorescence count rate of 2×10^8 counts/s, three orders of magnitude larger than the measured one. While around one to two

orders of magnitude in difference could be explained by the detection efficiency due to the 50/50 beamsplitter, the quantum yield of the APD, and the cut-off filter, three orders of magnitude seems a bit excessive compared to the 5-10 % found for QDI in section 1.3.2. Due to the good agreement with results reported elsewhere, significant misalignment are ruled out. One possible explanation would be that the system spends more time than anticipated in the triplet state.

In the following, the effect of both pump and probe power on the stimulated emission depletion signal will be studied. In the linear excitation regime, the higher the pump power, the more population can be found in the excited state. The higher the probe power, the more likely a stimulated emission event takes place. Both lead to an increase in depletion rate. The number of depleted fluorescence counts is shown in figure 4.10c. For all probe powers, the largest depletion is achieved around 100 µW pump power, after which the counts decreases again. This pump power corresponds to the saturation power. Saturation alone would only account for a flattening of the curve and not a decrease for higher pump powers. The reabsorption of a photon after a stimulated emission took place becomes more probable at high laser powers. In that case, the molecule has a chance to emit another photon via the fluorescence pathway after the stimulated emission event, reducing the depletion counts. Therefore, the observed drop in depletion does not necessary correspond to a drop in stimulated emission.

The depletion efficiency is the ratio between the fluorescence counts before and after depletion. A depletion efficiency of 1 corresponds to all fluorescence being depleted, and an efficiency of 0 to no depletion. As seen in figure 4.10d, the larger the pump power, the smaller the depletion efficiency. This can again be ascribed to the reexcitation after stimulated emission depletion at higher pump powers. At the same time, a higher probe power leads to a larger depletion efficiency of up to 0.7 for 4.5 mW probe power.

It appears as if the depletion efficiency does not scale linearly with the probe power. That is why the depleted counts normalized to the probe power are shown in figure 4.10e. Here, the lowest probe power leads to the highest depletion so that a larger relative depletion is achieved. This is in line with the nearly exponential decrease in fluorescence intensity with increasing probe powers[162]. Stimulated emission saturation occurs at 50 % reduction in fluorescence counts, which was only reached for the higher probe powers of 3 mW and 4.5 mW. The saturation of stimulated emission depletion for larger probe powers may again be an artifact due to the reabsorption at larger probe powers. This would only decrease the depletion signal negatively, without affecting the stimulated emission signal itself. Additionally, a more intense probe beam will lead to a reduction in shot noise, and the depletion saturation is partially counterbalanced by improved noise levels. That is why stimulated emission was measured at both moderate and high probe powers

in the following, while the pump power was kept near saturation at 100 μW for all measurements.

The saturation power for absorption was calculated to be 100 μW and that for stimulated emission as 3 mW, an order of magnitude larger. These quantities had been measured in front of the microscope. They still have to pass through a 50/50 beamsplitter and the objective before reaching the sample. The probe beam overfills the objective, while the dimensions of the pump beam more or less match it.

4.5 Stimulated emission of single molecules

Having achieved a well-aligned setup and a level of sensitivity that exceeds the required 10^{-7}, as seen by fluorescence depletion efficiencies of up to 70 %, the requirements for stimulated emission measurements on a single DBT molecule were met. In this section, stimulated emission measurements on single DBT molecules are performed. Detection in transmission as sketched in figure 4.2 becomes relevant at this point.

Before starting the actual experiments, the full setup was aligned on gold nanoantennas. Their large photothermal signal was also exploited to align the transmitted beam path onto the balanced photodiode[170]. Since it would be impossible to exchange samples without removing the top objective, the DBT sample was spincoated directly onto the same coverslip as the nanoantennas. As the antennas were confined to a certain area on the coverslip, the sample was simply moved away from the antenna area after alignment.

The molecules were first localized by raster-scanning the sample through the focus. Figure 4.9a shows an example, where each bright spot corresponds to a DBT molecule. The transmitted intensity of the probe beam can be detected simultaneously through the monitor channel of the balanced photodiode. The transmitted signal is shown in figure 4.9b, where darker areas correspond to less transmission. These darker areas coincide with the edges of anthracene crystals in which the DBT molecules are embedded[171]. The molecules identified in figure 4.9a by applying a threshold of 175 counts/5ms were superimposed onto the transmission image as green dots. It can be seen that the molecules are mainly found at the edge of a crystal similar to previous work[158]. This effect will become relevant later on.

After recording the confocal image, the two beams were carefully aligned onto a molecule, and their polarization adjusted such that it overlapped with the molecular dipole. Then, the molecule was repeatedly scanned laterally through the focus. The scans measured 4 μm in 20 pixels with an integration time of 500 ms/pixel. The pump beam was set to 100 μW, while different laser powers were tried for the probe beam up to approximately 5 mW, both measured in front of the microscope. The pump beam was modulated at 1.4 MHz and the balanced signal from the photo-
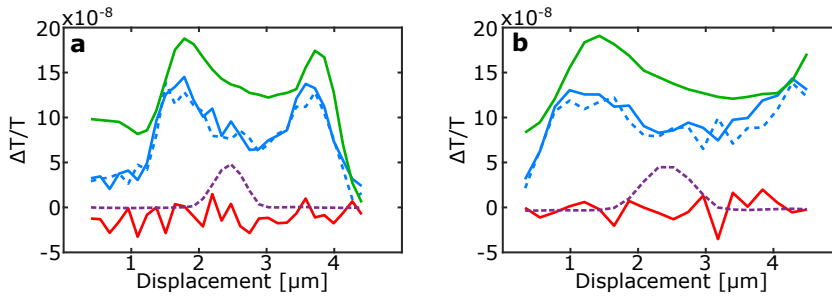
Figure 4.11: *Single molecule stimulated emission measurements.* Two example molecules. The stimulated signal (blue solid), also with the pump beam blocked (blue dashed) and their difference (red solid). For comparison the DBT fluorescence (purple, dashed) and the transmitted probe beam (green) have been added with arbitrary units.

diode with gain 10^4 V/A (2.6×10^3 V/W) was demodulated with an effective time constant of 100 ms. Every other scan, the pump beam was blocked via a shutter to compare the demodulated signal with and without the pump beam on and to remove background noise such as electronic noise.

While only noise was visible at moderate probe powers, features like the one seen in figure 4.6b appeared when increasing the probe power. Figure 4.11 shows two representative examples of single molecules measured at approximately 1.5 mW probe power in front of the microscope. This corresponds to 400 µW probe power reaching the balanced photodiode, as measured with the oscilloscope integrated in the lock-in amplifier. The signal with the pump beam switched on (blue, solid) and switched off (blue, dashed) were both averaged over 50 scans, resulting in a total integration time of 25 s/pixel. They share the same features so that taking their difference resulted in a featureless straight line (red, solid).

The sensitivity of this difference signal amounts ∼10^{-8} using equations (4.3) and (4.4). In comparison, the 400 µW probe power reaching the balanced photodiode the shot noise limited sensitivity would be half that size according to equations (4.2) and (4.3). Despite the factor two in difference, both the measured and calculated sensitivity are at least an order of magnitude better than the estimated sensitivity required by the experiment.

The fluorescence signal of the molecule has been added to the graph (purple, dashed) to find the position of the molecule. The observed features do not overlap with it. However, they do overlap with the transmitted probe signal (green). Due to this similarity, it can be safely assumed that the features are related to the interaction of the probe beam with the sample. The photodamage of the anthracene crystal can be ruled out as a likely cause since it would only show any signal in the presence of the pump beam. The most likely candidate is RF noise of the pump beam modulation adding a small modulation contribution to the probe beam. The more light is transmitted by the sample, the larger the detected modulation becomes. Under

normal circumstances, this modulation would be too small to observe, but with the high sensitivity achieved in this setup, it becomes visible.

As previously shown, DBT molecules tend to be located at the edge of anthracene crystals, which always corresponds to a change in transmitted light. Therefore, features like the ones shown here were visible in all measurements. The detected background signal has an amplitude of $\sim 10^{-7}$, which is comparable to the predicted amplitude of the stimulated emission signal. This shows that a favorable environment with sufficient sensitivity for the detection of stimulated emission of individual DBT molecules had been created. When the background signal is removed, noise of $\sim 10^{-8}$ remains, which should not obscure the stimulated emission signal. While small misalignments, or minor sample and beam drifts cannot be ruled out entirely, it is unlikely that they accounted for an order of magnitude in signal loss.

In the following, more concentrated DBT samples were used to estimate the sensitivity of the stimulated emission signal and to discuss possible reasons for the absence of a signal.

4.5.1 Sensitivity levels

The sensitivity of stimulated emission was characterized by using a sample with a higher DBT concentration. Therefore, more than one molecule was in the focus at the same time. The increase in concentration does not only lead to a larger signal, but also to several side effects that made it less than straightforward than a simple scaling of the signal. Even at these higher concentrations, no stimulated emission signal was visible. The reasons and possible solutions for that will be discussed in the following.

In the single molecule case, the anthracene matrix ensured that all molecules within a crystal have roughly the same orientation. When the laser was aligned along their dipole moment, they all exhibited a similar fluorescence count rate and they were very photostable, withstanding high laser powers over extended periods of time. Similar to the single molecule case, the molecules in the concentrated sample had a tendency to cluster at the crystal edges instead of forming a homogeneous layer. For the concentrated measurements, there was no preferential polarization angle, from which it was concluded that their dipole moments were randomly oriented and the molecules no longer properly embedded inside the crystal matrix.

Another side effect is the emergence of a substantial signal at the APD upon excitation by the probe beam. Figure 4.12a shows the confocal image when exciting with both the pump and probe beam, while in figure 4.12b, only the probe beam was used to excite the same area. A high concentration of DBT molecules can be found in the bottom left corner of the two confocal images. The probe beam wavelength was
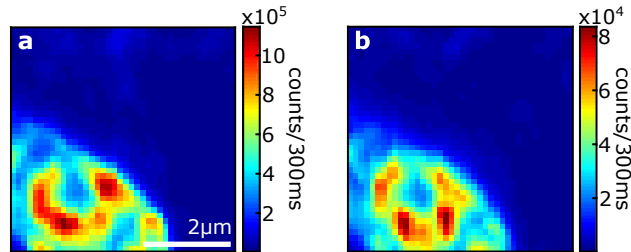
Figure 4.12: *Confocal DBT ensemble measurement.* **(a)** Confocal image of concentrated DBT sample using both pump and probe excitation. **(b)** Confocal image of the same area using only probe excitation.

chosen such that it should not overlap with the absorption cross-section of DBT. In addition, it is above the cut-off of the band-pass filter and the filter should block any longer wavelength luminescence signal. Even so, about 10 % of the counts are due to excitation by the probe laser. Two-photon absorption of the anthracene matrix can be ruled out due to the 575 nm long-pass filter in the APD detection path.

Next, the number of molecules in the focus was estimated. In the single mole-cule image in figure 4.9a, up to 500 counts/5ms were recorded per molecule. In comparison, the count rate of 1×10^6 counts/300ms of the condensed sample in figure 4.12a is 33 times larger. Considering that molecules, whose dipole moments are not perfectly aligned with the polarization of the laser beams, or that are not located near the center of the focused beam, are excited less efficiently, the total number of molecules in the focus is even larger than 33. In practice, the increase in APD counts with the unblocking of the probe beam was so large, that it was even larger than the stimulated emission depletion signal for larger probe powers.

Finally, the determination of a suitable pump power through the measurement of a saturation curve also proved difficult. Figure 4.13a shows the saturation curve averaged over four concentrated points on the sample. It can be seen that the maximum achievable pump laser power of 4 mW, the saturation curve remained almost linear. Due to the random orientation of the dipole moments and the position outside the beam center, many DBT molecules were not excited efficiently and only a small fraction of the molecules had their fluorescence saturated. Still, using the same settings as for single molecule measurements, a signal should be detected due to the large amount of molecules in the focal area.

Considering 33 molecules in the focus and the estimated stimulated emission con-trast of 1.6×10^{-7} for a single DBT molecule (see section 4.2), a $\Delta P/P$ signal around $33 \times 1.6 \times 10^{-7} \approx 5 \times 10^{-6}$ should be visible when looking at the concentrated sam-ple. Figure 4.13b shows a $\Delta P/P$ measurement similar to those shown in figure 4.11 for the single molecule case. Here, the horizontal line including the brightest peak of figure 4.12a has been scanned using the same laser powers as in the single mole-cule case, but averaging over only 300 ms/pixel.
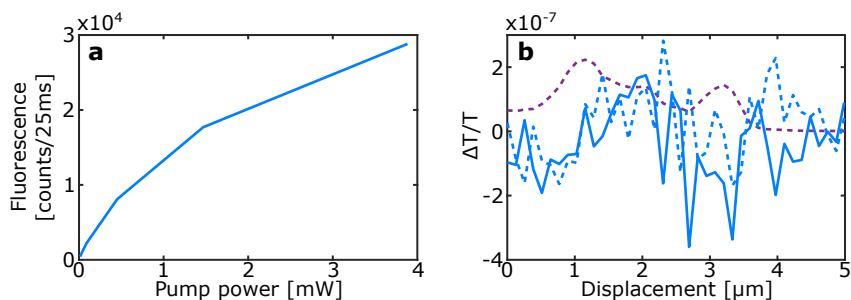
Figure 4.13: *DBT ensemble measurements.* **(a)** Saturation curve averaged over four different areas. **(b)** $\Delta P/P$ measurement for 300 ms with both beams (blue solid) and only probe beam (blue dashed). Fluorescence for comparison in purple.

The measurement with the pump beam blocked (blue dashed) and unblocked (blue solid) look very similar again. Both show a peak around 2 μm displacement. The fluorescence intensity is shown in purple for comparison whose main fluorescence peak is located at 1 μm displacement. The sensitivity of the measurement is again calculated by taking the standard deviation of the difference between the two $\Delta P/P$ traces. It amounts to 1.5×10^{-7}, compared to the three times small shot noise limit of 5×10^{-8}. In contrast, the anticipated stimulated emission signal 5×10^{-6} of from the DBT ensemble of is more than an order of magnitude larger than either of these sensitivities and the stimulated emission signal should stand out clearly from the noise.

There are different reasons for the lack of stimulated emission signal. The alignment should not be one of them. The coalignment of the two laser beams onto the sample was very robust. Each day, the alignment of the entire setup was reviewed on gold nanoantennas before starting the DBT measurements to ensure the quality of the alignment. Only minor tweaks were necessary occasionally. There was a small drift of the sample, mainly in the lateral scanning direction. During the measurement of figure 4.11a for example, the drift was 33 nm for the entire duration of the measurement of 1000 s plus dead time after each line to store the data. Fitting the emission peaks to correct for the sample drift did not change the results significantly and mainly smoothed the graphs due to the interpolation before averaging. The alternating measurements with and without the pump beam on ensured that any sample variations over time entered the both averages equally.

Another possibility would be a competing differential signal of opposite sign, i.e. excited state absorption. However, according to calculations of DBT in literature, a transition from S_1 to a higher excited state with an energy corresponding to around 850 nm is unlikely [160, 161].

A much more plausible explanation is a less tight focus. The ratio between the absorption cross-section and beam waist, σ/A, determines the stimulated emission

contrast. While σ is fixed for the molecule, A depends on the beam shape and focusing ability of the setup. The shape of the 850 nm probe beam could not be cleaned by a pinhole in the telescope to avoid a noise contribution by it. The ensuing less-than-ideal beam shape might have led to a wider beam waist in the focus even though this effect has been minimized by overfilling the bottom objective. Since A depends quadratically on the beam waist, even small decreases can have a significant effect. For example, a 10 % increase in beam waist diameter would already decrease σ/A by 25 %.

DBT is an ideal molecule to study stimulated emission on as far as stability is concerned. However, it requires the pump and especially probe beam at relatively high wavelengths. The larger the probe wavelength, the larger A in accordance with equation (1.5a), and the smaller σ/A for a constant σ. Therefore, changing to a molecule at lower wavelengths or with a higher σ may be a way to drastically improve the stimulated emission contrast. However, it would require the reconfiguration of the setup to the new wavelength regime. Moreover, the substitute molecule would likely be less stable and more prone to spectral variability than DBT.

4.6 Conclusion

A very sensitive setup has been created and systematically tested. Stimulated emission depletion measurements with up to 70 % depletion efficiency demonstrated the correct alignment of the setup. Despite several improvements in the experimental design compared to previous attempts, no stimulated emission signal could be recorded. The most likely factor is a large beam waist in the focus. This can only be improved upon by having a probe beam with a better beam profile, or changing to a molecule, which allows the use of a lower wavelength probe beam.

In the next chapter, the low noise levels of this chapter will be exploited to study the scattering and photothermal properties of gold nanoantennas of various lengths and in various surrounding media.

5 | Photothermal Microscopy

Single molecule setups lend themselves to a range of applications beyond single molecule detection. In this chapter, the pump-probe setup of chapter 4 was adapted to systematically study how focused Gaussian beams interact with plasmonic gold nanoantennas of different lengths, at various positions in the focus, surrounded by different media, and using different detection angles. First, it was studied how the incident field of the probe beam interferes with the scattering field due to the antenna. The interference originates from an interplay between the focal position dependent Gouy phase of the incident beam and the resonance dependent antenna scattering phase. It results in a dispersive interference signal that mainly depends on the antenna dimensions, and that it flips sign when passing through the antenna resonance. Second, a modulated pump beam was added which causes a refractive index change by heating the surrounding medium. The modulated temperature increase leads to a combination of the probe beam scattering off the refractive index gradient around the nanoantenna, and the antenna resonance shifting, which affects the interference between the incident and scattered light. While the latter effect is often ignored when studying smaller particles that mainly absorb, it will be demonstrated that both effects are relevant for antennas with a significant scattering cross-section. The photothermal measurements strongly depended on the photothermal properties of the surrounding medium, which exhibited strong variations around antenna resonance. Comprehensive models complemented all experiments, which agreed well qualitatively with the observed results.

The methods that were developed for single molecule experiments combine excellent sensitivity and spatial resolution. Both are useful features for a range of applications beyond the field of singe molecules. In this chapter, the interaction between plasmonic gold nanoantennas and focused Gaussian beams is investigated using the stimulated emission pump-probe setup developed in chapter 4. Even though the setup remained intact, very different processes were probed that will be introduced in the following.

An antenna typically refers to a macroscopic device that is used to convert radio waves into electric energy and vice versa to facilitate long-distance communication. Optical antennas are their counterpart at the nanoscale, where they link freely propagating electromagnetic radiation to localized electric fields[172, 173]. An optical antenna is any nanometric structure that exhibits resonances at optical wavelengths, though only nanotennas made out of noble metals are considered here. In metals, the collective oscillation of surface charges that are confined to the nanoscopic dimensions of the antenna lead to localized surface plasmons.

In rectangular shaped nanoantennas like the ones used in this chapter, plasmon modes can form along both the short and long antenna axis as sketched in figure 5.1a and b. This gives rise to a transverse and longitudinal surface plasmon resonance respectively. As figure 5.1c shows, the longitudinal mode has a stronger, more red-shifted resonance peak than the transverse mode. The antenna properties including the plasmon resonance, cross-sections and the scattering phase can be derived from the antenna polarizability. It depends on many parameters including the antenna geometry and the refractive index of its surrounding medium. For example, the longer the antenna, or the lower the refractive index of its surrounding medium, the more red-shifted the plasmon resonance becomes[174–177]. The longitudinal resonance mode can be tuned over the entire visible spectrum by increasing the antenna length which already becomes apparent when looking at the solutions in figure 5.1d which contain nanoantennas of increasing lengths[178].

The antenna properties including the resonance tunability get exploited in a wide range of applications including biological and chemical sensing[175, 177, 179], signal enhancement[134, 180], high resolution imaging[24, 181], biomedical treatments[182, 183], and photothermal microscopy[55, 170, 184]. In most applications, various interconnected parameters need to be taken into account when designing the experiments. When it comes to placing a single nanoantenna into a focused Gaussian beam, many of these connections have not been studied systematically. This chapter aims to close this gap by looking how an antenna interacts with a focused Gaussian by measuring the differences in intensity reaching a detector placed in the far field. On the one hand, a decrease in intensity can be observed due to absorption. On the other hand, an additional increase or decrease in intensity can be found due to scattering, which depends strongly on the phase difference
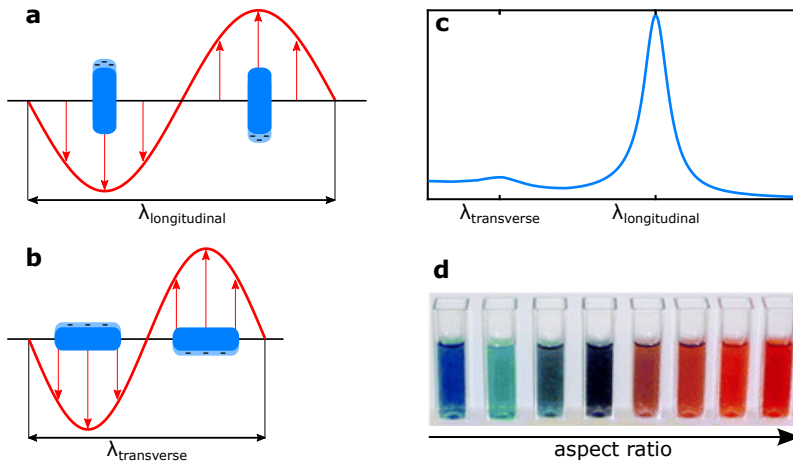
Figure 5.1: *Surface plasmon resonances.* The **(a)** longitudinal, and **(b)** transverse surface plasmon resonance of a nanoantenna when excited by an electric field (red). **(c)** The resulting extinction spectrum with both longitudinal and transverse components. **(d)** Tuning the extinction spectrum through the aspect ratio[178].

between the incident and scattered light. In the far field, a combination between the scattered light and the undisturbed part of the incident beam is detected. For collinear incident beams, the phase difference between them can be directly taken as the scattering phase of the antenna, which undergoes a π phase shift around the plasmon resonance wavelength. However, for focused beams, like those found in a confocal microscope, the Gouy phase has to be taken into account as well. It gradually shifts the phase of the incident beam passing through the focus from $-\pi/2$ to $\pi/2$, while the scattering phase in independent of the focal position[185, 186]. Consequently, the phase difference between the incident and scattered light now depends on both the antenna position inside the focus, and the scattering phase.

The effect of the Gouy phase on axial and lateral antenna displacements is well known, for example in the optical tweezers community[187–189]. However, experiments and models are often based exclusively on the off-resonant excitation at a single wavelength of a gold nanoparticle in just one surrounding medium. The 1st objective of this chapter is to understand how the antenna resonance and position, together with its surrounding medium jointly affect the interference signal reaching the detector. Special attention will be given to the combined effect of the antenna position and plasmon resonance through the interplay between Gouy phase and scattering phase, as well as to the effect of the detection angle and the refractive indices of different media. This does not only improve existing models by systematically probing the entire parameter space, but also is a crucial step towards the understanding of photothermal detection, on which the second objective of this chapter is based.

For photothermal detection, a modulated pump beam is added to the setup. It is ideally chosen resonant with the antenna, which radiates most of the absorbed energy into its environment as heat through phonon-phonon coupling and the change in detected signal due to this heating is probed with the second beam[190, 191]. The temperature increase alters the refractive index of the surrounding medium, which leads to two different detectable effects. The first effect upon heating is the well-studied thermal lens effect, which measures the divergence or convergence of the probe beam on the refractive index gradient around the antenna[170, 190, 192, 193]. Though not related to the Gouy phase[194], the signal depends on the spatial position of the lens inside the focused beam. Many properties have been studied with this technique already, including σ_{abs} of antennas[59], the antenna orientation[57], and the photothermal properties of the surrounding medium[192]. It has even reached single molecule sensitivity[49]. Yet, in most experiments, the spatial dependence of the signal was not explicitly taken into account.

The second effect upon heating is that the refractive index change shifts the plasmon resonance, and the scattering phase of the antenna with it. The ensuing change between the Gouy and scattering phase will be picked up on the detector together with the thermal lens effect. Most models regarding the photothermal effect were designed for small nanospheres that are five times less sensitive to refractive index changes than rectangular antennas[195], and where $\sigma_{abs} \gg \sigma_{scat}$, so that the scattering contribution could be safely ignored when probing off-resonantly[170]. $\sigma_{abs} \sim \sigma_{scat}$ holds in the experiments presented here, and the scattering signal due to change in resonance becomes comparable in size to the thermal lens effect. This effect has been largely ignored so far, even in measurements on rectangular antennas. Instead, it has either been attributed entirely to the thermal lens effect[57, 59], or as a redshift of the plasmon resonance without taking into account the focal dependence of the signal strength and sign[58, 60].

The 2nd objective of this chapter is to show that the change in refractive index upon heating affects both the thermal lens and the shift in antenna resonance. A model to describe both effects will be developed which enables the comparison between various parameters including the antenna position and resonance as well as the surrounding medium. It will be stressed how ignoring certain aspects like the contribution of the resonance shift or the focal position dependence, both common in the field[57–60, 190, 192, 196], can lead to incomplete models and data interpretation.

Both objectives concern the affect that an antenna placed into a focused Gaussian beam has on the transmission of the probe beam by systematically studying the effect of the antenna position, dimensions (i.e. plasmon resonances), detection angle, and surrounding medium for a constant excitation wavelength. The 1st objective is to study the interaction of an antenna with a single focused beam, stressing the

interconnection between the antenna position and resonance. The 2nd objective is to understand how the signal reaching the detector changes when introducing a modulated pump beam to the setup which heats up the surrounding medium, creating a refractive index change. Both the thermal lens effect and the resonance shift are observed through the probe beam. Comprehensive models were developed to qualitatively explain the results observed for the different interconnected parameters.

5.1 An antenna in a focused Gaussian beam

In this section, a formalism to describe the interactions between a focused Gaussian beam and a gold nanoantenna is derived. The expression for the two main components of the derivation, the polarizability of gold nanoantennas, and Gaussian beam optics are first introduced. Then, their combined effect is modeled, showing how the differential signal detected in the far field depends strongly on both the antenna position and spectral and resonance properties. To be able to systematically study a range of parameters and their interplay, approximations are made to keep the computational time down without forsaking the validity of the model to show the correct results qualitatively. Whenever feasible, an intuitive explanation of an effect will be given before starting the mathematical derivation of it.

5.1.1 Polarizability of gold nanoantennas

Different numerical methods exist to model nanoantennas. They are typically limited to certain antenna shapes, or they come with lengthy computation times like the discrete dipole approximation (DDA) and the finite-difference time-domain (FDTD) method[197]. The nanoantennas used in this work can be best described as rectangular boxes of constant height and width, but of varying lengths and which were modeled as prolate spheroids.

Gans theory, which is an extension of Mie theory, offers an analytical solution for the optical properties of small spheroidal particles[198, 199]. It is common to approximate rod nanoantennas as spheroids[174, 176, 200]. While it does not yield the correct result in terms of absolute numbers, it follows the general trends of the optical properties of rod antennas, like that the resonance wavelength scales linearly with the antenna's aspect ratio and the refractive index of the surrounding medium[174, 176]. Still, in Gans theory the resonance wavelength only scales with aspect ratio and not with antenna dimensions[176, 200]. This is because it ignores higher order multipoles, which account for retardation effects in larger antennas. Also, the ratio $\sigma_{scat}/\sigma_{abs}$ is underestimated by Gans theory, where σ_{scat} becomes dominant only for antennas that are twice as large as their rectangular counterpart[201].
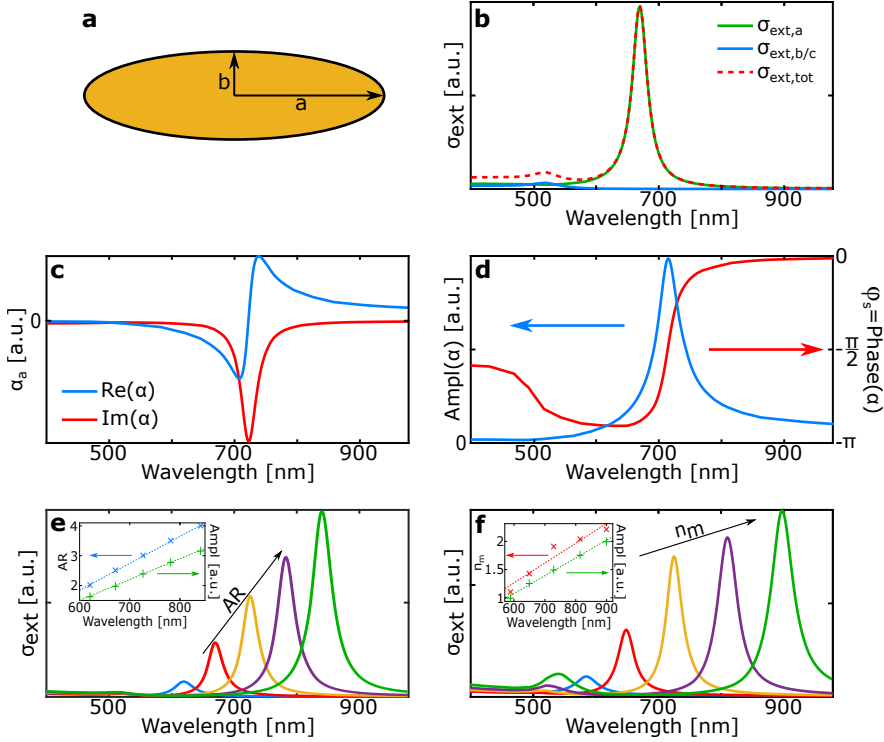
Figure 5.2: *Spheroidal gold nanoantennas.* **(a)** Sketch of prolate spheroid with long axis a and short axis $b = c$. **(b)** σ_{ext} when exciting a spheroid with $n_m = 1.5$ and $AR = 2.5$ along (blue) or across (green) its long axis, and the average over all orientations (dashed red). **(c)** Real (blue) and imaginary (red) part of α_a for $AR = 3$. **(d)** The phase (red) and amplitude (blue) of α_a for $AR = 3$. **(e)** σ_{ext} for $n_m = 1.5$, $AR = 2 - 4$ (step size 0.5, left to right). **(f)** σ_{ext} for $AR = 3$, $n_m = 1 - 2$ (step size 0.25, left to right). $b = 50$ nm for all calculations.

For a prolate spheroidal particle with dimensions $a > b = c$, as the one sketched in figure 5.2a, the polarizability α_i along its three antenna axes is given by[199]

$$\alpha_i = V \frac{\varepsilon_p - \varepsilon_m}{\varepsilon_m + L_i(\varepsilon_p - \varepsilon_m)}, \text{with} \tag{5.1a}$$

$$L_a = \frac{1 - e^2}{e^2}\left(\frac{1}{2e}\ln\left(\frac{1 + e}{1 - e}\right) - 1\right), \tag{5.1b}$$

$$L_b = L_c = (1 - L_a)/2 \tag{5.1c}$$

ε_p and ε_m are the dielectric functions of the particle and its surrounding medium. L_i is a geometrical factor with $L_a + L_b + L_c = 1$, that depends on the eccentricity e of the spheroid with $e^2 = 1 - b^2/a^2$. The volume of a spheroid is $V = \frac{4}{3}\pi abc$.

From equation (5.1a) it can be seen that the polarizability depends on the particle dimensions, especially its eccentricity, as well as the dielectric functions ε_m and ε_p, and that it scales linearly with the antenna volume. Throughout this chapter,

the aspect ratio $AR = a/b$ will be referred to instead of the eccentricity. Also, the refractive index $n = \sqrt{\varepsilon}$ will be used. The propagation of the electromagnetic wave of the focused beams will be taken as $e^{-i(kz-\omega t)}$ throughout this chapter, which affects how certain quantities are expressed. For example, the complex refractive index $\tilde{n}$ reads $\tilde{n} = n - i\kappa$ instead of the more commonly seen $\tilde{n} = n + i\kappa$, with κ the extinction coefficient. The complex refractive index of gold was obtained from tabulated values reported by Johnson and Christy[202]. The surrounding medium is one of the experimental parameters and different values for it will be modeled. Since all surrounding media used in this chapter are transparent, κ_m can be neglected, and $\tilde{n}_m \approx n_m$.

With the expression for the polarizability in equation (5.1), the absorption and scattering cross-section σ_{abs} and σ_{scat} can be calculated as[199]:

$$\sigma_{abs} = -k\operatorname{Im}(\alpha), \tag{5.2a}$$

$$\sigma_{scat} = \frac{k^4}{6\pi}|\alpha|^2. \tag{5.2b}$$

Their sum is the extinction cross-section σ_{ext}, and $k = 2\pi n_m/\lambda_0$ with λ_0 the vacuum wavelength. Since $\alpha \propto V$, $\sigma_{abs} \propto V$ and $\sigma_{scat} \propto V^2$, small particles are stronger absorbers and large particles stronger scatterers. With equations (5.1) and (5.2), the spectral properties of antennas was studied including the polarizability and the effect of n_m and AR. The results are plotted in figure 5.2b-f.

Either the longitudinal or transverse surface plasmon or a combination of the two are excited, depending on the orientation of the antenna with respect to the polarization of the incident beam. This is mirrored in equation (5.1), where $\alpha_a \neq \alpha_b = \alpha_c$. Figure 5.2b plots σ_{ext} of the three components for $n_m = 1.5$ and $AR = 2.5$. $b = 50$ nm has been used for all calculations. When the electric field is aligned along the long axis of the spheroid ($\sigma_{ext,a}$, green), a large absorption peak arises around 680 nm. When one of the short axes is chosen instead ($\sigma_{ext,b/c}$, blue), a smaller peak around 550 nm emerges. Summing up the three spectral components, the spectrum in case of arbitrary antenna orientation was obtained ($\sigma_{ext,tot}$, dashed red). In the following, only the polarization along the long axis is considered corresponding to the longitudinal surface plasmon unless stated otherwise.

Both the real and imaginary part of the complex polarizability α along the long axis were plotted in figure 5.2c for an antenna with $AR = 3$ and $n_m = 1.5$. The real part has a dispersive negative-to-positive shape that crosses zero at resonance. The imaginary part resembles a dip centered around the resonance wavelength, which is $\lambda_{res} = 725$ nm for the chosen parameters. Figure 5.2d shows the amplitude and phase of the polarizability for the same antenna parameters. The amplitude has a maximum at resonance. The phase goes from $-\pi$ to 0, with $-\pi/2$ at resonance and corresponds to the phase change that light obtains when scattering off the

$\varphi_{Gouy}(z_p)=\arctan(z_p/z_R)$
$\varphi_{scat}(z_p)=\arctan(z_p/z_R)+\varphi_s$
$\Delta\varphi(z_p)=-\varphi_s$
Phase at $z=z_p$

$\varphi_{Gouy}(z_D)=\arctan(z_D/z_R)\approx\pi/2$
$\varphi_{scat}(z_D)=\arctan(z_p/z_R)+\varphi_s$
$\Delta\varphi(z_D)=\pi/2-\arctan(z_p/z_R)-\varphi_s$
Phase at $z=z_D$
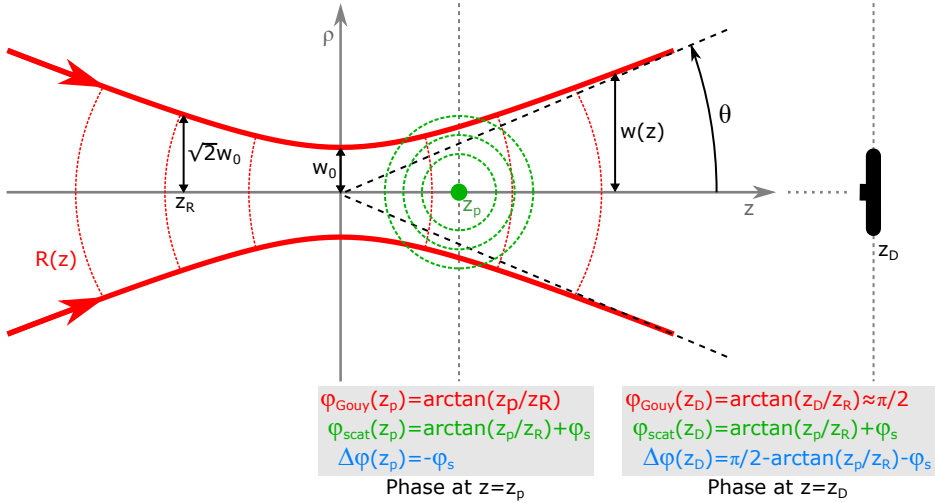
Figure 5.3: *Focused Gaussian beam.* A focused Gaussian beam (red) with radius $w(z)$ and beam waist $w(z=0)=w_0$ traveling along z and detected at z_D. z_R is the Rayleigh range, $R(z)$ the radius of curvature of the beam's wavefront (red dashed) and θ the angular spread of the beam. A particle placed into the beam at position z_p (green dot), scatters light (green dashed). The phases at z_p and z_D are added below.

nanoantenna φ_s which will come back later in the interference discussion. For $\lambda < 500$ nm, the phase rises again up to almost $-\pi/2$ due to interband transitions in gold[199, 202].

The effect of AR and n_m on σ_{ext} are considered next. Figure 5.2e shows the influence of the aspect ratio on the resonance position. Keeping $n_m = 1.5$ fixed, the aspect ratio was changed from 2-4 by increasing the antenna length with a step size of 0.5. As a result, the maximum amplitude of σ_{ext} increases and the resonance shifts towards longer wavelengths. The resonant peaks are spaced equidistantly, i.e. $\lambda_{res} \propto AR$, and the amplitude also increases linearly with the aspect ratio. These two linear dependencies are plotted in the inset of figure 5.2e. Similarly, when using a fixed aspect ratio of $AR = 3$ and varying the n_m from 1-2 with a step size of 0.25, the resonance shifts to higher values for larger refractive indices. This is plotted in figure 5.2f. Again, there is a linear relationship between the position of the resonance wavelength and the variable parameter as seen in the inset of the figure. However, the amplitude of σ_{ext} rises slower for larger n_m. This is in agreement with other simulations using Gans theory[176, 201] and even experimental results[195, 203].

5.1.2   Gaussian beam optics

The other important component for the understanding of light-antenna interactions is the field amplitude and phase of the focused Gaussian beam. Gaussian beams have

a radially symmetric electric field amplitude that follows a Gaussian distribution. An x-polarized collimated beam that travels along the z-axis with $\rho = \sqrt{x^2 + y^2}$ the radial distance from the center of the beam, and w the beam radius at $1/e$ amplitude can be described as

$$\mathbf{E}_G(\rho) = E_0 \exp\left(-\rho^2/w^2\right). \tag{5.3}$$

More factors need to be added to this expression when describing a focused Gaussian beam that travels from negative to positive z and passes through the focus at $z = 0$ including the beam radius $w(z)$ and the radius of curvature of its wavefront $R(z)$. The electric field distribution of the lowest order mode (TEM$_{00}$) of the incident Gaussian beam now reads[204]

$$\mathbf{E}_{inc}(\rho, z) = E_0 \frac{w_0}{w(z)} \exp\left(-\frac{\rho^2}{w^2(z)}\right) \exp\left(-i\left[kz + k\frac{\rho^2}{2R(z)} - \varphi_{Gouy}(z)\right]\right)\hat{\mathbf{e}}_x. \tag{5.4}$$

Due to the excitation with a linearly polarized beam along the long antenna axis $\hat{\mathbf{e}}_x$, only the x-component of the electric field is relevant and the other vectorial components and the not perfectly circular shape in a tight focus can be neglected. This situation is sketched in figure 5.3, where w_0 is the $1/e$ beam waist radius at the focus. The remaining parameters are defined as follows:[204]

$$z_R = \frac{\pi w_0^2 n_m}{\lambda_0} = \frac{1}{2}k w_0^2 \qquad \text{Rayleigh range} \tag{5.5a}$$

$$w(z) = w_0\sqrt{1 + (z/z_R)^2} \qquad \text{beam radius} \tag{5.5b}$$

$$R(z) = z\left(1 + (z_R/z)^2\right) \qquad \text{radius of curvature} \tag{5.5c}$$

$$\varphi_{Gouy}(z) = \arctan(z/z_R) \qquad \text{Gouy phase} \tag{5.5d}$$

$$\theta = \frac{\lambda_0}{\pi w_0 n_m} \qquad \text{beam divergence} \tag{5.5e}$$

The Rayleigh range z_R is the distance from the focus where $w(z) = \sqrt{2}w_0$. The Gouy phase $\varphi_{Gouy}(z)$ shifts by π when going from the negative to the positive far field with $\varphi_{Gouy}(z = 0) = 0$. The beam divergence in the far field ($z \to \infty$) is based on the approximation $\tan(\theta) \approx w(z)/z \approx \theta$.

Using the beam parameters from equation (5.5), the focused Gaussian beam from equation (5.4) can be rewritten in a more compact way as

$$\mathbf{E}_{inc}(\rho, z) = E_0 \frac{\exp(-ikz)}{1 - iz/z_R} \exp\left(-\frac{\rho^2/w_0^2}{1 - iz/z_R}\right)\hat{\mathbf{e}}_x. \tag{5.6}$$

Here, the Gouy phase entered the denominator of the first part of the equation through the relationship $\exp(i\arctan(x)) = (1 + ix)/\sqrt{1 + x^2}$. The beam intensity along the z-axis is $I_{inc}(\rho = 0) = |\mathbf{E}_{inc}|^2 = E_0^2/(1 + z^2/z_R^2)^{-1}$, and follows a Lorentzian shape along the z-axis. It determines the beam intensity at the position where it interacts with the antenna and will be seen back throughout the chapter.

5.1.3 Combining it all

Whenever an antenna is placed into the beam at axial position z_p (green sphere figure 5.3), it can both absorb and scatter light. The difference in power of the incident beam reaching the detector with or without the antenna present is given by

$$\frac{\Delta P}{P} = \frac{P_{inc+ant} - P_{inc}}{P_{inc}}. \tag{5.7}$$

As already discussed in chapter 1 in the context of Fourier transform spectroscopy, the interference signal depends on the phase difference $\Delta\varphi$, in this case between the incident and scattered light at the detector in the far field at $z = z_D$. The two relevant phases to consider here are the Gouy phase φ_{Gouy} for the incident and the scattering phase of the antenna φ_s so that

$$\Delta\varphi(z) = \varphi_{Gouy}(z) - \varphi_{scat}(z). \tag{5.8}$$

$\Delta P/P > 0$ for constructive interference ($\Delta\varphi < \pi/2$), and $\Delta P/P < 0$ for destructive interference ($\Delta\varphi > \pi/2$). The Gouy phase of the incident light evolves through the entire focus, whereas the scattering phase does not. To understand this better, the phases at antenna position $z = z_p$ and detector position $z = z_D$ are both indicated in figure 5.3. At $z = z_p$, the incident light has a Gouy phase of $\varphi_{Gouy}(z_p) = \arctan(z_p/z_R)$. The scattered light obtains an additional phase φ_s with respect to it such that $\varphi_{scat}(z_p) = \varphi_{Gouy}(z_p) + \varphi_s$ and $\Delta\varphi(z_p) = -\varphi_s$. At the detector position $z_D \to \infty$, the Gouy phase will have evolved further to $\varphi_{Gouy}(z_D) = \arctan(z_D/z_R) \approx \pi/2$, while the scattered phase will have remained unchanged: $\varphi_{scat}(z_D) = \varphi_{scat}(z_p)$. As a consequence,

$$\Delta\varphi(z_D) = \pi/2 - \arctan(z_p/z_R) - \varphi_s. \tag{5.9}$$

The detected phase difference therefore depends on both z_p and φ_s. z_p relates to the antenna position in the beam, while φ_s depends on the excitation wavelength with respect to the plasmon resonance, making this a two dimensional problem.

φ_s is given by the phase of the polarizability, which had been sketched in figure 5.2d. It depends on the plasmon resonance and follows the shape of an inverse tangent as a function of wavelength. Its values range from $-\pi$ for short to 0 for long wavelengths, passing through the point of inflection with value $\varphi_s = -\pi/2$ at resonance.

Using equation (5.9), the light scattering off a resonant antenna ($\varphi_s = -\pi/2$) interferes destructively for all z_p. In the focus ($z_p = 0$) the two fields are exactly out of phase which leads to a minimum in detected signal: $\Delta\varphi(z_p = 0) = \pi$. This leads to $\Delta P/P$ being negative throughout z_p with a dip symmetric around $z_p = 0$. For wavelengths below the resonance wavelength, φ_s asymptotically moves to $-\pi$ where

$\Delta\varphi(z_p < 0) < \pi/2$ and $\Delta\varphi(z_p > 0) > \pi/2$. This corresponds to constructive interference for $z_p < 0$ and destructive interference for $z_p > 0$. For longer wavelength, $\varphi_s = 0$ and the opposite trend emerges with a negative-to-positive signal. The results still need to be weighted by the beam intensity, which decreases the further away from the focus position the antenna is placed. In addition, the contribution due to absorption has not been taken into account. For this, the polarizability from equation (5.1) will be combined with the Gaussian beam defined in equation (5.6).

Antennas smaller than the excitation wavelength can be approximated as dipole scatterers even though formalisms including higher order terms exist for spheroidal particles in a focused Gaussian beam[205–207]. For a dipole at $z = z_p$ with dipole moment $\mathbf{p} = \varepsilon_m \alpha \mathbf{E}_G(z_p)$ the scattered field in the far field in spherical coordinates is[199]

$$\mathbf{E}_{scat} = \frac{e^{-ikr}}{-ikr} \frac{ik^3}{4\pi\varepsilon_m} \hat{\mathbf{e}}_r \times (\hat{\mathbf{e}}_r \times \mathbf{p}). \tag{5.10}$$

In the far field at detector position, and under the paraxial approximation $\rho \to 0$, $r \approx z_D \to \infty$ this can be simplified to[186]

$$\mathbf{E}_{scat}(z_p, z_D) \approx E_0 \frac{\alpha k^2}{4\pi z_D} \frac{\exp(-ikz_D)}{1 - iz_p/z_R} \hat{\mathbf{e}}_x. \tag{5.11}$$

The incident field from equation (5.6) at the detector position is approximated in the same way as

$$\mathbf{E}_{inc}(z_D) \approx E_0 i \frac{z_R}{z_D} \exp(-ikz_D) \hat{\mathbf{e}}_x. \tag{5.12}$$

The prefactor i is due to the Gouy phase, since $\varphi_{Gouy}(z) \to \pi/2$ for large z, and $e^{i\pi/2} = i$.

The relative intensity difference because of the interference between the incident and scattered light can be described as the ratio of the beam powers

$$\frac{\Delta P}{P} = \frac{|\mathbf{E}_{inc} + \mathbf{E}_{scat}|^2 - |\mathbf{E}_{inc}|^2}{|\mathbf{E}_{inc}|^2} = \frac{2\operatorname{Re}(\mathbf{E}_{inc}^* \mathbf{E}_{scat}) + |\mathbf{E}_{scat}|^2}{|\mathbf{E}_{inc}|^2}. \tag{5.13}$$

Using equation (5.12) and equation (5.11) for $\mathbf{E}_{inc}$ and $\mathbf{E}_{scat}$, this can be rewritten as

$$\frac{\Delta P}{P} = \underbrace{\frac{k}{\pi w_0^2} \frac{\operatorname{Im}(\alpha) + z_p/z_R \operatorname{Re}(\alpha)}{1 + (z_p/z_R)^2}}_{\Delta P/P_1} + \underbrace{\frac{k^4}{16\pi^2 z_R^2} \frac{|\alpha|^2}{1 + (z_p/z_R)^2}}_{\Delta P/P_2}. \tag{5.14}$$

$\Delta P/P_1$ stems from the $2\operatorname{Re}(\mathbf{E}_{inc}^* \mathbf{E}_{scat})$ term and resembles σ_{abs} from equation (5.2a) with an additional $z_p/z_R \operatorname{Re}(\alpha)$ component. This addition accounts for the position dependent Gouy phase. $\Delta P/P_2$ comes from $|\mathbf{E}_{scat}|^2$ which resembles σ_{scat} from
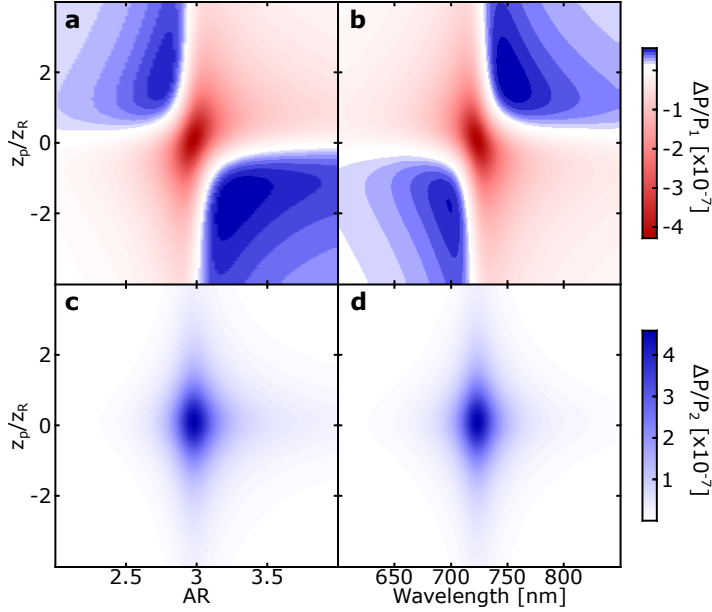
Figure 5.4: $\Delta P/P$ *models.* **(a)** $\Delta P/P_1$ for different *AR* at 725 nm excitation wavelength and for $n_m = 1.5$. **(b)** $\Delta P/P_2$. **(c-d)** show the same model, but for a variable excitation wavelength and *AR* fixed at 3.

equation (5.2b). This term usually gets dropped in calculations, since small particles do not scatter significantly and $|\mathbf{E}_{scat}|^2 \ll |\mathbf{E}_{inc}|^2$[185, 186, 188].

With the polarization from equation (5.1), the effect of *AR* and z_p on $\Delta P/P$ can be calculated. Figure 5.4a shows the results for $\Delta P/P_1$ for a surrounding medium with $n_m = 1.5$ and where the incident light has wavelength $\lambda = 725$ nm, the resonance wavelength for $AR = 3$. At resonance, a large negative signal emerges that is symmetric around $z_p = 0$. Antennas with smaller aspect ratios exhibit a dispersive negative-to-positive signal, and antennas with a larger aspect ratio a positive-to-negative trend. All of this is in line with the discussion of the Gouy phase at the beginning of this section and demonstrates the importance of both the antenna position and resonance condition when considering $\Delta P/P$. For example, non-resonant antennas give $\Delta P/P_1 \approx 0$ in the focus. As a side note, because $\Delta P/P_1 \propto \alpha \propto V$, the dispersive signal is stronger for the antennas with larger *AR*.

$\Delta P/P_2$ is sketched separately in figure 5.4b. It gives a positive signal centered around $z_p = 0$ and the resonant antenna length. Since $\Delta P/P_2 \propto \alpha^2 \propto V^2$, it becomes more important for larger antennas. Since Gans theory yields the incorrect $\sigma_{scat}/\sigma_{abs}$ ratios[201], the relative contribution of $\Delta P/P_1$ and $\Delta P/P_2$ from the model will be differ from those achieved in the experiment, while the shape of the individual components is correct.

Figure 5.4c and d present the same results for an antenna of $AR = 3$ that has been excited at different wavelengths. A large negative $\Delta P/P_1$ signal at resonant wavelength 725 nm is again accompanied by a dispersive signal for longer and shorter wavelengths. Figure 5.4a and c are almost mirror images of each other. That is because going to higher excitation wavelengths is very similar to reducing the resonance wavelength by decreasing AR. However, the antenna dimensions remain constant in the latter case, which leads to the observed similarity between the signal strength above and below the resonance wavelength.

One important conclusion from the single beam model is that $\Delta P/P$ measurements in a setup with a tight focus the Gouy phase needs to be included. This was summarized in figure 5.4 where $\Delta P/P$ depended strongly on both λ_{res} and z_p. For resonant antennas, the strongest signal is achieved in the focus, but for non-resonant antennas, it can be found at about $\pm 2\,z_p/z_R$ distance from the focus. Depending on whether the excitation occurs above or below the resonant wavelength, the sign of the dispersive $\Delta P/P_1$ signal flips.

5.2 Photothermal detection

The second objective of this chapter is to understand how the heating of the surrounding medium induced by a modulated pump beam changes the detected signal. Both pump and probe beam are cw lasers so that the electron-electron and electron-phonon scattering effects that happen on a timescale of up to ~1 ps can be safely ignored[58, 60]. Instead, only the phonon-phonon scattering that heats the surrounding medium on longer time scales needs to be considered here.

Due to the temperature increase in the medium, a refractive index gradient is created around the antenna, called the thermal lens. Two different effects are induced by the change of refractive index that are simultaneously detected by the probe beam. First, the scattering of the probe beam off the thermal lens will be considered. Second, the change in $\Delta P/P$ induced by the refractive index change is studied. A formalism for both effects will be derived in the following, starting with an introduction into the relevant thermodynamics.

5.2.1 Heating the nanoenvironment

The heat radiated from the antenna increases the temperature at the antenna surface homogeneously[208, 209]. From the surface, the heat diffuses outward, creating a temperature gradient around the antenna as sketched in figure 5.6a in red. The efficiency of the temperature increase is given by the specific heat C_p. The larger its value, the more energy is required to heat the medium by the same amount. The temperature increase affects n_m. This is expressed by the thermo-optical coefficient $\frac{dn}{dT}$. For most media it is negative, and the refractive index decreases upon heating.

The temperature gradient also depends on the efficiency with which heat spreads through the medium, given by the thermal conductivity κ. The larger κ, the further the heat spreads. The temperature gradient at a distance r from a point source that is modulated with a heating beam with frequency Ω as $(1 + \cos(\Omega t))$ can be expressed as[190, 191]

$$\Delta T(\Omega, r, t) = \frac{P_{heat}}{4\pi\kappa r}\left(1 + \exp\left(-\frac{r}{r_{th}}\right)\cos\left(\Omega t - \frac{r}{r_{th}}\right)\right). \tag{5.15}$$

$P_{heat} = \sigma_{abs}P_h/A_h$ is the heat dissipated by the antenna due to the pump beam with power P_h. P_h/A_h is the power density of a pump beam with area $A_h = 2\pi w_h^2(z_p)$. The subscript h was added to all parameters regarding the pump beam to differentiate it from the probe beam parameters which do not carry any subscript. Finally, r_{th} is the thermal radius, given by the characteristic $1/e$ length of heat diffusion at frequency Ω as

$$r_{th}(\Omega) = \sqrt{\frac{2\kappa}{\Omega C_p}}. \tag{5.16}$$

Heat takes a finite amount of time to dissipate into the medium. This is reflected in the cosine of equation (5.15), which includes the retardation of the heat dissipation at a certain distance from the heat source by adding the term r/r_{th}. If the thermal radius $r_{th}(\Omega)$ is much larger than the beam waist radius $w(z_p) \sim r$, then the expression for the temperature can be simplified to

$$\Delta T(\Omega, r, t) \approx \frac{P}{4\pi\kappa r}(1 + \cos(\Omega t)), \tag{5.17}$$

which corresponds to a long-ranged $1/r$ profile. It implies that any temperature change at the heat source is immediately felt throughout the entire medium on the time scale of the experiment. That is why it is considered the steady-state regime. For larger Ω, the temperature change in the surrounding medium is lagging behind the heat modulation in accordance with equation (5.15). This results in an out-of-phase component for detection with a lock-in amplifier.

The refractive index change directly relates to the temperature change through the thermo-optical coefficient $\frac{dn}{dT}$ as

$$\Delta n(\Omega, r, t) = \frac{dn}{dT}\Delta T(\Omega, r, t). \tag{5.18}$$

Table 5.1 lists the thermodynamic parameters of the different media used in this chapter together with the calculated values for r_{th} at $\Omega = 1\,\text{MHz}$. The positive $\frac{dn}{dT}$ of glass and ITO leads to an increase in refractive index upon heating, while it decreases for water, ethanol and immersion oil is due to the negative $\frac{dn}{dT}$.
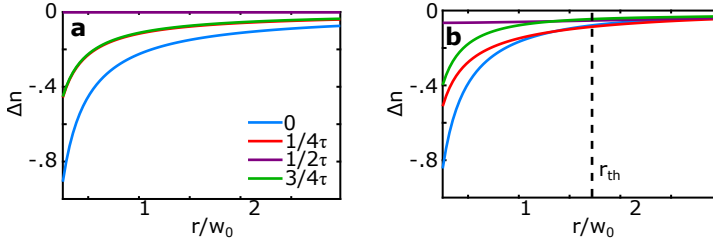
Figure 5.5: *Steady state vs fast modulation of Δn.* Simulation of Δn at different phases of the pump oscillation τ in water for **(a)** $\Omega = 1\,\text{kHz}$ (steady state), and **(b)** $\Omega = 1\,\text{MHz}$. Model parameters: $\lambda_h = 625\,\text{nm}$, $\lambda = 725\,\text{nm}$, w_0, $w_{0,h} = 300\,\text{nm}$, $P_h = 1\,\mu\text{W}$, $a = 150\,\text{nm}$, $b = 50\,\text{nm}$.

To demonstrate the effect of Ω on the refractive index gradient, figure 5.5 shows the Δn calculated with equations (5.15) and (5.18) at modulation frequencies $\Omega_{slow} = 1\,\text{kHz}$ and $\Omega_{fast} = 1\,\text{MHz}$ for water as a surrounding medium. All additional parameters are given in the figure description and will be used for all subsequent model figures as well, unless stated otherwise. Using $\Omega = 2\pi/\tau$ with τ the oscillation period, Δn was calculated for the modulation maximum ($t = 0/\tau$), modulation minimum ($t = \frac{1}{2}\tau$) as well as the downward and upward point of inflection ($t = \frac{1}{4}\tau$, $\frac{3}{4}\tau$). Figure 5.5a shows Δn for Ω_{slow} for which $r_{th} = 57w_0$. The largest refractive index profile is reached for the modulation maximum (blue), zero for the modulation minimum (purple) and the same profile for the downward and upward points of inflection (red and green). Figure 5.5b shows Δn for Ω_{fast} for which $r_{th} = 1.8w_0$. A slightly smaller Δn is obtained for the modulation maximum while the modulation minimum does not quite reach zero. For the points of inflection, the refractive index change is lagging behind such that Δn has a larger magnitude for $t = \frac{1}{4}\tau$ than $t = \frac{3}{4}\tau$. For distances beyond r_{th}, the modulation contrast almost disappears completely. An important consequence of using high modulation frequencies is a loss in signal strength compared to the steady-state regime.

	n	$\frac{dn}{dT}$	$\mathbf{C_p}$	κ	$\mathbf{r_{th}}$ (1 MHz)
		$[\text{K}^{-1}]$	$[\text{Jm}^{-3}\text{K}^{-1}]$	$[\text{W/m/K}]$	$[\text{m}]$
Glass	1.51	2.4×10^{-6}	2.1×10^6	1.19	1.1×10^{-6}
ITO	1.80	2.2×10^{-4}	2.6×10^6	5	2.0×10^{-6}
Air	1.00	-8.8×10^{-7}	1.2×10^3	0.026	6.6×10^{-6}
Water	1.33	-9.1×10^{-5}	4.2×10^6	0.6	5.4×10^{-7}
Ethanol	1.36	-4.0×10^{-4}	1.9×10^6	0.17	4.2×10^{-7}
Oil	1.52	-3.8×10^{-4}	-	-	-

Table 5.1: *Photothermal properties of different media.* Glass (BK7): from [210]. ITO: n from [211], $\frac{dn}{dT}$ from [212], C_p approximated by In_2O_3 value from [213], κ from [213]. Air, water and ethanol from[214]. Immersion oil: n from manufacturer, $\frac{dn}{dT}$ from comparable product from a different manufacturer[215]. r_{th} via equation (5.16) using $\Omega = 1\,\text{MHz}$.
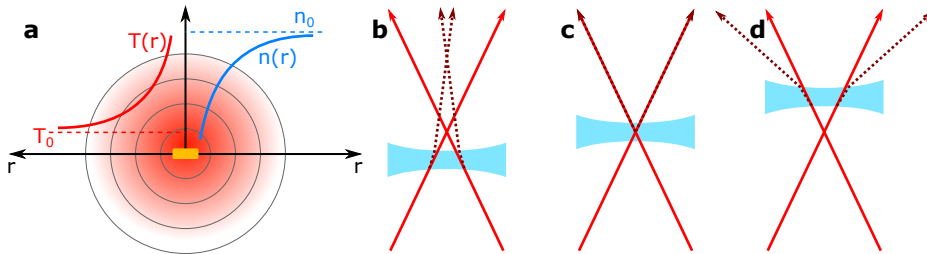
Figure 5.6: *Photothermal lens.* **(a)** Sketch of the photothermal effect. The temperature increase $\Delta T(r)$ is largest close to the center, which leads to the smallest n. **(b-d)** The incident light (red) scattering off the photothermal lens before, in or after the focus (dark red, dashed).

Independent of $r_{th}(\Omega)$ and the sign of $\frac{dn}{dT}$, the refractive index gradient $\Delta n(r)$ and the change in antenna polarizability because of it will contribute to the change in detected $\Delta P/P$ signal. They will be described in more detail in the following sections.

5.2.2 The thermal lens effect

Many theoretical descriptions exist for light scattering of light off the refractive index gradient formed around the nanoantenna upon heating. They include the equivalent dipole model[49, 216], photothermal heterodyne detection[196, 217], generalized Lorenz-Mie theory[170], Fresnel diffraction[194], and ray transfer matrix analysis[218]. Each of these descriptions comes with its own benefits and limitations.

Probably the most intuitive description is the ray transfer matrix formalism, where the three dimensional refractive index gradient gets approximated as a two dimensional lens[218]. In figure 5.6b-d the lensing effect on the incident beam (red, solid) for an antenna placed before, into and behind the focus are sketched for an $\frac{dn}{dT} < 0$ medium together with its corresponding divergent lens. When the antenna is placed before the focus ($z_p < 0$), the incident beam becomes narrower (dark red dashed). The narrower beam waist after the beam waist results in an increased power density and consequentially a larger signal at the detector. When the antenna is placed into the focus, the beam passes through the medium unaffected by the thermal lens. Behind the focus, it diverges the incident beam and the light reaching the detector decreases. Combining the three scenarios, a positive-to-negative contrast is observed at the detector when scanning the antenna through the focus. For $\frac{dn}{dT} > 0$ media, a converging lens would lead to the observation of the opposite signal trend. The actual derivation using the ray transfer matrix formalism now follows.

Assuming that the detector size is smaller than the beam area, the intensity reaching the detector is inversely proportional to the beam area at the detector: $I \propto 1/w^2(z_D)$. Ray transfer matrices are a mathematical description of how an optical ray at dis-

tance x from and at angle θ with the optical axis propagates through different optical elements. Each optical elements are represented by a $2x2$ matrix. The two relevant matrices here are the matrix for propagation in free space $\mathbf{M}_d$ which requires the parameter d for the distance traveled, and the matrix for a thin lens $\mathbf{M}_f$ with $f < 0$ the focal length for a diverging lens. In concrete,

$$\begin{pmatrix} x_2 \\ \theta_2 \end{pmatrix} = \mathbf{M} \begin{pmatrix} x_1 \\ \theta_1 \end{pmatrix}, \quad \text{with} \quad \mathbf{M}_d = \begin{pmatrix} 1 & d \\ 0 & 1 \end{pmatrix}, \quad \mathbf{M}_f = \begin{pmatrix} 1 & 0 \\ -\frac{1}{f} & 1 \end{pmatrix}. \tag{5.19}$$

The overall matrix with and without the thermal lens is then given by $\mathbf{M}_{TL} = \mathbf{M}_d \mathbf{M}_f$ respectively $\mathbf{M} = \mathbf{M}_d$. The distance of the ray from the optical axis, $x_2 = w(z_D)$, can now be calculated for the two cases as

$$x_2 = x_1 + d\theta_1, \tag{5.20a}$$

$$x_{2,TL} = \left(1 - \frac{d}{f}\right) x_1 + d\theta_1. \tag{5.20b}$$

For a thermal lens formed around an antenna at z_p, $x_1 = w(z_p)$ and $\tan(\theta_1) \approx w(z_p)/z_p \approx \theta_1$. Using $z_D \gg z_p$, $d = z_D + z_p \approx z_D$, and further assuming that $d \gg f \gg z_{R,p}$ and $z_p > z_R$, equation (5.20) can be rewritten to find the beam intensity reaching the detector as

$$I_0 \propto \frac{1}{w^2(z_D)} \approx \frac{1}{w_0^2} \frac{z_R^2}{z_D^2}, \tag{5.21a}$$

$$I_{TL} \propto \frac{1}{w_{TL}^2(z_D)} \approx \frac{1}{w_0^2} \frac{z_R^2}{z_D^2} \left[1 + \frac{2z_p}{f}\right]. \tag{5.21b}$$

The same expression for I_0 would have been reached for $w(z)$ from equation (5.5a) as a starting point. With the two intensities known, the photothermal contrast Φ_{TL} because of the thermal lens is given by

$$\Phi_{TL}(z_p) = \frac{I_{TL} - I_0}{I_0} = \frac{2z_p}{f}. \tag{5.22}$$

The effective focal length f_{eff} for spherical particles with radius $R < \lambda$ in the steady-state regime can be derived as[218]

$$f_{eff}(z_p) \approx \frac{n_0}{\Delta n} \frac{w_0^2}{4R} \left[1 + \left(\frac{z_p}{z_R}\right)^2\right]. \tag{5.23}$$

For $r_{th} > w_0$, as is the case in the presented experiments, the $1/r$ temperature decay of the steady-state regime is assumed to not have a large quantitative effect on the effective focal length. From equation (5.23) it can be seen that for $\frac{dn}{dT} < 0$ media,

$f_{eff} < 0$ describes a diverging lens as anticipated. Inserting this negative focal length into equation (5.22), $\Phi_{TL}(z_p < 0) > 0$ and $\Phi_{TL}(z_p > 0) < 0$ which results in the positive-to-negative signal trend discussed earlier.

Combining Φ_{TL} from equation (5.22) with equations (5.5), (5.18) and (5.23), one finally obtains

$$\Phi_{TL} = \frac{P_h \sigma_{abs} \frac{dn}{dT} z_p}{n_0 w_0^2 w_{0,h}^2 \pi^2 \kappa} \frac{R}{r} \left[1 + \left(\frac{z_p}{z_R}\right)^2\right]^{-1} \left[1 + \left(\frac{z_p}{z_{R,h}}\right)^2\right]^{-1}$$

$$\times \left(1 + \exp\left(-\frac{r}{r_{th}}\right) \cos\left(\Omega t - \frac{r}{r_{th}}\right)\right). \quad (5.24)$$

The two expressions with the square brackets reflect the beam intensity at the particle position of the probe respectively pump beam. The better the overlap between the antenna and the pump beam focus, the more efficient the heating. The better the overlap with the probe beam, the more light is scattered. When using this equation for simulations, the antenna radius is approximated by $R = a/2$ and the effective radius of the focused beam at the antenna position by $r = w(z_p)/\sqrt{2}$[218]. σ_{abs} is determined using equation (5.2a).

The modulated signal is detected with a lock-in amplifier, which is phase sensitive. Therefore, Φ_{TL} has to be separated into an in-phase ($\Phi_{TL,\cos}$) and an out-of-phase ($\Phi_{TL,\sin}$) component that are expressed mathematically by the integration over one oscillation of the modulation $\tau = 2\pi/\Omega$. The signal is measured separately at the two lock-in amplifier channels as $\Phi_{TL} = \sqrt{\Phi_{TL,\sin}^2 + \Phi_{TL,\cos}^2}$ with

$$\Phi_{TL,\cos} = \frac{2}{\tau} \int_0^\tau \cos(\Omega t)\Phi_{TL}dt, \quad (5.25a)$$

$$\Phi_{TL,\sin} = \frac{2}{\tau} \int_0^\tau \sin(\Omega t)\Phi_{TL}dt. \quad (5.25b)$$

The relative strengths of the in-phase and out-of-phase components depend on the photothermal properties of the surrounding medium and the modulation frequency. Figure 5.7 simulates $\Phi_{TL}(z_p)$ for antennas resonant with the heating beam at $\lambda_h = 625$ nm using Ω_{fast}. Figure 5.7a shows for which AR each medium is resonant with the heating beam. It scales from small to large AR, for smaller n_m. Figure 5.7b-f shows Φ_{TL} at the resonant AR for each of the five media. The total signal Φ_{TL} (blue) follows a negative-to-positive dispersive trend for the $\frac{dn}{dT} > 0$ media, and the opposite one for the $\frac{dn}{dT} < 0$ media, even though its strength shows large variations. According to equation (5.24), the signal strength scales as $\frac{dn}{dT}/\kappa$. For example, for ethanol this term is an order of magnitude larger than for water, which is reflected in their Φ_{TL} signal.
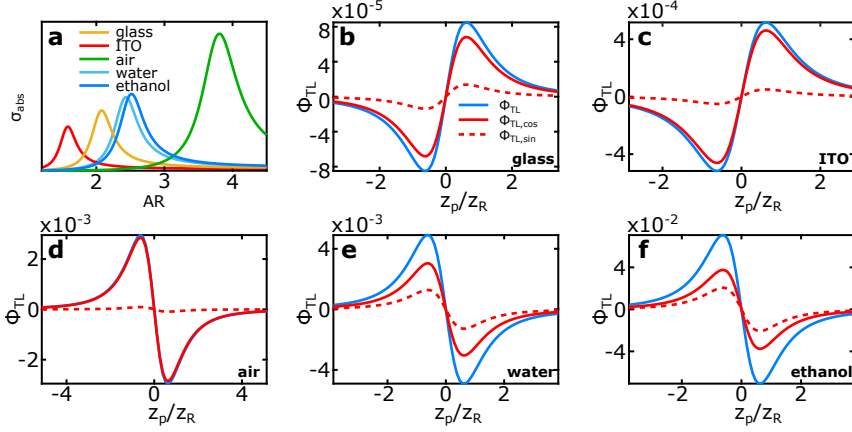
Figure 5.7: $\Phi_{TL,\cos}$ *and* $\Phi_{TL,\sin}$ *for different media.* **(a)** σ_{abs} for antennas surrounded by different media. $\Phi_{TL,\cos}$, $\Phi_{TL,\sin}$ and Φ_{TL} at $\Omega = 1\,\text{MHz}$ and resonant *AR* for **(b)** glass $(\sim 10^{-4})$, **(c)** ITO $(\sim 10^{-4})$, **(d)** air $(\sim 10^{-3})$, **(e)** water $(\sim 10^{-3})$, and **(f)** ethanol $(\sim 10^{-2})$. Model parameters in figure 5.5.

$\Phi_{TL,\cos}$ (red solid) and $\Phi_{TL,\sin}$ (red dashed) exactly follow the same signal trend as Φ_{TL} for all media, though with different ratios related to r_{th}. For air, which has the largest r_{th} at 6.6 µm, $\Phi_{TL,\sin}/\Phi_{TL}$ is almost zero while for ethanol, which has the smallest r_{th} at 420 nm, the out-of-phase component contributes almost 30 % to the signal. When choosing a lower modulation frequency, the steady state regime is eventually reached for all media and $\Phi_{TL,\cos}$ approaches Φ_{TL}.

Figure 5.8a relates the $\Phi_{TL,\cos}$ to z_p and *AR*, again using the values for water and Ω_{fast}. Here, *AR* entered the calculations through σ_{abs}. The maximum amplitude of $\Phi_{TL,\cos}$ is one order of magnitude larger for the $\Phi_{TL,\sin}$ component consistent with figure 5.7e. Regardless of *AR*, the signal shows a positive-to-negative dispersive signal when scanning through z_p for this $\frac{dn}{dT} < 0$ medium with the oscillation maximum at $\pm 0.5\,z_p/z_R$. The thermal lens effect does not depend on the Gouy phase which cancels out[194], but only on the tightness of the focus through z_R.

5.2.3 Change in polarizability

The change in n_m upon heating alters the polarizability of the antennas through equation (5.1). Then, the modulated change in polarizability is given by the difference in $\Delta P/P$ with the pump beam on and off as

$$\Phi_\alpha = \frac{\Delta P}{P}(n_{m,pump\ on}) - \frac{\Delta P}{P}(n_{m,pump\ off}). \tag{5.26}$$

Just as $\Delta P/P$ was separated into two components in equation (5.14), the Φ_α contribution due to $\Delta P/P_1$ and $\Delta P/P_2$ will be looked at separately as $\Phi_{\alpha i} = \Delta P/P_{i,on} - \Delta P/P_{i,off}$ with $\Phi_\alpha = \Phi_{\alpha 1} + \Phi_{\alpha 2}$.
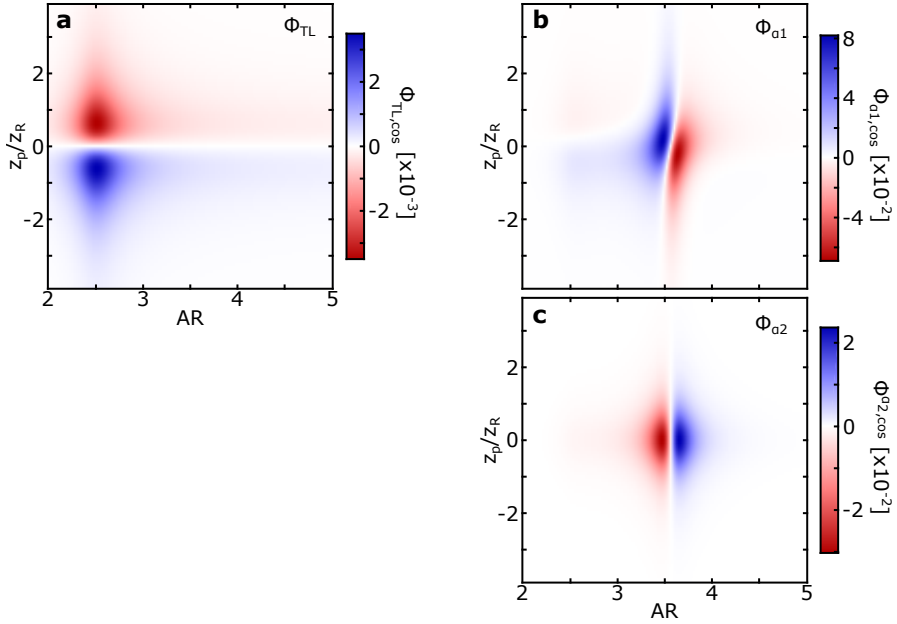
Figure 5.8: Φ_α *plotted via* Δn *(t).* Simulation for water at $\Omega = 1\,\mathrm{MHz}$ of **(a)** $\Phi_{TL,\mathrm{cos}}$, **(b)** $\Phi_{\alpha1,\mathrm{cos}}$ and **(c)** $\Phi_{\alpha2,\mathrm{cos}}$. Model parameters in figure 5.5.

For $\frac{dn}{dT} < 0$ media, $\Delta n < 0$ and the plasmon resonance shifts to lower wavelengths. That is comparable to taking the difference between two $\Delta P/P$ measurements with different antenna lengths, where the shorter AR represents the scenario with the pump beam on. When looking at the $\Delta P/P_1$ model plotted in figure 5.4a, this would result in a positive-to-negative dispersive $\Phi_{\alpha1}$ signal for antennas with a small AR, and a negative-to-positive dispersive $\Phi_{\alpha1}$ signal for antennas with a large AR. Around the resonant AR, transitions between several different shapes occur. $\Delta P/P_2$ from figure 5.4b yields a negative $\Phi_{\alpha2}$ for antennas below resonance, and a positive one for antennas with an AR that is larger than the resonant antenna, both centered around $z_p = 0$. This argumentation does not take into account the efficiency with the surrounding medium is heated, which will be strongest for antennas resonant with the pump beam that were placed into the focus.

For the actual calculations, the polarizability from equation (5.1) is made time-dependent by introducing $\Delta n(\Omega, r, t)$ from equations (5.15) and (5.18) as $\epsilon_m = (n_m + \Delta n)^2$ into it. Using this polarizability in $\Delta P/P$ from equation (5.14), the in-phase and out-of-phase components can be calculated by integrating over one oscillation period of the modulation similar to Φ_{TL} in equation (5.25). The results for $\Phi_{\alpha,\mathrm{cos}}$ are plotted in figure 5.8b and c. They are about one order of magnitude larger than $\Phi_{\alpha,\mathrm{sin}}$. The strongest signal for both $\Phi_{\alpha1}$ and $\Phi_{\alpha2}$ is found around the probe beam resonance (AR 3.5), instead of the pump beam resonance (AR 2.5), where the heating and thus Δn is strongest. This is because the polarizability varies a lot

around the plasmon resonance, but hardly at all at its tails. Therefore, the larger change in $\Delta P/P$ around probe resonance far outweighs small changes in $\Delta P/P$ around the pump beam resonance despite the stronger Δn.

In an actual experiment, a superposition of Φ_{TL} and Φ_α is measured and the overall photothermal signal is given by

$$\Phi = \Phi_{TL} + \Phi_\alpha.$$

The relative strength of the individual components Φ_{TL}, $\Phi_{\alpha 1}$, and $\Phi_{\alpha 2}$ depends strongly on the antenna's volume, overlap of the pump and probe beam with σ_{abs} and σ_{scat} of the antenna, and the modulation frequency, among other parameters. While the simplified spheroidal model used to describe the polarizability of nano-antennas is sufficient to show the signal trends of the three individual components, their relative signal strengths would not reflect those of the rectangular antennas used in the actual experiment. This is partially due to the difference in cross-sections and refractive index change between model and actual system[201]. Still, the model presented here is apt to describe the signal trends, which lends itself to a qualitative interpretation of the data.

Having modeled both the static interaction of an antenna with a single focused beam as presented in figure 5.4, and the time-dependent signal due to a modulated pump beam heating the surrounding medium as shown in figure 5.8, it is now time to compare the simulations to actual data.

5.3 Setup

The stimulated emission pump-probe setup from chapter 4 only needed some minor adjustments to be able to measure both the single beam contrast $\Delta P/P$ and the photothermal response Φ. Two 885 nm long-pass filters (HG885LP, Chroma) replaced the band-pass filters in the APD detection path to detect the antenna luminescence due to the probe laser at 850 nm. The same high NA oil immersion objective (1.4NA, 60x, Nikon Plan Apo λ) was used to focus light onto the sample. However, the transmitted signal was collected with a 0.5 NA air objective (EC Plan-Neofluar 20x/0.5, Zeiss), which occasionally had been exchanged by a 0.95 NA air objective (Achroplan 63x/0.95, Zeiss) for detecting wider angles. The monitor channel of the balanced photodiode was used to measure the change in transmission $\Delta P/P$. The balanced RF output of the balanced photodiode was sent to the lock-in amplifier to obtain Φ. Moderate pump and probe powers of around 50-100 µW in front of the microscope were used throughout the experiment as to not damage the antennas ($\sim$10 kW/cm² at sample).
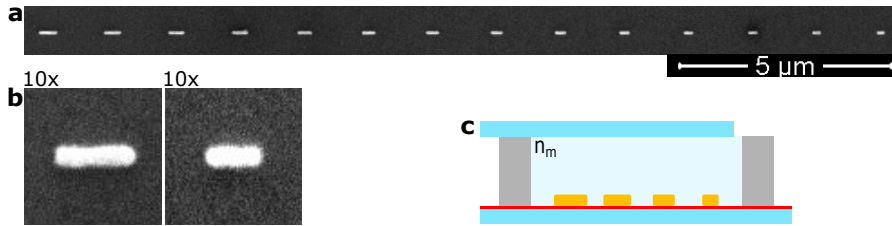
Figure 5.9: *Gold nanoantennas.* **(a)** Scanning electron microscope image of row of antennas of decreasing length on a glass coverslip. **(b)** 10x zoom of a 220 nm and 130 nm long antenna. **(c)** Sketch of antenna sample. The antennas (gold) are on top of an ITO layer (red). A well (gray) is created around the antennas, enclosing a medium with refractive index n_m by a second coverslip on top.

5.3.1 Sample preparation

The sample consisted of an array of gold nanoantennas with a width and height of 50 nm and with a lengths that varied from 60-220 nm in steps of 10 nm. The antennas were fabricated using electron-beam lithography. A 10 nm layer of indium tin oxide (ITO) was evaporated onto a cleaned coverslip, which was subsequently placed onto a hotplate at 350 °C for 6 min to oxidize the ITO. 150 μM of PMMA (polymethyl methacrylate, resist AR-P 671.04) was spincoated on top of the ITO layer at 8000 rpm for 60 s, resulting in a layer thickness of approximately 180 nm. After the electron-beam exposure, the sample was developed in a solution of methyl isobutyl ketone (MIBK) and isopropyl alcohol (IPA) with 1:3 MIBK:IPA ratio for 45 s, followed by another 45 s in only IPA. Subsequently, a 50 nm layer of gold was evaporated on top of the sample, before finally doing a 2-3 h liftoff in acetone, which left only the nanostructures on top of the ITO layer. Figure 5.9a shows a scanning electron microscope (SEM) image of a row of antennas of varying lengths fabricated this way. The 10x zoomed in images in figure 5.9b of a 220 nm and 130 nm long antenna show that the antennas do not form a perfect rectangle, but have curved edges. The shape of the antenna ends affects the resonance condition and extinction efficiency, but not the qualitative scattering behavior that is studied in this chapter[219].

Figure 5.9c shows a sketch of the finished sample. The ITO layer (red) onto which antennas of various lengths (gold) had been placed covers the bottom coverslip (blue). The antennas were surrounded by media of different refractive indices n_m, which were prevented from spreading by a silicone film (gray) with a 1 cm diameter and 0.5 mm thickness (Polymax Ltd) that had been taped onto the coverslip. Different media were used: lab air, milli-Q water, ethanol and immersion oil. A second coverslip closed the liquid off on top to create a flat surface. To avoid capillary forces from squeezing the two coverslips together as part of the liquid evaporates, a small opening was left by the top coverslip at the silicone edge. Through this opening, water was added ever 30 min, or ethanol every 10 min to ensure that the

focal area was properly submerged. A typical measurement took about 1 min so that several measurements could be performed between refills in both cases.

Each z_p scan was performed over 5 μm in 40 pixel integrating over 100 ms/pixel, taking about 5 s in total per scan. The single beam and pump-probe experiments were both performed at the same time, where z_p scans with the pump beam on were alternated with scans with the pump beam blocked. About 5 iterations were done and the individual measurements averaged, giving a total measurement time of about 1 min per antenna. Each antenna had been measured individually for each surrounding medium.

5.4 Single beam experiments

In this section, the effect of focusing only the probe beam at 850 nm onto the nanoantennas was studied to find the dependence of various parameters on the transmitted light reaching the detector. First, the effect that different detection angles have are considered, followed by the antenna displacement through the focus, and finally the surrounding medium.

5.4.1 Detection angle

The model in the theory part was derived using the paraxial approximation for narrow detection angles. This is equivalent to using a low *NA* objective to collect the transmitted light. To study the effect that the detection angle has on the $\Delta P/P$ signal, measurements with a 0.5 *NA* and a 0.95 *NA* are compared for air as the surrounding medium. Figure 5.10a shows the antenna luminescence of two rows of antennas whose lengths ranged from left to right from 220-60 nm. The 5th antenna from the left is the brightest for both rows, corresponding to 180 nm antenna length. The smallest antenna, whose luminescence is still visible, is the 13th (100 nm). The luminescence counts of up to 400 counts/10ms are quite similar to single molecule fluorescence counts. Based on FDTD calculations, the antennas used in this chapter have $\sigma_{abs} \approx \sigma_{scat} \approx 10^{-10}$ cm², which is about six orders of magnitude larger than the single molecule absorption cross-section. Still, this is largely compensated by the low emission quantum yield of the antennas of ~10^{-4}-10^{-6} due to the electrons and holes rapidly relaxing towards the Fermi level via electron–electron and electron–phonon scattering[220–222].

For the $\Delta P/P$ signal in figure 5.10b, which had been collected with a 0.95 *NA* objective, the strongest signal is recorded for the 7th antenna (160 nm), and antennas beyond the 10th (130 nm) are no longer visible. This means that there is a 20 nm antenna length difference between the brightest luminescence and $\Delta P/P$ signal. According to the model plotted in figure 5.4, the resonant antenna results in the strongest $\Delta P/P$ signal for an antenna in the focus. The one-photon luminescence
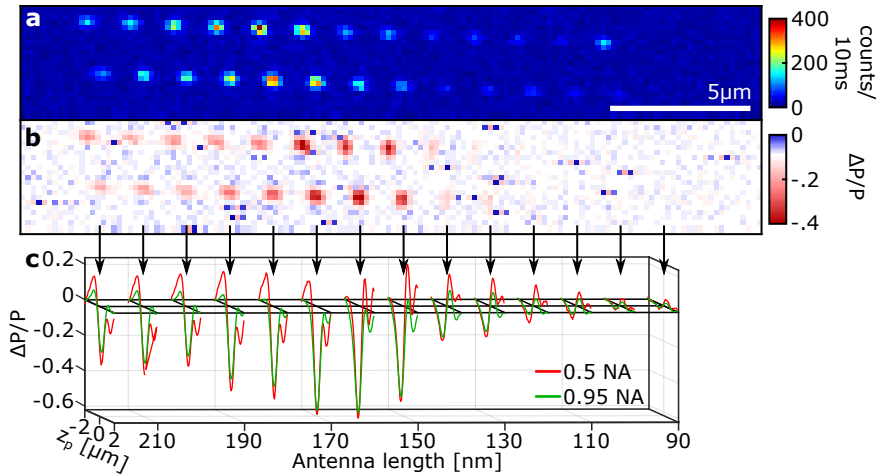
Figure 5.10: *Luminescence and $\Delta P/P$ of antennas in air.* **(a)** Luminescence and **(b)** $\Delta P/P$ signal of antennas from length 220-60 nm from left to right detected in focus with a 0.95 *NA* objective. **(c)** $\Delta P/P$ of the bottom row as a function of z_p for the different antenna lengths, detected with an objective with 0.5 *NA* (red) or 0.95 *NA* (green).

is also strongest when the excitation wavelength overlaps with the antenna resonance[221, 222]. However, it results in a luminescence spectrum that overlaps with σ_{scat} [222], the majority of which will be blocked by the laser cut-off filter at 885 nm for resonant excitation. That is why antennas slightly longer than resonance give most counts on the APD even though they do not luminesce most efficiently. The $\Delta P/P$ signal is measured without any filters in the beam path so that the resonance condition directly corresponds to the largest negative signal.

Scanning the antennas axially through the focus should confirm this since only the resonant antenna gives a dip centered at $z_p = 0$ based on the model. The z_p-scans for the bottom row of figure 5.10b are presented in figure 5.10c for transmission detection with a 0.5 *NA* (red) and 0.95 *NA* (green) objective. Here, the position of $z_p = 0$ has been assigned to each graph by fitting the luminescence signal with a Gaussian. The luminescence peak position corresponds to the antenna in focus at $z_p = 0$ irregardless of the antenna length since it does not depend on phase. In agreement with the model in figure 5.4a, $\Delta P/P$ has a dispersive positive-to-negative signature for long antennas, a dispersive negative-to-positive signal for short antennas and a single dip centered around $z_p = 0$ at the resonant antenna length of 160 nm which indeed corresponds to the brightest antenna. The signal for longer antennas is larger than that for shorter antennas, because longer antennas have the larger cross-sections due to larger volumes.

Figure 5.11 shows a representative long, resonant, and short antenna. The 220 nm long antenna in figure 5.11a exhibits the modeled dispersive positive-to-negative signal. For short antennas, this signal flips sign as shown in figure 5.11c for a
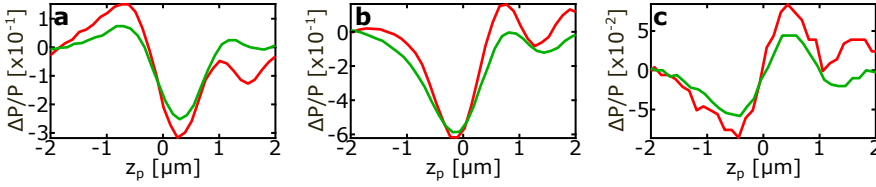
Figure 5.11: $\Delta P/P$ *of antennas in air.* $\Delta P/P$ vs z_p signal of antennas of length **(a)** 220 nm, **(b)** 160 nm, **(c)** 110 nm from figure 5.10 for the 0.5 NA (red) and 0.95 NA (green) objective.

110 nm long antenna. The antenna of this length had been invisible for the $\Delta P/P$ image in figure 5.10b due to the zero-crossing of $\Delta P/P$ at $z_p = 0$. As can be seen in figure 5.11b, the 160 nm long resonant antenna has the largest signal and it mainly exhibits a negative dip centered around $z_p = 0$, the signature for a resonant antenna. Therefore, the largest $\Delta P/P$ signal in figure 5.10 indeed corresponded to the resonant antenna. While the dip is not positioned perfectly at $z_p = 0$ but slightly below it, the neighboring antennas deviated even more from the ideal signal shape.

The signal shows additional oscillations for $z_p > 0$, especially in the measurement with the 0.5 NA objective. A signal contribution due to scattering off the ITO layer and coverslip to these oscillations beyond a phase change can be ruled out since they are not observed when measuring off the antennas. Instead, they likely originate from aberrations in the beam due to focusing through dielectric interfaces with mismatching refractive indices that lead to phase-modifications[170, 223].

Comparing the difference between the two objectives for the three antenna lengths in figure 5.11, the dispersive signal for long and short antennas is less pronounced for the 0.95 NA than for the 0.5 NA objective, while the dip for resonant antennas remains roughly the same. This is because the interference between the incident and scattered field averages out when integrating over many detection angles, the main signal contributor for off-resonant antennas. At resonance, absorption mainly contributes. This is why the signal strength drops mainly for non-resonant antennas, but the signal shape smoothens for all. This phenomenon has already been modeled for small gold nanospheres by Selmke et al. using Mie scattering theory[186]. In their case, the dispersive signature disappeared completely when the detection angle became larger than the excitation angle, giving rise to a single negative signal centered around $z_p = 0$ linked to absorption.

Still, while a smaller detection angle is more sensitive to the scattering component of $\Delta P/P$, less signal is detected overall, leading to a smaller signal-to-noise ratio. This becomes most apparent for the smaller antennas, which generally have a weaker $\Delta P/P$ signal due to their smaller size. The detection angle therefore is a trade-off between signal strength and noise.

All results could be satisfactorily described using only $\Delta P/P_1$ from the model. Any additional small component due to $\Delta P/P_2$ cannot be ruled out entirely. It would
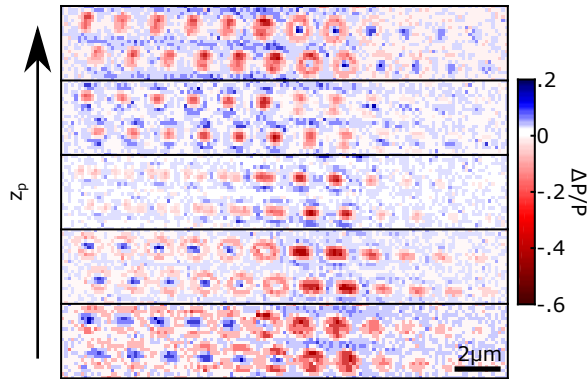
Figure 5.12: $\Delta P/P$ *maps scanned through* z_p. From bottom to top, z_p is increased by $0.5\,\mu m$ while recording $\Delta P/P$ in the xy-plane perpendicular to the beam propagation.

give a positive signal contribution that would be strongest at the resonant antenna. Considering that at resonance, the signal attenuates by almost 60 %, any positive $\Delta P/P_2$ contribution would be much smaller than the $\Delta P/P_1$ contribution. Since $\Delta P/P_2$ only becomes relevant for larger particles, the dominance of $\Delta P/P_1$ underlines the validity of the assumption of dealing with small particles.

5.4.2   Antenna displacement

Not only the axial, but also the lateral displacement affects the strength and sign of the transmitted intensity. Figure 5.12 shows xy-scans of the $\Delta P/P$ signal measured at different antenna heights in steps of $0.5\,\mu m$ for air using the $0.5\,NA$ objective. The scan in the middle of the figure was roughly in focus, as was verified by the diffraction limited luminescence spots on the corresponding confocal image (not shown). Only considering the signal in the center of each antenna for now, this basically is a very coarse z_p scan. In agreement with the $\Delta P/P_1$ model and previous results, long antenna lengths result in a negative-to-positive signal trend while short antennas in the opposite, and resonant antennas remain negative throughout. Off-resonant antennas have the strongest signal away from the focus, while the resonant ones have it at the focus.

The lateral antenna displacement, while not modeled, is still interesting to consider here as well. Just like the axial displacement, the lateral displacement also depends strongly on the phase difference between the incident and scattered light governed by the Gouy and scattering phase. When scanning through antennas in the xy-plane, a ring of opposite sign was occasionally observed around the main signal. In some cases, it even exceeded the signal strength of the central spot. This is due to aberrations of the point spread functions of tightly focused beams that result in peaks or dips at the beam edges, similar to an Airy pattern for a perfect lens[224]. They become especially visible for narrow detection angles since the scattering is

averaged over less angles [170]. The measurement of a central peak with lobes of the opposite sign is also in agreement with models and measurements of gold nanospheres, where the three-lobe structure emerged for small detection angles as well when moving the antenna laterally through the beam[170, 186].

This three dimensional scan underlines the importance of aligning the nanoantenna well in all three dimensions. When misaligned axially, non-resonant antennas give the strongest signal which might lead to the wrong assignation of the resonant antenna length. Lateral misalignment onto the ring could lead to the recording of a signal of opposite sign.

5.4.3 Surrounding medium

As has already been apparent from modeling σ_{ext} for different n_m in figure 5.2f, larger n_m values shift the antenna resonance to longer wavelengths. This is equivalent to shorter antennas being resonant for the same excitation wavelength. In the following, the antennas are surrounded by four different media: air ($n_m = 1$), water ($n_m = 1.33$), ethanol ($n_m = 1.36$) and immersion oil ($n_m = 1.52$). The antennas had been placed on a glass substrate ($n_{glass} = 1.52$) with a thin ITO layer ($n_{ITO} = 1.8$) on top, which both contribute to the shift in plasmon resonance as well.

Surface plasmons create an electromagnetic field around the antenna, which has an exponentially decaying field strength. The surrounding medium affects the plasmons. For larger n_m, the restoring forces of the free electrons are reduced, resulting in a stronger, narrower plasmon resonance peak that is shifted to higher wavelengths[201]. This can already be seen when modeling the polarizability from equation (5.1) for different n_m. Since the $1/e$ penetration depth of the electromagnetic fields is only around 1-2 times the antenna diameter[225], and strongest at the antenna surface, the effective refractive index will be treated as a surface problem here, rather than a volume problem. For this, the refractive index is weighted by the surface area S_i in contact with each medium, which leads to the effective refractive index expression

$$n_{m,eff} = \frac{S_{ITO} n_{ITO} + S_m n_m}{S_{ITO} + S_m}. \tag{5.27}$$

For example, an antenna with length 200 nm and width and height 50 nm, results in $n_{air,eff} = 1.18$, $n_{water,eff} = 1.43$,$n_{ethanol,eff} = 1.46$, and $n_{oil,eff} = 1.58$. The same values for a 100 nm long antenna are $n_{air,eff} = 1.18$, $n_{water,eff} = 1.42$, $n_{ethanol,eff} = 1.45$, and $n_{oil,eff} = 1.58$. Thus, the changes in n_m due to the ITO layer are more pronounced the larger the refractive index mismatch. For the experimental parameters used here, the antenna length does not appear to have a significant effect on $n_{m,eff}$. Going from air, to water/ethanol, to immersion oil, $n_{m,eff}$ increases by about 0.2 with each medium. Due to the linear relationship between n_m and AR, the resonant antenna lengths should therefore be spaced equidistantly for the different media.
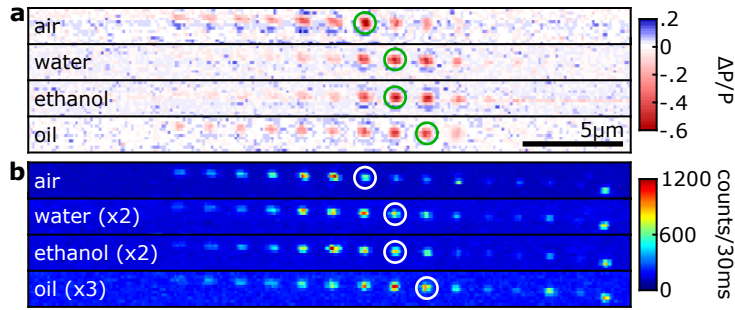
Figure 5.13: *Antennas in different media.* **(a)** The $\Delta P/P$ signal of antennas of decreasing length surrounded by air, water, ethanol or immersion oil. **(b)** The luminescence signal measured simultaneously. All images except for air were scaled by the factor given in the graph.

Figure 5.13a shows confocal images of $\Delta P/P$ measurements in the focus for the four media. The brightest spot and thus the resonant antennas indeed shifts towards shorter antenna lengths the larger n_m becomes. While for air, the 160 nm long antenna (7th) can be confidentially assigned as the brightest antenna, for the other three media it is a tie between 140 nm and 150 nm length. Therefore, z_p scans need to be consulted to make a definite assignment between the two antenna lengths for each of the liquids. Based on these z_p scans, which will be presented later in figure 5.14, the resonant antenna length was 150 nm for water and ethanol, and 140 nm for immersion oil, which were circled in the figure.

Figure 5.13b shows the simultaneously measured luminescence signal. Similar to the air results in figure 5.10a and b, there is a discrepancy between the brightest spot of the luminescence and $\Delta P/P$ graph due to the laser cut-off filter in case of the luminescence detection. Contrary to the $\Delta P/P$ results, the brightest luminescence signal for immersion oil is shifted to shorter antenna lengths with respect to water and ethanol. As a side note, the bright antennas on the right hand side (100 nm and 80 nm) were photodamaged and were not considered in this analysis.

The luminescence counts are about three times lower for immersion oil compared to an air objective. The larger the relative mismatch between the refractive index of the coverslip and the surrounding medium, the more light is radiated into the higher index material (i.e. coverslip) and under a smaller angle[226]. As a consequence, more luminescence is collected by the bottom objective for air than immersion oil. The scattered signal $\Delta P/P$ should also preferentially radiate into the higher index material[226]. Yet, the signal is comparable for all four media. Possible explanations for this similarity will be discussed later in this section when comparing the z_p scans.

To be able to interpret the $\Delta P/P$ data in more depth, z_p scans of all the different antenna lengths and in all four surrounding media were performed. Figure 5.14a shows measurements of the antenna lengths that best resemble the resonant condi-
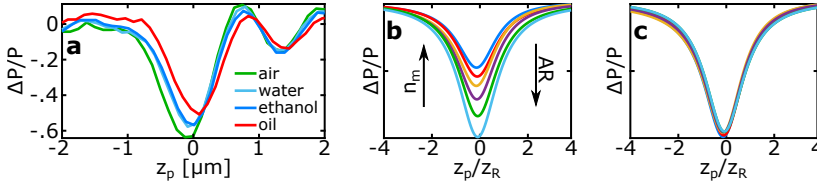
Figure 5.14: $\Delta P/P$ *signal for resonant antenna length.* **(a)** $\Delta P/P$ for resonant antenna lengths for different media: $160\,\text{nm}$ for air (green), $150\,\text{nm}$ for water (light blue) and ethanol (darker blue), and $140\,\text{nm}$ for immersion oil (red). **(b)** Simulated data for resonant excitation wavelength $725\,\text{nm}$. $n_m = 1.2 - 1.8$, $AR = 2.3 - 3.2$, with antenna length adjusted to obtain different AR. **(c)** Same as (b), but with AR normalized to the antenna's area $a \times b$.

tion for each medium; the symmetrical dip around $z_p = 0$. This length was $160\,\text{nm}$ for air (green), $150\,\text{nm}$ for water and ethanol (light and dark blue), and $140\,\text{nm}$ for immersion oil (red). The resonant $\Delta P/P$ signal for air is strongest and that immersion oil is weakest, with the one for water and ethanol having an equal intermediate signal strength. The four $\Delta P/P$ signals come from antennas of different lengths that were surrounded by media with different n_m. This behavior can be reproduced with the $\Delta P/P_1$ model given by equation (5.14). The results are shown in figure 5.14b for $n_m = 1.2 - 1.8$ corresponding to $AR = 3.2 - 2.3$ at $\lambda_{ex} = 725\,\text{nm}$. Just like for the measured data, the larger n_m (or the smaller AR), the smaller $\Delta P/P$ becomes.

The reduction in resonant signal strength for antennas in higher index materials may be either due to the increase in n_m or the decrease in antenna length or a combination of the two. In the simulations, AR had been varied by increasing or decreasing the length of the long axis of the spheroid to reflect the actual antenna sample. It is also possible to adjust AR by making the spheroids longer and narrower at the same time. When adjusting the antennas' dimensions such that their geometrical cross-section $a \times b$ remains constant, and otherwise not changing anything in the model, the $\Delta P/P$ signals all have the same strength. This is shown in figure 5.14c from where it can be concluded that, based on the spheroidal model, the signal strength at resonance depends predominantly on the antennas' dimensions.

This can be experimentally confirmed when looking at non-resonant antennas. Figure 5.15a shows a $220\,\text{nm}$ long antenna, which exhibits the expected positive-to-negative dispersive behavior for all four media. The $\Delta P/P$ signals resemble each other except for small deviations for the air results. The same is true for small antennas as figure 5.15c shows for a $120\,\text{nm}$ long antenna. All four $\Delta P/P$ graphs look almost identical in shape and signal strength again. Therefore, when far from resonance, n_m does not appear to have any significant influence on the shape nor the strength of $\Delta P/P$ as a function of z_p when measured on the same antenna. Instead, it depends mainly on the antenna dimensions. When going from $120\,\text{nm}$ to $110\,\text{nm}$ antenna length for example, an almost $50\,\%$ drop in $\Delta P/P$ signal intensity
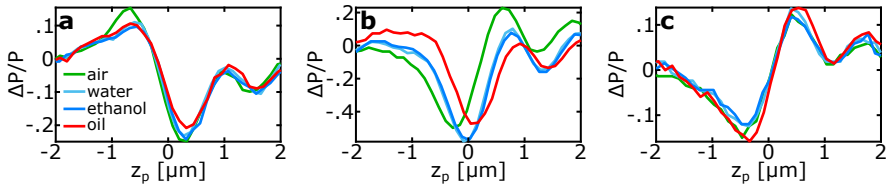
Figure 5.15: $\Delta P/P$ *for different n_m.* The $\Delta P/P$ signal as a function of z_p for antennas surrounded by air (green), water (light blue), ethanol (dark blue), or immersion oil (red). The graphs are shown for antenna length **(a)** 220 nm, **(b)** 150 nm, and **(c)** 120 nm.

is recorded for all four media. This change is consistently much larger than the differences seen between the individual graphs of the same antenna length.

As mentioned above, the similarity in off-resonant $\Delta P/P$ contrast for different surrounding media is surprising, since more scattered light disappears into the coverslip for lower n_m materials. Three different effects come to mind, though numerical simulations would be necessary to confirm any of them. First, due to the refraction of the transmitted light, a smaller effective detection angle is achieved for lower n_m media, consistent with a 10% drop in transmitted light reaching the detector for air compared to immersion oil as medium. Second, a larger refractive index mismatch leads to a weaker, though more forward directive scattering pattern, which may increase the $\Delta P/P$ contrast detected through the low *NA* objective. Third, as long as the antenna is smaller than the focal spot size, the excitation power reaching the antenna may be increased by an evanescence field generated at the surface of the coverslip for lower n_m media, thus resulting in a larger luminescence and $\Delta P/P$ signal for lower n_m materials. The change in scattering cross-section can be ruled out since it would lead to an increase in signal for longer antennas, and a decrease for antennas shorter than the resonance length.

The resonant antenna length differs by up to 20 nm from medium to medium and signal overlap for different surrounding media breaks down. Figure 5.15b shows a 150 nm long antenna, which is resonant for both water and ethanol. The antenna surrounded by air is resonant for longer, and the antenna surrounded by immersion oil for shorter antennas. This is reflected in the small dispersive component of opposite sign in their respective $\Delta P/P$ signal.

To conclude, the experimental results support the assumption that the particle dimensions and detection angle are more relevant to the $\Delta P/P$ signal strength and shape than the refractive index of the surrounding medium when measuring far from resonance. Around resonance, the gradual sign change of the dispersive $\Delta P/P$ signal makes it more sensitive to n_m.
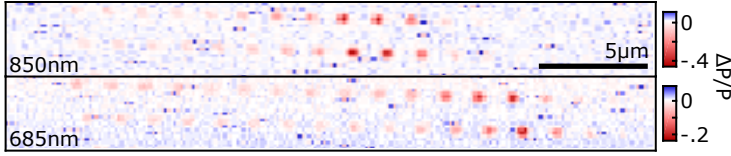
Figure 5.16: *Antenna resonance pump beam.* $\Delta P/P$ measurement of antennas in immersion oil for the 850 nm probe beam (top) and the 685 nm pump beam (bottom).

5.5 Pump-probe experiments

This section discusses the second objective of the chapter, which can be summarized as understanding the alterations of the transmitted beam induced by a modulated pump beam. Figure 5.16 shows that the pump beam resonantly excites antennas ~40 nm shorter than the probe beam at 850 nm. The same systematic steps as in section 5.4 were followed to determine how the detection angle, antenna displacement through the focus, and the surrounding medium affect the overall detected photothermal signal $\Phi = \Phi_{TL} + \Phi_\alpha$ for different antenna lengths.

While $\Delta P/P$ showed signal attenuation of up to 60 %, a much smaller signal strength is anticipated for Φ. A temperature increase of up to 10 K is anticipated for nanorods submerged in water based on measurements using resonant cw illumination[209]. With $\frac{dn}{dT} \approx -1 \times 10^{-4}\,\mathrm{K}^{-1}$, this translates to $\Delta n = -1 \times 10^{-3}$, much smaller than the one of 0.8 from the model plotted in figure 5.5. $\Delta n = -1 \times 10^{-3}$ is already one order of magnitude smaller than the refractive index difference between water and ethanol, which was impossible to differentiate in the $\Delta P/P$ graphs looking at the n_m dependence in figure 5.15. Assuming from the $\Delta P/P$ results that $\Delta P/P_{ethanol} - \Delta P/P_{air} < 10^{-2}$, it follows that $\Phi_\alpha < 10^{-3}$ for water.

Signals can be resolved with an excellent signal-to-noise ratio with the pump-probe setup developed in chapter 4, where the detection with a lock-in amplifier resulted in a sensitivity of ~10^{-7}. When the heating beam does not overlap with the resonance of σ_{abs}, Δn becomes even smaller. All measurements in this section were performed with a 1 MHz pump beam modulation. The demodulated in-phase and out-of-phase signal were both recorded. Since they were the same except for the phase difference, only the stronger in-phase component is given in the presented results. Due to the simultaneous measurement of $\Delta P/P$ and Φ by alternating a $\Delta P/P$ measurement with the pump beam blocked and a Φ measurement with the pump beam unblocked, all results from this section can be directly compared to the ones from the single beam experiments in the previous section.

For the interpretation of the results, it has to be taken into account again that the antennas are not surrounded by a homogeneous environment, but were placed onto a glass coverslip with an ITO layer, and in contact with the surrounding medium only at the other sides. For the photothermal detection, not only n_m, but also the
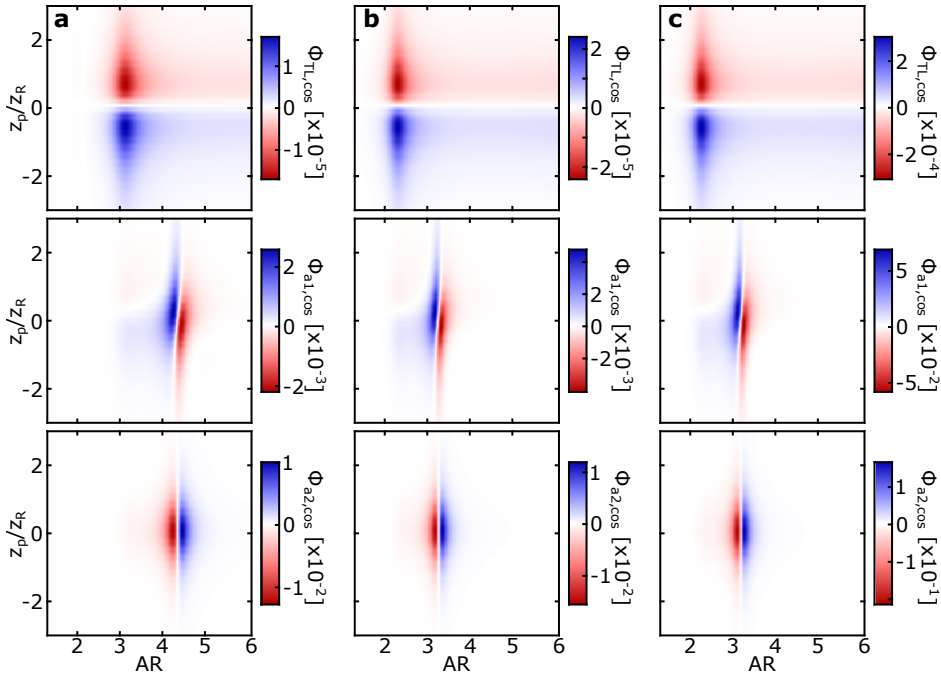
Figure 5.17: *Simulation of* Φ_{TL}, $\Phi_{\alpha 1}$ *and* $\Phi_{\alpha 2}$ *for the different media.* Taking into account having ITO and glass below the antennas, the combined signal is modeled for **(a)** air, **(b)** water, and **(c)** ethanol. Model parameters in figure 5.5.

photothermal properties such as $\frac{dn}{dT}$, C_p and κ need to be considered. Glass and ITO have a positive $\frac{dn}{dT}$, while the other media have a negative one. Therefore, the temperature change increases the refractive index of glass and ITO, and decreases it for the media placed on top of the coverslip. The sign of Δn determines the sign of the measured effect, and the interplay between positive and negative Δn partially compensate each other. To get a better understanding of the importance of each medium, the cases of air, water, and ethanol as surrounding medium were modeled.

The thermal lens effect Φ_{TL} is based on a refractive index gradient that spreads hundreds of nm and that is probed by a focused beam which has a radius of hundreds of nm at the antenna position as well. Therefore, the ITO layer of only 10 nm thickness is not expected to contribute significantly to the thermal lens and will be ignored in the Φ_{TL} model. The thermal lens due to the two hemispheres of refractive index gradient with glass at the bottom and the surrounding medium on top were considered to contribute equally to Φ_{TL}. The results are plotted in the top row of figure 5.17. The overall thermal lens has a positive-to-negative dispersive signal characteristic of a $\frac{dn}{dT} < 0$ medium for all surrounding media since the thermal lens effect of glass is at least one order of magnitude smaller than that of any of the other media as modeled in figure 5.7.
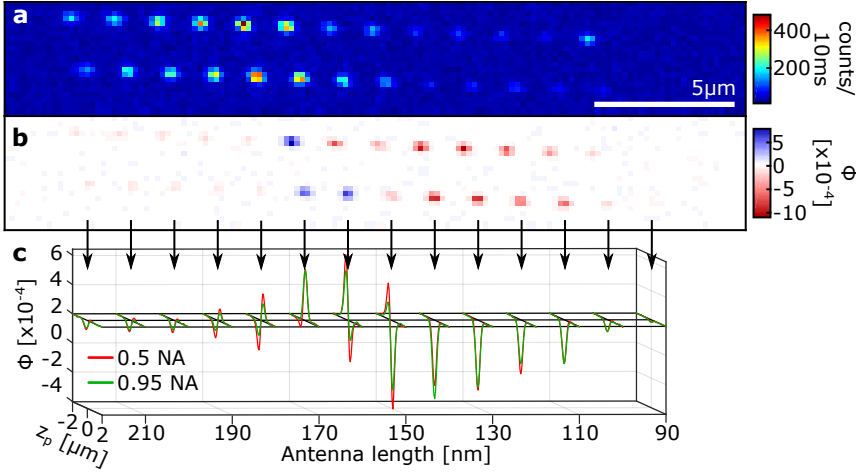
Figure 5.18: *Luminescence and Φ of antennas in air.* **(a)** Luminescence and **(b)** Φ signal of antennas from length 220-60 nm from left to right detected in focus with a 0.95 *NA* objective. **(c)** Φ of the bottom row as a function of z_p for the different antenna lengths, detected with an objective with 0.5 *NA* (red) or 0.95 *NA* (green).

In contrast to Φ_{TL}, the change in polarizability Φ_α depends mainly on the refractive index change near the antenna surface. That is why $n_{m,eff}$ from equation (5.27) was used to calculate the surface averaged contribution of each medium to the antenna polarizability. For this, the time-dependent refractive index change $\Delta n(\Omega, r, t)$ from equation (5.18) was used. The second and third row of figure 5.17 show the $\Phi_{\alpha 1}$ and $\Phi_{\alpha 2}$ results. As the majority of surfaces was surrounded by air, water or ethanol, and $\Delta n \propto \frac{dn}{dT}/\kappa$ is either comparable or smaller for the surrounding media, the $\frac{dn}{dT} < 0$ contribution dominated. For this reason, all subsequent experimental results will be interpreted as a $\frac{dn}{dT} < 0$ medium.

Figure 5.17 showed that for the chosen model parameters, the signal of Φ_{TL} is at least two orders of magnitude smaller than that of Φ_α for all three media, while that of $\Phi_{\alpha 1}$ is one order of magnitude smaller than $\Phi_{\alpha 2}$. The results of the previous sections already showed that the relative signal strengths between the modeled components $\Delta P/P_1$ and $\Delta P/P_2$ does not reflect the ratio found in experiments, where $\Delta P/P_1 \gg \Delta P/P_2$. Still the $\Delta P/P_1$ model qualitatively agreed well with measurements. From this a qualitatively correct Φ_α and Φ_{TL} model with $\Phi_{\alpha 1} \gg \Phi_{\alpha 2}$ is anticipated.

5.5.1 Detection angle

As had already been shown in the previous section, the detection angle affects $\Delta P/P$. There, the larger the detection angle, the more important the absorption contribution became compared to the scattering contribution and the dispersive $\Delta P/P$ signal converged into a dip centered around the focus for large enough detection angles.
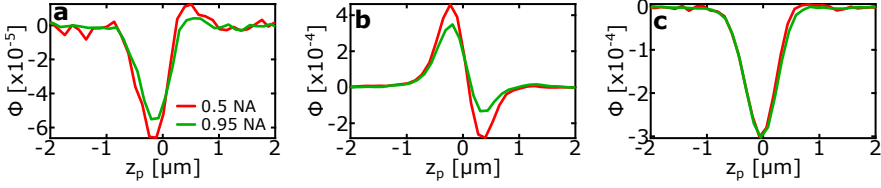
Figure 5.19: Φ *of antennas in air.* Φ vs z_p signal of antennas of lengths **(a)** 220 nm, **(b)** 160 nm, and **(c)** 110 nm from figure 5.18 for the 0.5 *NA* (red) and 0.95 *NA* (green) objective.

The Φ signal also depends on the detection angle as will be demonstrated in the following.

The luminescence and photothermal signal in the focal plane are shown in figure 5.18a and b. The Φ signal, which had been detected with the 0.95 *NA* objective, has a negative signal for both short and long antennas, though a positive one around resonance. Yet, the most resonant antenna length, which is 160 nm (7th), shows a negative signal for one and a positive one for the other row. A simple assignment of the resonant antenna to the largest signal therefore appears to be impossible by exclusively looking at the antenna signal in the focus.

Just as $\Delta P/P$, Φ depends strongly on z_p so that scanning the antennas through the focus would give more insight into the origin of the Φ contrast. Figure 5.18c shows the results for all antenna lengths collected with both the 0.5 *NA* (red) and 0.95 *NA* (green) objective. For both objectives, the Φ signal from long to short antennas goes from a negative signal, to a dispersive negative-to-positive signal, to a peak at 170 nm antenna length, to a dispersive positive-to-negative signal and finally to an exclusively negative signal again. This exactly follows the $\Phi_{\alpha 1}$ model results from figures 5.8 and 5.17, except for the shortest antennas where a dispersive signal had been anticipated for both $\Phi_{\alpha 1}$ and Φ_{TL}. Overall, Φ shows a much richer change in signal shapes than $\Delta P/P$ measurements and is stronger for short than for long antennas. The signal strength is related to the short antennas heating their environment more efficiently due to the better overlap with the heating beam.

Figure 5.19 shows Φ for a long, resonant, and short antenna to be able to look at the effect of the detection angle in more detail. The detection with the 0.5 *NA* objective (red) will be considered first. In figure 5.19a, the 220 nm long antenna shows a dip at $z_p < 0$ with a small positive contribution at $z_p > 0$, in figure 5.19b the 160 nm long resonant antenna shows a dispersive positive-to-negative signal, and in figure 5.19c the 110 nm short antenna shows a dip at $z_p = 0$. For the thermal lens effect Φ_{TL} it has already been shown both experimentally and theoretically that larger detection angles lead to smaller overall signals[194, 217]. For Φ_α no such models are known. Still, since it is the difference between $\Delta P/P$ measured at two different n_m, the expected behavior can be deduced. First, $\Delta P/P$ is smaller for larger detection angles, so that Φ_α should also become smaller for larger *NA* objectives since two smaller
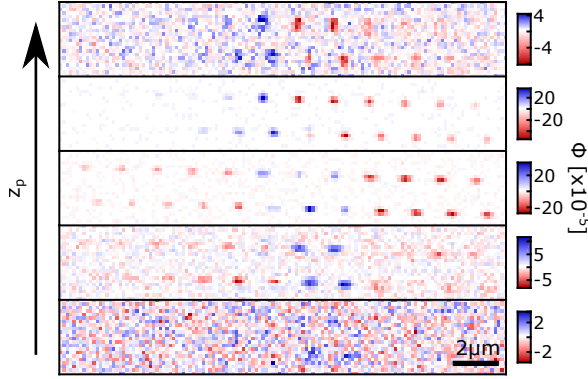
Figure 5.20: Φ *maps scanned through* z_p. From bottom to top, z_p is increased by 0.5 μm while recording Φ in the xy-plane perpendicular to the beam propagation direction.

numbers are subtracted. Following this line of thought, the detection angle has a larger effect on long antennas that scatter more. Second, the dispersive nature of $\Delta P/P$ disappeared for larger NA so that the Φ_α signal contributions away from $z_p = 0$ should become less pronounced for larger detection angles.

Both effects can indeed be observed in the data presented in figure 5.19. For the long and resonant antenna, the signal strength is reduced when comparing the detection with the 0.5 NA objective (red) to that with the 0.95 NA objective (green), while that of the short antenna is almost unchanged. The small positive feature in the 0.5 NA measurement of the long antenna also became less pronounced in with the 0.95 NA objective.

Just as for the $\Delta P/P$ measurements, the lower NA resulted in larger signals with richer features relating to scattering, while the higher NA offered a better signal-to-noise ratio due to the collection of more light. This becomes most pronounced for long antennas, which have the weakest signal. Still, both detection angles result in signal strengths $\sim 10^{-4}$, which can be picked up by lock-in amplifier with excellent contrast.

5.5.2 Antenna displacement

The effect of the lateral and axial particle displacement is considered next. Figure 5.20 shows the area scans of Φ for different antenna positions along the beam axis. Long antennas lead to a negative-to-positive signal of which the sign flip shifts towards smaller z_p (6th antenna column). For the resonant antennas (7th), the signal abruptly changes to a positive-to-negative one that turns into an overall negative signal for short antennas. As anticipated, this follows the same trend as the z_p scans from figure 5.18c.
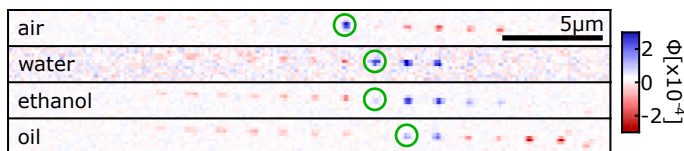
Figure 5.21: *Antennas in different media.* **(a)** The Φ signal of antennas in the focal plane surrounded by air, water, ethanol or immersion oil.

The spot size is small compared to the simultaneously measured $\Delta P/P$ signal plotted in figure 5.12. $\Delta P/P$ scales with the beam intensity at the antenna position, which for the axial antenna position scales as a Lorentzian $[1 + (z_p/z_R)^2]^{-1}$. $\Phi(z_p)$ additionally scales by the intensity of the heating beam at the antenna position given by $[1 + (z_p/z_{R,h})^2]^{-1}$, with $z_{R,h}$ substituting z_R. $\Phi(z_p)$ scales as the product of the two Lorentzian line shapes and the signal strength drops much faster. The intensity profile in the lateral position is given by a Gaussian $\sim \exp(-2\rho^2/w^2(z_p))$. The additional dependence on overlap with heating beam sees this multiplied by $\sim \exp(-2\rho^2/w_h^2(z_p))$ leading to a much faster exponential decay of the signal.

If the pump and probe laser were not coaligned, but the pump beam focus followed the antenna position in the probe beam in all three dimensions, optimal heating would be guaranteed at all times, and the signal would scale with the intensity of only the probe beam again as $[1 + (z_p/z_R)^2]^{-1}$[170].

The rapid decrease in Φ signal makes the proper alignment in all three dimensions crucial for measurements with high contrast. Lateral misalignments leading to a sign change due to the ring of opposite sign formed around the main signal are less likely to than for $\Delta P/P$ since the rapid signal decay makes them much weaker than the central Φ signal in all cases. Still, due to the dispersive nature of Φ in z_p for many antenna lengths, the antenna position within the focus needs to be known with high precision, or even better, a z_p scan could be performed.

5.5.3 Surrounding medium

Having already demonstrated the importance of the antenna position in the focus and that $\Phi_{\alpha 1}$ from the model reproduces the air results, the influence that the surrounding medium has on photothermal detection is now considered. Figure 5.21 shows the Φ signal at $z_p \approx 0$ of nanoantennas of different lengths surrounded by the different media. The resonant antennas were circled again. The negative signal for long antennas is almost invisible in all four cases due to the inefficient heating. At the resonant antenna length, the sign flips and Φ is positive. For short antennas, air and immersion oil give a negative signal whereas that for water and ethanol stayed positive and fades into the background faster. Due to the dispersive nature of Φ for most antenna lengths, the sign discrepancies might simply be due to small

antenna misalignments from the focus. However, different antenna responses to the photothermal parameters of each medium cannot be ruled out, either.
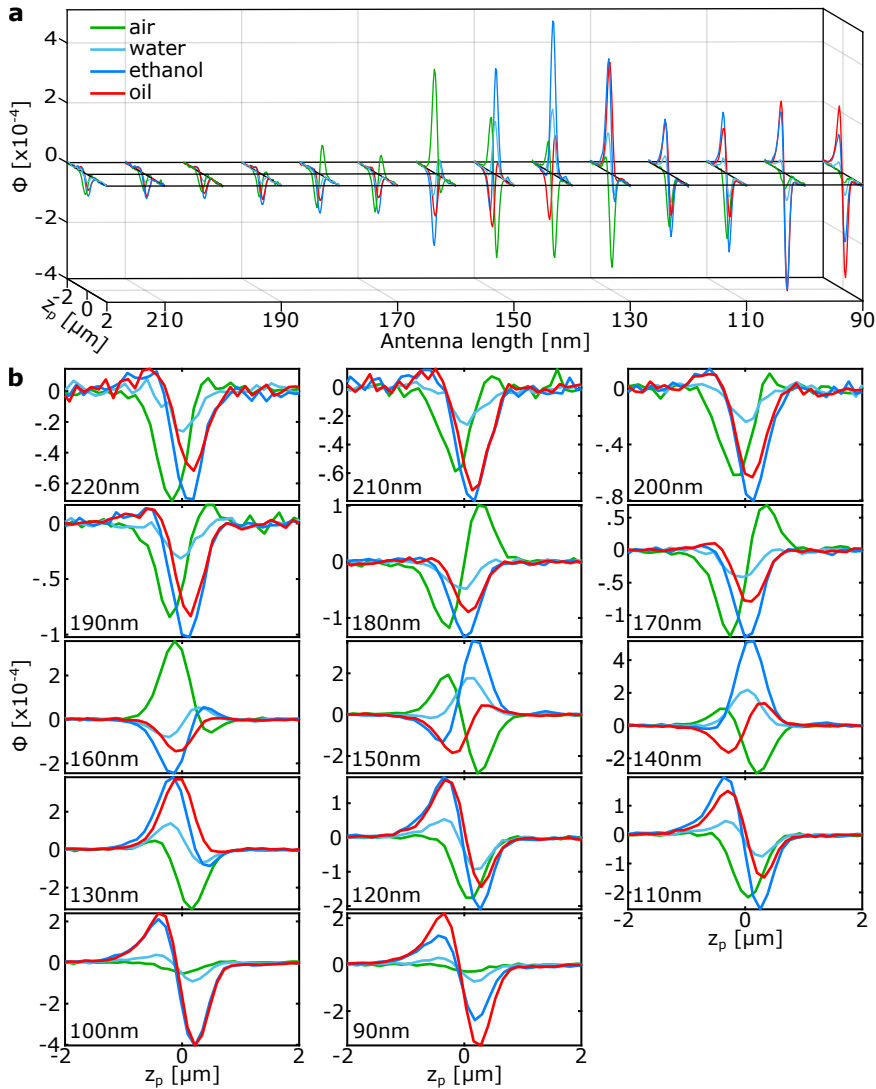
Figure 5.22: Φ *for different* n_m. **(a)** The Φ signal as a function of z_p for antennas surrounded by air (green), water (light blue), ethanol (dark blue), or immersion oil (red). **(b)** The individual results for antenna lengths 220-90 nm from top left to bottom right.

Figure 5.22a shows z_p scans of the Φ signal of all the different antenna lengths for all for media. The signal for all four media evolves in the same way, from a negative, to a negative-to-positive, to a positive, and finally a positive-to-negative signal, with short antennas in air being the only exception from this trend. Depending on the medium and its resonant conditions, the transition occurs for longer or shorter

antennas and with a different strength. Longer antennas for example generally gave a weaker signal due to the inefficient heating related to the poor overlap of the pump beam wavelength with σ_{abs}.

To fully appreciate the range of signal strengths and shapes, the results were plotted individually for each antenna length in figure 5.22b. Several of the signal similarities and differences between the different antenna lengths and surrounding media are discussed in the following.

Comparing the scans in focus from figure 5.21 to the z_p scans in figure 5.22b, the sign of Φ_{TL} in the former agrees well with the sign of the latter at $z_p = 0$ for air, water, and ethanol. For immersion oil, the antennas had been placed a bit above the focus. This can be seen best for antenna length 150 nm. In the confocal image it gave no signal, which corresponds to $z_p > 0$ in the z_p scan.

While $\Delta P/P$ had been largely independent of the surrounding media, Φ depends strongly on their photothermal properties. This can be seen well when comparing water and ethanol. They have a comparable n_m, and therefore also a comparable polarizability in the unheated case. Ethanol has a four times larger $\frac{dn}{dT}$ and a three times smaller κ than water, both of which lead to a larger Δn according to equation (5.18). The measurements reflect this, where ethanol has a roughly three times larger Φ signal than water for all antenna lengths.

Φ of water and ethanol mainly scale in intensity, even though a variation in signal shape can occasionally also be observed. A good example for this is the 150 nm long resonant antenna. While the antenna submerged in water had a positive signal throughout, the one in ethanol had a negative-to-positive divergent signal. Near resonance, the Φ signal transitions from negative-to-positive to exclusively positive when going to shorter antenna lengths. The refractive index of ethanol is 0.03 larger than that of water, which means that a slightly smaller antenna is resonant in ethanol than in water. This is supported by the fact that for antenna lengths that are far from resonance, and where the signal change is more gradual, no significant signal changes are registered.

This remarkable sensitivity to small changes in experimental parameters near resonance can also be seen back in the air results. The z_p scans measured for the detection angle and the surrounding media were based on different antenna rows. The 160 nm long antenna was the most resonant in both cases, exhibiting a dip at $z_p \lesssim 0$ with a comparable signal attenuation of ~60 % (see figure 5.11a, figure 5.14b). Still, in the former case, a dispersive positive-to-negative signal was recorded for Φ (figure 5.19b), but a positive signal with a small negative contribution at $z_p > 0$ for the latter (figure 5.22b). Around resonance, going to shorter antennas the positive signal transitions further into a dispersive positive-to-negative signal. With this in mind, the resonant antenna with the positive-to-negative dispersive shape is likely

shorter than the one with the peak even though this difference was too small to be resolved by the $\Delta P/P$ measurements.

Signal variations are not limited to resonant antennas. Something that sticks out in this context is that the signal measured in air differs quite a bit from that measured in water, ethanol and immersion oil which follow the same signal trends. For one thing, the three liquids have a dispersive positive-to-negative shape at short antennas, as anticipated for both $\Phi_{\alpha 1}$ and Φ_{TL} models. For air, the same antennas result in a Φ that is a dip centered around $z_p = 0$. The origin of the negative component could originate from $\Phi_{\alpha 2}$, which does give a negative signal there. However, since it was irrelevant for the interpretation of the $\Delta P/P$ data which did not show any appreciable difference in for the different refractive indices (see figure 5.15c). More experiments would be necessary to find the origin of this signal.

For long antennas, the shape of the Φ signal measured in air also differs considerably from that for the three liquids. Air gives a negative dip at $z_p < 0$ accompanied by a small peak at $z_p > 0$, whereas the other three media give a small peak at $z_p < 0$ accompanied by a large dip at $z_p > 0$. The air results remain in that shape before starting to transition around 180 nm antenna length, about 20 nm before resonance is reached. The other media start the shape transition only for antennas 10 nm before their resonance, starting with the negative-to-positive shape that antennas in air have exhibited for all long antennas. Based on these observations, it may be concluded that the signal shape transitions more gradually for air. This is in agreement with the Φ models shown in figure 5.17, where the simulation for air also showed a more gradual signal change than water or ethanol. This relates all the way back to the polarizability in equation (5.1). For larger n_m, the surface plasmons are damped less, resulting in a red-shifted resonance with a stronger, narrower peak. Therefore, the lower n_m of air contributes to the broadening in Φ. When modeling Φ, a change in any of the other parameters of the surrounding media ($\frac{dn}{dT}$, κ, C_p), or the antenna dimensions did not show a significant Φ broadening. For the antenna dimensions, their aspect ratio had been modeled for constant width and height b, constant length a, constant area $a \times b$ and constant volume $a \times b^2$.

$\Phi_{\alpha 2}$ and Φ_{TL} were not necessary to explain the obtained results. For $\Phi_{\alpha 2}$ this had been anticipated since $\Delta P/P_2 \ll \Delta P/P_1$. For Φ_{TL} the story is a bit more complicated. For short antennas that are resonant with the pump beam, the Φ_{TL} contribution should be strongest. However, its signature dispersive positive-to-negative signal has the same shape as $\Phi_{\alpha 1}$ and both scale linearly with the power of the pump beam through equation (5.15). Since $\Phi_{TL} \propto \sigma_{abs} \propto V$ and $\Phi_{\alpha 1} \propto \sigma_{scat} \propto V^2$, their individual contribution may be untangled by performing additional measurements on antennas with the same resonance but different volumes. Or the pump beam wavelength could be chosen longer than the probe beam wavelength so that both signals had a different shape.

An effect that has been ignored so far is the temperature increase due to the probe beam interacting with the antennas. The unmodulated probe beam power is similar to the power of the modulated heating beam and should therefore lead to a static thermal lens of comparable magnitude. Its contribution could in principle occur through the out-of-phase measurement of a single modulated beam[227]. However, the linear relationship between the excitation power and temperature increase, as the negligible contribution of the thermal lens effect to the signal, mean that probe beam heating only results in a constant refractive index offset in the experiment that is strongest for resonant antennas. The refractive index change is too small to be resolved in the $\Delta P/P$ results ($\sim 10^{-1}$), but would lead to a slightly shifted Φ signal due to a change in resonance frequency. In addition, any significant heat buildup over time can be ruled out since no signal difference between the first and last scan were observed for any medium or antenna length[228].

Overall, it has been shown that contrary to $\Delta P/P$, Φ is extremely sensitive to its environment and not only to the antenna length. Especially around the resonant antenna length, small differences in n_m and antenna dimensions that had been indiscernible in $\Delta P/P$, were picked up by Φ. The main contributor to the signal was the change in polarizability $\Phi_{\alpha 1}$. This underlines that measuring photothermal effects on refractive index sensitive nanoantennas with $\sigma_{abs} \sim \sigma_{scat}$ instead of nanospheres with $\sigma_{abs} \gg \sigma_{scat}$, the thermal lens effect no longer is the dominant signal contributor, also when probing off-resonant.

5.6   Conclusion

A framework has been developed to describe the interaction of tightly focused light with gold nanoantennas of different lengths, at various focal positions, and surrounded by several media. This model enhanced the understanding of the influence that these interconnected parameters have on the transmitted beam in far-field detection. Experiments that systematically probed these parameters agreed well with the developed model for both single beam scattering and pump-probe photothermal measurements.

The single beam experiments showed the interplay between the position dependent Gouy phase and the antenna resonance dependent scattering phase. When scanning antennas axially through the focus, long antennas exhibited a positive-to-negative dispersive interference signal, resonant ones a dip and the short ones a negative-to-positive dispersive signal. It had been further shown that smaller detection angles prevent the averaging out of the scattering, which leads to a stronger scattering signal at the cost of a reduced signal-to-noise ratio. For non-resonant antennas, the antenna dimensions had much stronger influence on the measured signal than the refractive index.

For the photothermal pump-probe experiments, the change in polarizability was the main contributor to the photothermal signal for the chosen refractive index sensitive antenna geometry with $\sigma_{abs} \sim \sigma_{scat}$. The signal shape and strength was sensitive to the antenna position and plasmon resonance and depended on both the refractive index and photothermal properties of the surrounding medium, besides the antenna dimensions. Especially near the antenna resonance, the detected signal transitioned between various shapes, demonstrating the sensitivity of this method to refractive index changes and changes in antenna dimensions. Smaller detection angles again lead to a larger signal with a lower signal-to-noise ratio.

This chapter has shown systematically that both the excitation wavelength and antenna position should always be considered when measuring the transmitted signal of gold nanoantennas in a tightly focused beam. For photothermal experiments, the contribution of the change in polarizability upon refractive index change should not be ignored for refractive index sensitive particles. The improved understanding of especially the photothermal signal for these larger particles will allow for better designed experiments and interpretation.

If properly calibrated, the refractive index, $\frac{dn}{dT}$ and κ sensitivity of the system could be exploited in sensing applications. Since these measurements are performed on a single antenna, very small detection and sample volumes would suffice to achieve signals with excellent signal-to-noise ratios as demonstrated here. Just as in single molecule experiments, single antenna methods have the advantage of beating the signal broadening of ensemble measurements. Yet, it needs to be performed as an axial scan or with high antenna position stability near a point of inflection of the photothermal signal.

Conclusion

The work that was presented in this thesis explored innovative and effective techniques to measure the spectral response of individual molecules and nanoantennas with two-beam excitation. All experiments were performed at room temperature, where (bio)molecules can be studied in a more natural environment than at cryogenic temperatures, at the cost of significantly reduced signal strength and stability. First, Fourier transform spectroscopy was introduced to single molecule spectroscopy, enabling the robust measurement of excitation spectra at room temperature. Second, a setup for shot noise limited detection of stimulated emission was developed with $\sim 10^{-8}$ sensitivity. Third, an analytical model for the scattering and absorption contribution of plasmonic nanoparticles in photothermal measurements was derived and systematically tested experimentally which took into account the different signal contributions for refractive index sensitive scatterers.

In the first part, Fourier transform spectroscopy at the single molecule level was pioneered to measure fluorescence excitation spectra. These spectra probe the excited state manifold, thus complementing the routinely measured emission spectra, which probe the excited state manifold. Using synthetic QDI molecules, which are relatively photostable and bright, it was demonstrated that Fourier transform spectroscopy is robust against blinking and photobleaching and that spectral variations of more than 100 nm can be probed at once due to the simultaneous excitation over the full spectral bandwidth. Next, excitation and emission spectra of weakly fluorescing LH2 complex where measured, which underlined the sensitivity of the technique. The lack of correlation between the B800 and B850 band showed that the two rings react to environmental changes independently, the former being weakly and the latter strongly coupled. The single complex Stokes shift showed variations and the shift is on average larger for red-shifted complexes and about 20 % larger than the ensemble Stokes shift. With this quantification of the disorder, important variables for both models and the interpretation of experimental results were provided, which will help with the interpretation of observed long-lasting coherences. In principle, single molecule Fourier transform spectroscopy can be transferred to any system requiring the robust and sensitive measurement of excitation spectra with diffraction-limited spatial resolution.

In the second part, a highly sensitive cw pump-probe setup was designed to detect stimulated emission of single DBT molecules. The setup was systematically brought to the shot noise level utilizing a shot noise limited laser diode, avoiding reflections in the beam path, and suppressing electronic noise. The achieved sensitivity was $\sim 10^{-8}$ compared to the estimated 2.3×10^{-8} signal-to-background ratio necessary for individual DBT molecules. In addition, the luminescence detection with a band-pass filter between the pump and probe beam wavelength minimized

the background level of stimulated emission depletion measurements. The good alignment of the setup was confirmed by a 70 % fluorescence depletion efficiency. Yet, no stimulated emission signal was observed despite several improvements of the experimental design compared to earlier attempts. To achieve an even larger signal-to-background ratio, the ratio σ_{abs}/A between the absorption cross-section σ_{abs} and the beam waist area A needs to be improved. This can be done by either choosing a molecule with a larger σ_{abs} or by selecting a molecule that can be stimulated down at a lower wavelength to decrease A. Once achieved, the time scale at which stimulated emission occurs would allow for the direct probing of ultrafast coherent excited state processes, which currently relies on the indirect probing through fluorescence.

In the third part, photothermal microscopy on plasmonic gold nanoantennas exploits the high sensitivity of the stimulated emission setup. A comprehensive analytical model based on Gans theory described the interaction of a single tightly focused Gaussian beam with gold nanoantennas. The effect of a heating beam on the signal was then explained by a change in refractive index using a thermal lens model that considers the contribution of both the change in polarizability and the thermal lens effect. Existing models neglected the contribution of the polarizability for refractive index sensitive scatterers, or the Gouy phase of tightly focused beams. This neglect leads to a clear mismatch between existing models and reality, which was demonstrated by systematically probing the interconnected contributions of the antenna lengths, positions in the focus, detection angles and in different surrounding media. In the single beam case, dispersive interference signal between the incident and scattering light arose in tightly focused beams that predominantly depended on the antenna position, resonance, and dimensions, but not on the refractive index of the surrounding medium. The photothermal pump-probe measurements showed that the differential signal relied strongly on the antenna position, dimension, and resonance length, as well as the photothermal properties of the surrounding medium. The dominant contribution comes from the change in polarizability for refractive index sensitive scatterers nanoantennas, in contrast to the photothermal lens effect that predominates the signal for strong absorbers. The computationally and conceptually accessible models agreed qualitatively with the measured results and will help to better interpret results. The improved understanding of the complex interplay between different contributions to the signal can be used in future applications.

Very diverse experimental techniques and models have been presented throughout this thesis. All of them revolved around the spectral detection of single particles through a confocal microscope in thus far unexplored regimes. They can be applied to a wide range of applications that require high sensitivity or spatial selectivity, including, but not limited to, quantum dots, color centers in diamonds, plasmonic nanoparticles, biological cells, and other nanometric structures.

Publications

- L. Piatkowski, E. Gellings, and N. F. van Hulst. "Multicolour single molecule emission and excitation spectroscopy reveals extensive spectral shifts". *Faraday Discuss.* 184 (2015), pp. 207–220.

- L. Piatkowski, E. Gellings, and N. F. van Hulst. "Broadband single-molecule excitation spectroscopy". *Nat. Commun.* 7 (2016), p. 10411.

- E. Gellings, S. Faez, and L. Piatkowski. "Highlights from Faraday Discussion 184: Single-Molecule Microscopy and Spectroscopy, London, UK, September 2015". *Chem. Commun.* 52.11 (2016), pp. 2213–2219.

- E. Gellings, R. Cogdell, and N. F. van Hulst. *Room temperature excitation-emission spectra of single LH2 show remarkably little variation.* [manuscript written].

Acknowledgements

Including my master thesis, I have spent the past 6 years at ICFO and in Barcelona. In that period, I have met many great people that I would like to thank here for their support in the completion of this doctoral thesis. There are several people that I would like to thank in particular:

First and foremost, I would like to thank my supervisor Niek van Hulst for providing guidance whenever needed. Thanks for letting me find my own path in the Molecular Nanophotonics Group!

A huge thank you also goes to the entire Molecular Nanophotonics group. Łukasz for showing me the ropes during my first project. To Lisa, Vikas and Richard for helping me get started on the LH2 complex. To Matz for offering new ideas whenever I really got stuck somewhere and introducing me to DBT. To Alex D. for the initial collaboration on the stimulated emission project. To Alex B., Ion, Paweł, Lisa and Monse for helping me make sense of my antenna results. To Jana and Paweł for proofreading part of the thesis. To the rest of the team for their support and endless discussions about science and life and everything in between: Luca, Gaëtan, Pablo, James, Unai, Nicola, Anshuman, and Emilie.

Another big thank you goes to the rest of ICFO. To the ICFO management and administration units for taking good care of all our non-scientific challenges. To the electronic and mechanical workshops for providing me with the necessary tools. To ICONS for all the great initiatives. To the futbolín fanatics for the friendly competitions. And to everyone who I crossed paths with, for making my time at ICFO special.

Beyond ICFO, I would like to thank my extended Rotary friends and family for the amazing time and the opportunity to grow alongside you. And to Salty Frisbee for many a Sunday and more well spent at the beach.

Last but not least, I would like to thank my family for always being there when I needed them despite the distance.

Bibliography

[1] I. Newton. "A letter of Mr. Isaac Newton, Professor of the Mathematicks in the University of Cambridge; containing his new theory about light and colors: sent by the author to the publisher from Cambridge, Febr. 6. 1671/72; in order to be communicated to the R. Society". *Philos. Trans. Roy. Soc. London* 6.80 (1671), pp. 3075–3087.

[2] W. H. Wollaston. "XII. A method of examining refractive and dispersive powers, by prismatic reflection". *Philos. Trans. Roy. Soc. London* 92 (1802), pp. 365–380.

[3] J. Fraunhofer. "Bestimmung des Brechungs- und des Farbenzerstreuungsvermögens verschiedener Glasarten, in Bezug auf die Vervollkommnung achromatischer Fernröhre". *Ann. Phys.* 56.7 (1817), pp. 264–313.

[4] J. F. W. Herschel. "XXXI. On the Absorption of Light by Coloured Media, and on the Colours of the Prismatic Spectrum exhibited by certain Flames; with an Account of a ready Mode of determining the absolute dispersive Power of any Medium, by direct experiment". *Trans. R. Soc. Edinburgh* 9.2 (1823), pp. 445–460.

[5] W. H. F. Talbot. "Some experiments on coloured flames". English. *Edinb. J. Sci.* (1826). Includes bibliographical references, pp. 77–81.

[6] Kirchhoff and Bunsen. "IX. Chemical analysis by spectrum-observations". *Lond. Edinb. Dubl. Phil. Mag.* 20.131 (1860), pp. 88–109.

[7] J. J. Thomson. "XL. Cathode Rays". *Lond.Edinb.Dubl.Phil.Mag.* 44.269 (1897), pp. 293–316.

[8] E. Rutherford. "LXXIX. The scattering of α and β particles by matter and the structure of the atom". *Lond. Edinb. Dubl. Phil. Mag.* 21.125 (1911), pp. 669–688.

[9] N. Bohr. "I. On the constitution of atoms and molecules". *Lond. Edinb. Dubl. Phil. Mag.* 26.151 (1913), pp. 1–25.

[10] N. C. Thomas. "The early history of spectroscopy". *J. Chem. Educ.* 68.8 (1991), p. 631.

[11] J. Keeler. *Understanding NMR Spectroscopy*. John Wiley & Sons Inc, 2010. 526 pp.

[12] P. M. Skrabal. *Spectroscopy*. Vdf Hochschulverlag AG, 2012. 352 pp.

[13] P. Vandenabeele. *Practical Raman Spectroscopy: An Introduction*. Wiley, 2013.

[14] J. B. Hearnshaw. *The Analysis of Starlight*. Cambridge University Press, 2014. 382 pp.

[15] M. Orrit, J. Bernard, and R. I. Personov. "High-resolution spectroscopy of organic molecules in solids: from fluorescence line narrowing and hole burning to single molecule spectroscopy". *J. Phys. Chem.* 97.40 (1993), pp. 10256–10268.

[16] W. E. Moerner, Y. Shechtman, and Q. Wang. "Single-molecule spectroscopy and imaging over the decades". *Faraday Discuss.* 184 (2015), pp. 9–36.

[17] R. Personov, E. Al'Shits, and L. Bykovskaya. "The effect of fine structure appearance in laser-excited fluorescence spectra of organic compounds in solid solutions". *Opt. Commun.* 6.2 (1972), pp. 169–173.

[18] A. A. Gorokhovskiĭ, R. K. Kaarli, and L. A. Rebane. "Hole burning in the contour of a pure electronic line in a Shpol'skiĭ system". *Sov. Phys. JETP Lett.* 20 (1974), p. 216.

[19] B. Kharlamov, R. I. Personov, and L. A. Bykovskaya. "Stable 'Gap' in Absorption Spectra of Solid Solutions of Organic Molecules by Laser Irradiation". *Opt. Commun.* 12 (1974), pp. 191–193.

[20] W. E. Moerner and L. Kador. "Optical detection and spectroscopy of single molecules in a solid". *Phys. Rev. Lett.* 62.21 (1989), pp. 2535–2538.

[21] M. Orrit and J. Bernard. "Single pentacene molecules detected by fluorescence excitation in a p-terphenyl crystal". *Phys. Rev. Lett.* 65.21 (1990), pp. 2716–2719.

[22] P. Tamarat et al. "Ten Years of Single-Molecule Spectroscopy". *J. Phys. Chem. A* 104.1 (2000), pp. 1–16.

[23] W. E. Moerner. "A Dozen Years of Single-Molecule Spectroscopy in Physics, Chemistry, and Biophysics". *J. Phys. Chem. B* 106.5 (2002), pp. 910–927.

[24] E. Betzig and R. J. Chichester. "Single molecules observed by near-field scanning optical microscopy". *Science* 262 (1993), pp. 1422–1425.

[25] S. Nie, D. T. Chiu, and R. N. Zare. "Probing individual molecules with confocal fluorescence microscopy". *Science* 266 (1994), pp. 1018–1021.

[26] P. Tchenio, A. B. Myers, and W. E. Moerner. "Dispersed fluorescence spectra of single molecules of pentacene in p-terphenyl". *J. Phys. Chem.* 97 (1993), pp. 2491–2493.

[27] J. K. Trautman et al. "Near-field spectroscopy of single molecules at room temperature". *Nature* 369.6475 (1994), pp. 40–42.

[28] J. J. Macklin et al. "Imaging and Time-Resolved Spectroscopy of Single Molecules at an Interface". *Science* 272.5259 (1996), pp. 255–258.

[29] W. E. Moerner. "Examining Nanoenvironments in Solids on the Scale of a Single, Isolated Impurity Molecule". *Science* 265.5168 (1994), pp. 46–53.

[30] F. Stracke et al. "Intrinsic conformer jumps observed by single molecule spectroscopy in real time". *Chem. Phys. Lett.* 325 (2000), pp. 196–202.

[31] J. Hofkens et al. "Conformational rearrangements in and twisting of a single molecule". *Chem. Phys. Lett.* 333.3-4 (2001), pp. 255–263.

[32] M. Streiter et al. "Dynamics of Single-Molecule Stokes Shifts: Influence of Conformation and Environment". *J. Phys. Chem. Lett.* (2016), pp. 4281–4284.

[33] R. M. Dickson et al. "On/off blinking and switching behaviour of single molecules of green fluorescent protein". *Nature* 388.6640 (1997), pp. 355–358.

[34] D. A. V. Bout et al. "Discrete Intensity Jumps and Intramolecular Electronic Energy Transfer in the Spectroscopy of Single Conjugated Polymer Molecules". *Science* 277.5329 (1997), p. 1074.

[35] M. A. Kol'chenko. "Intersystem Crossing Mechanisms and Single Molecule Fluorescence: Terrylene in Anthracene Crystals". *Opt. Spectrosc.* 98.5 (2005), p. 681.

[36] S. W. Hell and J. Wichmann. "Breaking the diffraction resolution limit by stimulated emission: stimulated-emission-depletion fluorescence microscopy". *Opt. Lett.* 19.11 (1994), p. 780.

[37] B. Huang, M. Bates, and X. Zhuang. "Super-Resolution Fluorescence Microscopy". *Annu. Rev. Biochem.* 78.1 (2009), pp. 993–1016.

[38] L. Schermelleh, R. Heintzmann, and H. Leonhardt. "A guide to super-resolution fluorescence microscopy". *J. Cell Biol.* 190.2 (2010), pp. 165–175.

[39] A. Kusumi et al. "Tracking single molecules at work in living cells". *Nat. Chem. Biol.* 10.7 (2014), pp. 524–532.

[40] Z. Liu, L. Lavis, and E. Betzig. "Imaging Live-Cell Dynamics and Structure at the Single-Molecule Level". *Mol. Cell* 58.4 (2015), pp. 644–659.

[41] C. Tietz et al. "Spectroscopy on Single Light-Harvesting Complexes at Low Temperature". *J. Phys. Chem. B* 103.30 (1999), pp. 6328–6333.

[42] M. H. Stopel, C. Blum, and V. Subramaniam. "Excitation Spectra and Stokes Shift Measurements of Single Organic Dyes at Room Temperature". *J. Phys. Chem. Lett.* 5.18 (2014), pp. 3259–3264.

[43] E. Thyrhaug et al. "Single-molecule excitation-emission spectroscopy". *Proc. Natl. Acad. Sci. U.S.A.* 116.10 (2019), p. 4064.

[44] S. Chong, W. Min, and X. S. Xie. "Ground-state depletion microscopy: detection sensitivity of single-molecule optical absorption at room temperature". *J. Phys. Chem. Lett.* 1.23 (2010), pp. 3316–3322.

[45] E. M. H. P. van Dijk et al. "Single-Molecule Pump-Probe Detection Resolves Ultrafast Pathways in Individual and Coupled Quantum Systems". *Phys. Rev. Lett.* 94.7 (2005).

[46] R. Hildner, D. Brinks, and N. F. van Hulst. "Femtosecond coherence and quantum control of single molecules at room temperature". *Nat. Phys.* 7.2 (2010), pp. 172–177.

[47] D. Brinks et al. "Ultrafast dynamics of single molecules". *Chem. Soc. Rev.* 43.8 (2014), pp. 2476–2491.

[48] P. Kukura et al. "Single-Molecule Sensitivity in Optical Absorption at Room Temperature". *J. Phys. Chem. Lett* 1.23 (2010), pp. 3323–3327.

[49] A. Gaiduk et al. "Room-Temperature Detection of a Single Molecule's Absorption by Photothermal Contrast". *Science* 330.6002 (2010), pp. 353–356.

[50] K. Brunner et al. "Photoluminescence from a single GaAs/AlGaAs quantum dot". *Phys. Rev. Lett.* 69.22 (1992), pp. 3216–3219.

[51] K. A. Lidke et al. "Superresolution by localization of quantum dots using blinking statistics". *Opt. Express* 13.18 (2005), p. 7052.

[52] A. Gruber. "Scanning Confocal Optical Microscopy and Magnetic Resonance on Single Defect Centers". *Science* 276.5321 (1997), pp. 2012–2014.

[53] E. Ringe et al. "Single nanoparticle plasmonics". *Phys. Chem. Chem. Phys.* 15.12 (2013), p. 4110.

[54] S. Schultz et al. "Single-target molecule detection with nonbleaching multicolor optical immunolabels". *Proc. Natl. Acad. Sci. U.S.A.* 97.3 (2000), pp. 996–1001.

[55] K. Lindfors et al. "Detection and Spectroscopy of Gold Nanoparticles Using Supercontinuum White Light Confocal Microscopy". *Phys. Rev. Lett.* 93.3 (2004).

[56] M. Tokeshi et al. "Single- and countable-molecule detection of non-fluorescent molecules in liquid phase". *J. Lumin.* 83-84 (1999), pp. 261–264.

[57] W.-S. Chang et al. "Plasmonic nanorod absorbers as orientation sensors". *Proc. Natl. Acad. Sci. U.S.A.* 107.7 (2010), pp. 2781–2786.

[58]   H. Baida et al. "Ultrafast Nonlinear Optical Response of a Single Gold Nanorod near Its Surface Plasmon Resonance". *Phys. Rev. Lett.* 107.5 (2011).

[59]   M. Yorulmaz et al. "Single-Particle Absorption Spectroscopy by Photothermal Contrast". *Nano Lett.* 15.5 (2015), pp. 3041–3047.

[60]   M. Zavelani-Rossi et al. "Transient Optical Response of a Single Gold Nanoantenna: The Role of Plasmon Detuning". *ACS Photonics* 2.4 (2015), pp. 521–529.

[61]   M. N. B.-S. Bernard Valeur. *Molecular Fluorescence.* Wiley VCH Verlag GmbH, 2012.

[62]   O. Gabriel. *Franck-Condon-Prinzip.* `https://commons.wikimedia.org/wiki/File:Franck-Condon-Prinzip.svg`. Adaptation of version 12 August 2007.

[63]   C. Gell, A. Smith, and D. Brockwell. *Handbook of Single Molecule Fluorescence Spectroscopy.* Oxfod University Press, 2006. 262 pp.

[64]   P. R. Selvin. *Single Molecule Techniques.* Cold Spring Harbor Laboratory Press, 2008.

[65]   D. E. Makarov. *Single Molecule Science.* Taylor & Francis Ltd., 2015. 214 pp.

[66]   H. Wang et al. "Microheterogeneity in Dye-Doped Silicate and Polymer Films". *J. Phys. Chem. B* 102.37 (1998), pp. 7231–7237.

[67]   O. Mirzov and I. G. Scheblykin. "Photoluminescence spectra of a conjugated polymer: from films and solutions to single molecules". *Phys. Chem. Chem. Phys.* 8 (47 2006), pp. 5569–5576.

[68]   M. Haase et al. "Photoblinking and photobleaching of rylene diimide dyes". *Phys. Chem. Chem. Phys.* 13 (5 2011), pp. 1776–1785.

[69]   C. Blum, A. J. Meixner, and V. Subramaniam. "Room temperature spectrally resolved single-molecule spectroscopy reveals new spectral forms and photophysical versatility of Aequorea green fluorescent protein variants". *Biophysical J.* 87 (2004), pp. 4172–4179.

[70]   F. Stracke et al. "Two and multilevel spectral switching of single molecules in polystyrene at room temperature". *Chem. Phys.* 300.1-3 (2004), pp. 153–164.

[71]   T. Basche and W. E. Moerner. "Optical modification of a single impurity molecule in a solid". *Nature* 355.6358 (1992), pp. 335–337.

[72]   C. Blum et al. "Discrimination and interpretation of spectral phenomen by room-temperature single-molecule spectroscopy". *J. Phys. Chem. A* 105 (2001), pp. 6983–6990.

[73]   W. E. Moerner. "Those Blinking Single Molecules". *Science* 277.5329 (1997), pp. 1059–1060.

[74]   T. Ha et al. "Quantum jumps of single molecules at room temperature". *Chem. Phys. Lett.* 271.1-3 (1997), pp. 1–5.

[75]   W.-T. Yip et al. "Classifying the Photophysical Dynamics of Single- and Multiple-Chromophoric Molecules by Single Molecule Spectroscopy". *J. Phys. Chem. A* 102.39 (1998), pp. 7564–7575.

[76]   M. F. García-Parajó et al. "Optical Probing of Single Fluorescent Molecules and Proteins". *ChemPhysChem* 2.6 (2001), pp. 347–360.

[77]   G. C. Hegerfeldt and D. Seidel. "Blinking molecules: Determination of photophysical parameters from the intensity correlation function". *J. Chem. Phys.* 118.17 (2003), pp. 7741–7746.

[78] Z. Wang and L. J. Rothberg. "Origins of Blinking in Single-Molecule Raman Spectroscopy". *J. Phys. Chem. B* 109.8 (2005), pp. 3387–3391.

[79] S. R. Emory et al. "Re-examining the origins of spectral blinking in single-molecule and single-nanoparticle SERS". *Faraday Discuss.* 132 (2006), pp. 249–259.

[80] E. K. L. Yeow et al. "Characterizing the Fluorescence Intermittency and Photobleaching Kinetics of Dye Molecules Immobilized on a Glass Surface". *J. Phys. Chem. A* 110.5 (2006), pp. 1726–1734.

[81] H. J. Kimble, M. Dagenais, and L. Mandel. "Photon Antibunching in Resonance Fluorescence". *Phys. Rev. Lett.* 39.11 (1977), pp. 691–695.

[82] T. Basché et al. "Photon antibunching in the fluorescence of a single dye molecule trapped in a solid". *Phys. Rev. Lett.* 69.10 (1992), pp. 1516–1519.

[83] W. P. Ambrose et al. "Fluorescence photon antibunching from single molecules on a surface". *Chem. Phys. Lett.* 269.3-4 (1997), pp. 365–370.

[84] W. P. Ambrose and W. E. Moerner. "Fluorescence spectroscopy and spectral diffusion of single impurity molecules in a crystal". *Nature* 349.6306 (1991), pp. 225–227.

[85] A. Zumbusch et al. "Probing individual two-level systems in a polymer by correlation of single molecule fluorescence". *Phys. Rev. Lett.* 70.23 (1993), pp. 3584–3587.

[86] T. Irngartinger, A. Renn, and U. P. Wild. "Fluorescence microscopy: Spectral jumps of single molecules". *J. Lumin.* 66-67 (1995), pp. 232–235.

[87] B. Kozankiewicz and M. Orrit. "Single-molecule photophysics, from cryogenic to ambient conditions". *Chem. Soc. Rev.* 43.4 (2014), pp. 1029–1043.

[88] P. Malý et al. "Ultrafast energy relaxation in single light-harvesting complexes". *Proc. Natl. Acad. Sci. U.S.A.* 113.11 (2016), pp. 2934–2939.

[89] D. Brinks et al. "Visualizing and controlling vibrational wave packets of single molecules". *Nature* 465.7300 (2010), pp. 905–908.

[90] R. Hildner et al. "Quantum Coherent Energy Transfer over Varying Pathways in Single Light-Harvesting Complexes". *Science* 340.6139 (2013), pp. 1448–1451.

[91] W. Min et al. "Imaging chromophores with undetectable fluorescence by stimulated emission microscopy". *Nature* 461 (2009), pp. 1105–1109.

[92] F. Lord Rayleigh. "XXXI. Investigations in optics, with special reference to the spectroscope". *Lond. Edinb. Dubl. Phil. Mag.* 8.49 (1879), pp. 261–274.

[93] S. Shashkova and M. Leake. "Single-molecule fluorescence microscopy review: shedding new light on old problems". *Biosci. Rep.* 37.4 (2017), BSR20170031.

[94] H. Quante and K. Müllen. "Quaterrylenebis(dicarboximides)". *Angew. Chem. Int. Ed. Engl.* 34.12 (1995), pp. 1323–1325.

[95] C. Eggeling et al. "Photobleaching of Fluorescent Dyes under Conditions Used for Single-Molecule Detection: Evidence of Two-Step Photolysis". *Anal. Chem.* 70.13 (1998), pp. 2651–2659.

[96] A. Diaspro et al. "Enhanced Green Fluorescent Protein (GFP) fluorescence after polyelectrolyte caging". *Opt. Express* 14.21 (2006), p. 9815.

[97]   E. Wientjes et al. "Pushing the Photon Limit: Nanoantennas Increase Maximal Photon Stream and Total Photon Number". *J. Phys. Chem. Lett.* 7.9 (2016), pp. 1604–1609.

[98]   J. Kauppinen and J. Partanen. *Fourier Transforms in Spectroscopy*. Wiley-VCH Verlag GmbH, 2002.

[99]   B. Hlivko, H. Hong, and R. R. Williams. "Fourier Transform Fluorescence Spectrometry". *Appl. Spectrosc.* 42.8 (1988), pp. 1563–1566.

[100]   G. V. Hartland et al. "Time-resolved Fourier transform spectroscopy with 0.25 cm-1 spectral and 10-7 s time resolution in the visible region". *Rev. Sci. Instrum.* 63.6 (1992), pp. 3261–3267.

[101]   P. Griffiths and J. De Haseth. *Fourier Transform Infrared Spectrometry*. Chemical Analysis: A Series of Monographs on Analytical Chemistry and Its Applications. Wiley, 2007.

[102]   J. G. Hirschberg et al. "Interferometric measurement of fluorescence excitation spectra". *Appl. Opt.* 37.10 (1998), pp. 1953–1957.

[103]   A. Perri et al. "Excitation-emission Fourier-transform spectroscopy based on a birefringent interferometer". *Opt. Express* 25.12 (2017), A483–A490.

[104]   P. B. Fellgett. "On the Ultimate Sensitivity and Practical Performance of Radiation Detectors". *J. Opt. Soc. Am.* 39.11 (1949), p. 970.

[105]   J. Connes and P. Connes. "Near-Infrared Planetary Spectra by Fourier Spectroscopy I Instruments and Results". *J. Opt. Soc. Am.* 56.7 (1966), p. 896.

[106]   C. E. Shannon. "Communication in the presence of noise". *Proc. IRE* 37.1 (1949), pp. 10–21.

[107]   F. Harris. "On the use of windows for harmonic analysis with the discrete Fourier transform". *Proc. IEEE* 66.1 (1978), pp. 51–83.

[108]   T. Weil et al. "The Rylene Colorant Family-Tailored Nanoemitters for Photonics Research and Applications". *Angew. Chem. Int. Ed.* 49.48 (2010), pp. 9068–9093.

[109]   Y. Avlasevich, C. Li, and K. Müllen. "Synthesis and applications of core-enlarged perylene dyes". *J. Mater. Chem.* 20 (19 2010), pp. 3814–3826.

[110]   R. Korlacki et al. "Optical Fourier Transform Spectroscopy of Single-Walled Carbon Nanotubes and Single Molecules". *ChemPhysChem* 8.7 (2007), pp. 1049–1055.

[111]   D. Brinks et al. "Beating spatio-temporal coupling: implications for pulse shaping and coherent control experiments". *Opt. Express* 19.27 (2011), p. 26486.

[112]   L. Zehnder. "Ein neuer Interferenzrefraktor". *Z. Instrumentenkd.* 11.275 (1891), pp. 275–285.

[113]   L. Mach. "Über einen Interferenzrefraktor". *Z. Instrumentenkd.* 12 (1892).

[114]   R. Croce and H. van Amerongen. "Natural strategies for photosynthetic light harvesting". *Nat. Chem. Biol.* 10.7 (2014), pp. 492–501.

[115]   D. Rutkauskas et al. "Fluorescence Spectral Fluctuations of Single LH2 Complexes from Rhodopseudomonas acidophila Strain 10050". *Biochemistry (Mosc.)* 43.15 (2004), pp. 4431–4438.

[116]   R. E. Blankenship. *Molecular Mechanisms of Photosynthesis*. Wiley-Blackwell, 2014.

[117]   H. Sumi. "Bacterial photosynthesis begins with quantum-mechanical coherence". *Chem. Rec.* 1.6 (2001), pp. 480–493.

[118]   Y. C. Cheng and R. J. Silbey. "Coherence in the B800 Ring of Purple Bacteria LH2". *Phys. Rev. Lett.* 96.2 (2006), p. 028103.

[119]   E. Harel and G. S. Engel. "Quantum coherence spectroscopy reveals complex dynamics in bacterial light-harvesting complex 2 (LH2)". *Proc. Natl. Acad. Sci. U.S.A.* 109.3 (2012), pp. 706–711.

[120]   R. E. Blankenship et al. "Comparing Photosynthetic and Photovoltaic Efficiencies and Recognizing the Potential for Improvement". *Science* 332.6031 (2011), pp. 805–809.

[121]   F. Odobel, Y. Pellegrin, and J. Warnan. "Bio-inspired artificial light-harvesting antennas for enhancement of solar energy capture in dye-sensitized solar cells". *Energy Environ. Sci.* 6.7 (2013), p. 2041.

[122]   G. S. Engel et al. "Evidence for wavelike energy transfer through quantum coherence in photosynthetic systems". *Nature* 446 (2007), p. 782.

[123]   E. Thyrhaug et al. "Identification and characterization of diverse coherences in the Fenna-Matthews-Olson complex". *Nat. Chem.* 10.7 (2018), pp. 780–786.

[124]   G. McDermott et al. "Crystal structure of an integral membrane light-harvesting complex from". *Nature* 374.6522 (1995), pp. 517–521.

[125]   M. Z. Papiz et al. "The Structure and Thermal Motion of the B800-850 LH2 Complex from Rps. acidophila at 2.0 Å Resolution and 100 K: New Structural Features and Functionally Relevant Motions". *J. Mol. Biol.* 326.5 (2003), pp. 1523–1538.

[126]   A. M. van Oijen et al. "Spectroscopy of Single Light-Harvesting Complexes from Purple Photosynthetic Bacteria at 1.2 K". *J. Phys. Chem. B* 102.47 (1998), pp. 9363–9366.

[127]   M. A. Bopp et al. "The dynamics of structural deformations of immobilized single light-harvesting complexes". *Proc. Natl. Acad. Sci. U.S.A.* 96.20 (1999), pp. 11271–11276.

[128]   M. Matsushita et al. "Spectroscopy on the B850 Band of Individual Light-Harvesting 2 Complexes of Rhodopseudomonas acidophila II. Exciton States of an Elliptically Deformed Ring Aggregate". *Biophys. J.* 80.3 (2001), pp. 1604–1614.

[129]   C. Hofmann et al. "Direct observation of tiers in the energy landscape of a chromoprotein: A single-molecule study". *Proc. Natl. Acad. Sci. U.S.A.* 100.26 (2003), pp. 15534–15538.

[130]   O. Zerlauskiene et al. "Static and Dynamic Protein Impact on Electronic Properties of Light-Harvesting Complex LH2". *J. Phys. Chem. B* 112.49 (2008), pp. 15883–15892.

[131]   R. Kunz et al. "Single-Molecule Spectroscopy Unmasks the Lowest Exciton State of the B850 Assembly in LH2 from Rps. acidophila". *Biophys. J.* 106.9 (2014), pp. 2008–2016.

[132]   D. Rutkauskas et al. "RETRACTED: Fluorescence Spectroscopy of Conformational Changes of Single LH2 Complexes". *Biophys. J.* 88.1 (2005), pp. 422–435.

[133]   G. S. Schlau-Cohen et al. "Single-molecule spectroscopy reveals photosynthetic LH2 complexes switch between emissive states". *Proc. Natl. Acad. Sci. U.S.A.* 110.27 (2013), pp. 10899–10903.

[134]   E. Wientjes et al. "Strong antenna-enhanced fluorescence of a single light-harvesting complex shows photon antibunching". *Nat. Commun.* 5.1 (2014).

[135]   F. Caycedo-Soler et al. "Theory of Excitonic Delocalization for Robust Vibronic Dynamics in LH2". *J. Phys. Chem. Lett.* 9.12 (2018), pp. 3446–3453.

[136]   V. I. Novoderezhkin, D. Rutkauskas, and R. van Grondelle. "Dynamics of the Emission Spectrum of a Single LH2 Complex: Interplay of Slow and Fast Nuclear Motions". *Biophys. J.* 90.8 (2006), pp. 2890–2902.

[137]   S. Tubasum et al. "Evidence of excited state localization and static disorder in LH2 investigated by 2D-polarization single-molecule imaging at room temperature". *Phys. Chem. Chem. Phys.* 15.45 (2013), pp. 19862–19869.

[138]   L. Piatkowski, E. Gellings, and N. F. van Hulst. "Broadband single-molecule excitation spectroscopy". *Nat. Commun.* 7 (2016), p. 10411.

[139]   R. J. Cogdell, A. Gall, and J. Köhler. "The architecture and function of the light-harvesting apparatus of purple bacteria: from single molecules to in vivo membranes". *Q. Rev. Biophys.* 39.03 (2006), pp. 227–324.

[140]   R. Monshouwer et al. "Superradiance and Exciton Delocalization in Bacterial Photosynthetic Light-Harvesting Systems". *J. Phys. Chem. B* 101.37 (1997), pp. 7241–7248.

[141]   J. L. Herek et al. "Quantum control of energy flow in light harvesting". *Nature* 417.6888 (2002), pp. 533–535.

[142]   S. Prince et al. "Apoprotein structure in the LH2 complex from Rhodpseudomonas acidophila strain 10050: modular assembly and protein pigment interactions 1 1Edited by R. Huber". *J. Mol. Biol.* 268.2 (1997), pp. 412–423.

[143]   M. F. Richter et al. "Single-Molecule Spectroscopic Characterization of Light-Harvesting 2 Complexes Reconstituted into Model Membranes". *Biophys. J.* 93.1 (2007), pp. 183–191.

[144]   R. Kunz et al. "Fluorescence-Excitation and Emission Spectra from LH2 Antenna Complexes of Rhodopseudomonas acidophila as a Function of the Sample Preparation Conditions". *J. Phys. Chem. B* 117.40 (2013), pp. 12020–12029.

[145]   F. Schleifenbaum et al. "Single-molecule spectral dynamics at room temperature". *Mol. Phys.* 107.18 (2009), pp. 1923–1942.

[146]   L. Piatkowski, E. Gellings, and N. F. van Hulst. "Multicolour single molecule emission and excitation spectroscopy reveals extensive spectral shifts". *Faraday Discuss.* 184 (2015), pp. 207–220.

[147]   A. T. Gardiner, S. Takaichi, and R. J. Cogdell. "The effect of changes in light intensity and temperature on the peripheral antenna of Rhodopseudomonas acidophila". *Biochem. Soc. Trans.* 21.1 (1993), 6S–6S.

[148]   R. E. Hirsch. "Heme-Protein Fluorescence". *Topics in Fluorescence Spectroscopy.* Kluwer Academic Publishers, 2006, pp. 221–255.

[149]   M. Twardowska et al. "Fluorescence enhancement of photosynthetic complexes separated from nanoparticles by a reduced graphene oxide layer". *Appl. Phys. Lett.* 104.9 (2014), p. 093103.

[150] I. Kaminska et al. "Strong Plasmonic Enhancement of a Single Peridinin–Chlorophyll a–Protein Complex on DNA Origami-Based Optical Antennas". *ACS Nano* 12.2 (2018), pp. 1650–1655.

[151] C. Chen et al. "Viewing the Interior of a Single Molecule: Vibronically Resolved Photon Imaging at Submolecular Resolution". *Phys. Rev. Lett.* 105.21 (2010).

[152] I. Rajapaksa and H. K. Wickramasinghe. "Raman spectroscopy and microscopy based on mechanical force detection". *Appl. Phys. Lett.* 99.16 (2011), p. 161103.

[153] A. Einstein. "Zur Quantentheorie der Strahlung". *Phys. Z.* 18 (1917).

[154] L. Kastrup and S. W. Hell. "Absolute Optical Cross Section of Individual Fluorescent Molecules". *Angew. Chem. Int. Ed.* 43.48 (2004), pp. 6646–6649.

[155] A. Grofcsik and W. J. Jones. "Stimulated emission cross-sections in fluorescent dye solutions: gain spectra and excited-state lifetimes of Nile blue A and oxazine 720". *J. Chem. Soc., Faraday Trans.* 88.8 (1992), p. 1101.

[156] M. Liebel, C. Toninelli, and N. F. van Hulst. "Room-temperature ultrafast nonlinear spectroscopy of a single molecule". *Nat. Photonics* 12.1 (2017), pp. 45–49.

[157] C. Toninelli et al. "Near-infrared single-photons from aligned molecules in ultrathin crystalline films at room temperature". *Opt. Express* 18.7 (2010), p. 6577.

[158] C. Polisseni et al. "Stable, single-photon emitter in a thin organic crystal for application to quantum-photonic devices". *Opt. Express* 24.5 (2016), p. 5615.

[159] A. A. L. Nicolet et al. "Single Dibenzoterrylene Molecules in an Anthracene Crystal: Main Insertion Sites". *ChemPhysChem* 8.13 (2007), pp. 1929–1936.

[160] I. Deperasińska et al. "On the photo-stability of single molecules. Dibenzoterrylene in 2,3-dimethylnaphthalene crystals". *Chem. Phys. Lett.* 492.1-3 (2010), pp. 93–97.

[161] Z. S. Sadeq, R. A. Muniz, and J. E. Sipe. "One- and two-photon absorption spectra of dibenzoterrylene". *Phys. Rev. Mater.* 2.7 (2018).

[162] J. Vangindertael et al. "An introduction to optical super-resolution microscopy for the adventurous biologist". *Method. Appl. Fluoresc.* 6.2 (2018), p. 022003.

[163] E. Wolf. "Electromagnetic diffraction in optical systems - I. An integral representation of the image field". *Proc. R. Soc. London, Ser. A* 253.1274 (1959), pp. 349–357.

[164] B. Richards and E. Wolf. "Electromagnetic diffraction in optical systems, II. Structure of the image field in an aplanatic system". *Proc. R. Soc. London, Ser. A* 253.1274 (1959), pp. 358–379.

[165] Q. Li. "Optimization of point spread function of a high numerical aperture objective lens : application to high resolution optical imaging and fabrication". PhD thesis. École normale supérieure de Cachan - ENS Cachan, 2014.

[166] E. Clar and W. Willicks. "Aromatische Kohlenwasserstoffe, LXIX. Mitteil.: 7.8;16.16-Dibenzterrylen". *Chem. Ber.* 88.8 (1955), pp. 1205–1207.

[167] I. Gregor, D. Patra, and J. Enderlein. "Optical Saturation in Fluorescence Correlation Spectroscopy under Continuous-Wave and Pulsed Excitation". *ChemPhysChem* 6.1 (2005), pp. 164–170.

[168] J. Humpolíčková, A. Benda, and J. Enderlein. "Optical Saturation as a Versatile Tool to Enhance Resolution in Confocal Microscopy". *Biophys. J.* 97.9 (2009), pp. 2623–2629.

[169]   P. Wilson. *The Circuit Designer's Companion.* Elsevier LTD, Oxford, 2017.

[170]   M. Selmke, M. Braun, and F. Cichos. "Photothermal Single-Particle Microscopy: Detection of a Nanolens". *ACS Nano* 6.3 (2012), pp. 2741–2749.

[171]   A. M. Nawar and I. Yahia. "Fabrication and characterization of anthracene thin films for wide-scale organic optoelectronic applications based on linear/nonlinear analyzed optical dispersion parameters". *Opt. Mater.* 70 (2017), pp. 1–10.

[172]   P. Mühlschlegel et al. "Resonant Optical Antennas". *Science* 308.5728 (2005), pp. 1607–1609.

[173]   L. Novotny and N. van Hulst. "Antennas for light". *Nat. Photonics* 5.2 (2011), pp. 83–90.

[174]   S. W. Prescott and P. Mulvaney. "Gold nanorod extinction spectra". *J. Appl. Phys.* 99.12 (2006), p. 123504.

[175]   K. Saha et al. "Gold Nanoparticles in Chemical and Biological Sensing". *Chem. Rev.* 112.5 (2012), pp. 2739–2779.

[176]   P. Tuersun et al. "Refractive index sensitivity analysis of gold nanoparticles". *Optik* 149 (2017), pp. 384–390.

[177]   J. Jiang et al. "Plasmonic nano-arrays for ultrasensitive bio-sensing". *Nanophotonics* 7.9 (2018), pp. 1517–1531.

[178]   E. C. Dreaden et al. "The golden age: gold nanoparticles for biomedicine". *Chem. Soc. Rev.* 41.7 (2012), pp. 2740–2779.

[179]   X. Fan et al. "Sensitive optical biosensors for unlabeled targets: A review". *Anal. Chim. Acta* 620.1-2 (2008), pp. 8–26.

[180]   A. Kinkhabwala et al. "Large single-molecule fluorescence enhancements produced by a bowtie nanoantenna". *Nat. Photonics* 3.11 (2009), pp. 654–657.

[181]   T. H. Taminiau et al. "Optical antennas direct single-molecule emission". *Nat. Photonics* 2.4 (2008), pp. 234–237.

[182]   E. Boulais et al. "Plasmonics for pulsed-laser cell nanosurgery: Fundamentals and applications". *J. Photochem. Photobiol., C* 17 (2013), pp. 26–49.

[183]   J. B. Vines et al. "Gold Nanoparticles for Photothermal Cancer Therapy". *Front. Chem.* 7 (2019).

[184]   S. Berciaud et al. "Photothermal Heterodyne Imaging of Individual Nonfluorescent Nanoclusters and Nanocrystals". *Phys. Rev. Lett.* 93.25 (2004).

[185]   J. Hwang and W. Moerner. "Interferometry of a single nanoparticle using the Gouy phase of a focused laser beam". *Opt. Commun.* 280.2 (2007), pp. 487–491.

[186]   M. Selmke and F. Cichos. "Energy-redistribution signatures in transmission microscopy of Rayleigh and Mie particles". *J. Opt. Soc. Am. A* 31.11 (2014), p. 2370.

[187]   F. Gittes and C. F. Schmidt. "Interference model for back-focal-plane displacement detection in optical tweezers". *Opt. Lett.* 23.1 (1998), p. 7.

[188]   A. Pralle et al. "Three-dimensional high-resolution particle tracking for optical tweezers by forward scattered light". *Microsc. Res. Tech.* 44.5 (1999), pp. 378–386.

[189]   A. Rohrbach and E. H. K. Stelzer. "Three-dimensional position detection of optically trapped dielectric particles". *J. Appl. Phys.* 91.8 (2002), pp. 5474–5488.

[190] D. Boyer et al. "Photothermal Imaging of Nanometer-Sized Metal Particles Among Scatterers". *Science* 297.5584 (2002), pp. 1160–1163.

[191] P. Berto et al. "Time-harmonic optical heating of plasmonic nanoparticles". *Phys. Rev. B* 90.3 (2014).

[192] A. Gaiduk et al. "Detection limits in photothermal microscopy". *Chem. Sci.* 1.3 (2010), p. 343.

[193] V. P, C. L, and L. B. "Photothermal microscopy: optical detection of small absorbers in scattering environments". *J. Microsc.* 254.3 (2014), pp. 115–121.

[194] M. Selmke, M. Braun, and F. Cichos. "Nano-lens diffraction around a single heated nano particle". *Opt. Express* 20.7 (2012), p. 8055.

[195] H. Chen et al. "Shape- and Size-Dependent Refractive Index Sensitivity of Gold Nanoparticles". *Langmuir* 24.10 (2008), pp. 5233–5237.

[196] S. Berciaud et al. "Photothermal heterodyne imaging of individual metallic nano-particles: Theory versus experiment". *Phys. Rev. B* 73.4 (2006).

[197] J. Parsons et al. "A comparison of techniques used to simulate the scattering of electromagnetic radiation by metallic nanostructures". *J. Mod. Opt.* 57.5 (2010), pp. 356–365.

[198] R. Gans. "Über die Form ultramikroskopischer Goldteilchen". *Ann. Phys.* 342.5 (1912), pp. 881–900.

[199] C. F. Bohren and D. R. Huffman. *Absorption and Scattering of Light by Small Particles*. Wiley-VCH, 1998.

[200] G. W. Bryant, F. J. G. de Abajo, and J. Aizpurua. "Mapping the Plasmon Resonances of Metallic Nanoantennas". *Nano Lett.* 8.2 (2008), pp. 631–636.

[201] H. Chen et al. "Gold nanorods and their plasmonic properties". *Chem. Soc. Rev.* 42.7 (2013), pp. 2679–2724.

[202] P. B. Johnson and R. W. Christy. "Optical Constants of the Noble Metals". *Phys. Rev. B* 6.12 (1972), pp. 4370–4379.

[203] C. Fang et al. "Facile Growth of High-Yield Gold Nanobipyramids Induced by Chloroplatinic Acid for High Refractive Index Sensing Properties". *Sci. Rep.* 6.1 (2016).

[204] O. Svelto. *Principles of Lasers*. Springer US, 2010.

[205] Y. Han and Z. Wu. "Scattering of a spheroidal particle illuminated by a Gaussian beam". *Appl. Opt.* 40.15 (2001), p. 2501.

[206] Y. Han, G. Gréhan, and G. Gouesbet. "Generalized Lorenz-Mie Theory for a Spheroidal Particle with Off-Axis Gaussian-Beam Illumination". *Appl. Opt.* 42.33 (2003), p. 6621.

[207] F. Xu et al. "Generalized Lorenz-Mie theory for an arbitrarily oriented, located, and shaped beam scattered by a homogeneous spheroid". *J. Opt. Soc. Am. A* 24.1 (2007), p. 119.

[208] O. Ekici et al. "Thermal analysis of gold nanorods heated with femtosecond laser pulses". *J. Phys. D: Appl. Phys.* 41.18 (2008), p. 185501.

[209] Z. Chen et al. "Imaging Local Heating and Thermal Diffusion of Nanomaterials with Plasmonic Thermal Microscopy". *ACS Nano* 9.12 (2015), pp. 11574–11581.

[210] Schott. *Optical Glass - Data sheet Inquiry Glass*. Version 28/08/2019.

[211] R. J. Moerland and J. P. Hoogenboom. "Subnanometer-accuracy optical distance ruler based on fluorescence quenching by transparent conductors". *Optica* 3.2 (2016), p. 112.

[212] A. B. Socorro et al. "Temperature sensor based on a hybrid ITO-silica resonant cavity". *Opt. Express* 23.3 (2015), p. 1930.

[213] T. Ashida et al. "Thermal transport properties of polycrystalline tin-doped indium oxide films". *J. Appl. Phys.* 105.7 (2009), p. 073709.

[214] S. Bialkowski. *Photothermal Spectroscopy Methods for Chemical Analysis*. Wiley-Interscience, 1995. 620 pp.

[215] SPI Supplies. *Cargille™ Immersion Oils: Type DF, FF, and HF*. https://www.2spi.com/catalog/documents/CargilleImmersion-Fluorescence.pdf. Accessed 15 Aug 2019.

[216] P. M. R. Paulo et al. "Photothermal Correlation Spectroscopy of Gold Nanoparticles in Solution". *J. Phys. Chem. C* 113.27 (2009), pp. 11451–11457.

[217] J. Miyazaki et al. "Optimal detection angle in sub-diffraction resolution photothermal microscopy: application for high sensitivity imaging of biological tissues". *Opt. Express* 22.16 (2014), p. 18833.

[218] M. Selmke, M. Braun, and F. Cichos. "Gaussian beam photothermal single particle microscopy". *J. Opt. Soc. Am. A* 29.10 (2012), p. 2237.

[219] C. Ungureanu et al. "Discrete dipole approximation simulations of gold nanorod optical properties: Choice of input parameters and comparison with experiment". *J. Appl. Phys.* 105.10 (2009), p. 102032.

[220] M. Yorulmaz et al. "Luminescence Quantum Yield of Single Gold Nanorods". *Nano Lett.* 12.8 (2012), pp. 4385–4391.

[221] Y. Fang et al. "Plasmon Emission Quantum Yield of Single Gold Nanorods as a Function of Aspect Ratio". *ACS Nano* 6.8 (2012), pp. 7177–7184.

[222] Y.-Y. Cai et al. "Photoluminescence of Gold Nanorods: Purcell Effect Enhanced Emission from Hot Carriers". *ACS Nano* 12.2 (2018), pp. 976–985.

[223] S. Hell et al. "Aberrations in confocal fluorescence microscopy induced by mismatches in refractive index". *J. Microsc.* 169.3 (1993), pp. 391–405.

[224] M. Selmke. "Photothermal Single Particle Detection in Theory & Experiments". PhD thesis. Universität Leipzig, 2013.

[225] T. Read, R. V. Olkhov, and A. M. Shaw. "Measurement of the localised plasmon penetration depth for gold nanoparticles using a non-invasive bio-stacking method". *Phys. Chem. Chem. Phys.* 15.16 (2013), p. 6122.

[226] W. Lukosz. "Light emission by magnetic and electric dipoles close to a plane dielectric interface III Radiation patterns of dipoles with arbitrary orientation". *J. Opt. Soc. Am.* 69.11 (1979), p. 1495.

[227] M. Selmke et al. "Photothermal single particle microscopy using a single laser beam". *Appl. Phys. Lett.* 105.1 (2014), p. 013511.

[228] P. Zijlstra, J. W. M. Chon, and M. Gu. "Effect of heat accumulation on the dynamic range of a gold nanorod doped polymer nanocomposite for optical laser writing and patterning". *Opt. Express* 15.19 (2007), p. 12151.